Novel Carbon (C)-Boron (B)-Nitrogen (N)-Containing H_2 Storage Materials

DOE Award No. DE-EE0005658

Final Report
August 2016

Project Period: 5 March 2012 – 14 August 2016

Recipient: University of Oregon (5 March 2012 – June 30 2013)
Boston College (September 1 2013 – August 14 2016)

University of Oregon:
Department of Chemistry
1253 University of Oregon
Eugene, OR 97403-1253

Boston College
Merkert Chemistry Center
2609 Beacon Street
Chestnut Hill, MA 02467

Sub-recipients: Pacific Northwest National Laboratory (PNNL)
The University of Alabama
Protonex Technology Corporation (since October 1, 2015 a subsidiary of Ballard Power Systems)

Contacts: Prof. Shih-Yuan Liu, Boston College
(617) 552-8543; shihyuan.liu@bc.edu

Dr. Tom Autrey, PNNL
(509) 375-3792; tom.autrey@pnnl.gov

Prof. David A. Dixon, The University of Alabama
(205) 348-8441; dadixon@bama.ua.edu

Dr. Paul Osenar, Protonex Technology Corporation
(508) 490-9960; paul.osenar@protonex.com

Executive Summary

The following summarizes the research conducted for DOE project DE-EE0005658 "Novel Carbon(C)-Boron(B)-Nitrogen(N)-Containing H_2 Storage Materials". This work focused in part on the continued study of two materials identified from the preceding project DE-FG360GO18143 ("Hydrogen Storage by Novel CBN Heterocycle Materials") as lead candidates to meet the DOE technical targets for either vehicular or non-automotive hydrogen storage applications. Specifically, a room-temperature liquid, 3-methyl-1,2-cyclopentane (**B**), and a high H_2 capacity solid, 1,2-BN-cyclohexane (**J**), were selected for further characterization and performance optimization. In addition to these compounds, the current project also aimed to prepare several new materials predicted to be disposed towards direct reversibility of H_2 release and uptake, a feature deemed critical to achieving efficient recycling of spent fuel end products. To assist in the rational design of these and other next-generation materials, this project undertook to investigate the mechanism of hydrogen release from established compounds (mainly **B** and **J**) using a combined experimental/computational approach.

Among this project's signature accomplishments, the preliminary synthetic route to **B** was optimized for production on decagram scale. With such quantities of material available, its performance in powering an actual 30 W proton exchange membrane (PEM) fuel cell stack was tested and found to be identical to that of facility H_2. Despite this positive proof-of-concept achievement, however, further consideration of neat **B** as a potential hydrogen storage material was abandoned due to evidence of thermal instability. Specifically, mass spectrometry-coupled thermogravimetric analysis (TGA-MS) revealed significant H_2 release from **B** to initiate at 50 °C, well below the 60 °C minimum threshold set by the DOE.

This result prompted a more extensive investigation in the decomposition mechanism of **B** *vis-à-vis* that of **J**, which exhibited in neat form a substantially higher onset temperature for spontaneous H_2 release (70 °C). Solution-phase kinetic experiments using ReactIR established a second-order dependence for the initial loss of H_2 from both **B** and **J**; Arrhenius analysis, however, revealed the activation barrier for this reaction was lower for **B** than for **J**, which presumably contributes to the diminished thermal stability of the former. On the basis of these and other experimental results, extensive computational efforts yielded a reasonable mechanistic model for the dehydrogenation of 1,2-BN-cycloalkane materials.

While the prospect of *neat* **B** as a suitable hydrogen storage material was discarded, it was proposed that the *combination* of **B** with more thermally stable amine-borane-based materials might afford mixtures with improved properties. Indeed, when **B** was combined with ammonia borane (AB) in a 2:1 molar ratio, the two materials formed a liquid. More significantly, this mixture remained liquid even after complete dehydrogenation, thus establishing the potential for a single-phase fuel cycle. (In contrast, the dehydrogenation product of neat **B** is a low melting solid (mp = 28−30 °C).) Another advantage conferred by the blend formulation was a dramatic reduction in the amount of borazine produced by AB. Borazine is a well-known contaminant of H_2 produced by the thermal decomposition of neat AB, and exerts deleterious effects on fuel cell performance. Residual gas analysis (RGA) of the gas stream generated from the **B**-AB blend, however, detected just 0.01% borazine content when a Pt-Ni nanoparticle dehydrogenation catalyst was used. In all

then, the 2:1 **B-**AB blend marks a major achievement in the effort to develop a suitable liquid amine-borane hydrogen storage material, and merits further investigation into the optimization for practical adoption.

Similar realization of the potential of **J** as a high % wt. H_2 material required a method to dehydrogenate the carbonaceous components of the molecule *without* the use of a sacrificial hydrogen acceptor, as had been reported in the previous project. Ultimately, this reaction was achieved for a *B,N*-disubstituted BN-cyclohexene model substrate using a gas flow system with a fixed Pd/C catalyst bed. Considerable work remains, however, to translate these initial results into a general protocol for complete dehydrogenation of fully saturated BN-cycloalkane materials such as **J**.

With concrete confirmation of the possibility to perform both BN and CC dehydrogenation on a single theoretical substrate, COMSOL modeling was used to evaluate the effects of thermodynamically coupling the two reactions. It was hypothesized that the heat generated from exothermic BN dehydrogenation would partially drive the endothermic CC dehydrogenation reaction; this additional heat consumption was expected to in turn confer the benefit of lowering the maximum reactor temperature. A two-dimensional model of an axisymmetric reactor including experimental kinetic and calculated thermodynamic parameters for both reactions did indeed predict these outcomes. The extent to which the effects of thermodynamic coupling actually manifested, however, were also revealed to depend strongly on the relative rates of the two reactions, as well as the magnitude of the equilibrium constant governing the progress of the endothermic process.

Given the evident complexity of attaining high effective % wt. H_2 capacity with **J**, alternative systems were investigated for greater facility of extensive H_2 release. Among those studied, 1,2,4,5-bis-BN-cyclohexane (**H**) demonstrated the most favorable properties, particularly with respect to thermal stability: rather than decompose, a neat sample instead sublimed when heated above 150 °C. Nevertheless, two commercially available catalytic systems were identified to effect release of two H_2 equivalents from **H**. Release of further equivalents were apparently impeded by the formation of either polymeric material or one of two dimeric cage compounds depending on the catalyst used. Notably, a method to regenerate **H** from these product mixtures remains to be developed. Thus, while **H** may prove useful for certain long-term energy storage needs, it is currently less suited applications involving frequent fuel consumption.

Similar difficulties were also encountered in attempts to realize the complete fuel cycle of 1,3-BN-cyclohexane (**E**) and *B,N*-substituted derivatives thereof. It had been initially proposed that **E** would provide for readily reversible BN dehydrogenation through a measure of frustrated Lewis pair-type character. Indeed, computations predicted this reaction would be essentially thermoneutral in solution. In the course of attempts to fully hydrogenate the spent fuel, however, dimeric species formed and proved resistant to further BN reduction. While a number of monomeric cyclic compounds were also successfully synthesized as formal boron-nitrogen frustrated Lewis pairs, none demonstrated any capacity to split H_2 across the BN unit. The challenge of developing a practical amine-borane-based material for readily reversible hydrogen storage thus remains unresolved at this time. As such, it deserves consideration as a major objective of any future work.

Publications that acknowledge DOE-EERE support:

1) Matus, M.; Liu, S.-Y.; Dixon, D. A. "Dehydrogenation Reactions of Cyclic $C_2B_2N_2H_{12}$ and C_4BNH_{12} Isomers" *J. Phys. Chem. A* **2010**, *114*, 2644-2654. [10.1021/jp9102838]

2) Campbell, P. G.; Zakharov, L. N.; Grant, D.; Dixon, D. A.; Liu, S.-Y. "Hydrogen Storage by Boron-Nitrogen Heterocycles: A Simple Route for Spent Fuel Regeneration" *J. Am. Chem. Soc.* **2010**, *132*, 3289-3291. [10.1021/ja9106622]

3) Daly, A. M.; Tanjaroon, C.; Marwitz, A. J. V.; Liu, S.-Y.; Kukolich S. G. "Microwave Spectrum, Structural Parameters, and Quadrupole Coupling for 1,2-Dihydro-1,2-azaborine" *J. Am. Chem. Soc.* **2010**, *132*, 5501-5506. [10.1021/ja1005338]

4) Campbell, P. G.; Abbey, E. R.; Neiner, D.; Grant, D. J.; Dixon, D. A.; Liu, S.-Y. "Resonance Stabilization Energy of 1,2-Azaborines: A Quantitative Experimental Study by Reaction Calorimetry" *J. Am. Chem. Soc.* **2010**, *132*, 18048-18050. [10.1021/ja109596m]

5) Luo, W.; Zakharov, L. N.; Liu, S.-Y. "1,2-BN Cyclohexane: Synthesis, Structure, Dynamics, and Reactivity" *J. Am. Chem. Soc.* **2011**, *133*, 13006-13009. [10.1021/ja206497x]

6) Marwitz, A. J. V.; Lamm, A. N.; Zakharov, L. N.; Vasiliu, M.; Dixon, D. A.; Liu, S.-Y. "BN-substituted diphenylacetylene: a basic model for conjugated pi-systems containing the BN bond pair" *Chem. Sci.* **2012**, *3*, 825-829. [10.1039/C1SC00500F]

7) Luo, W.; Campbell, P. G.; Zakharov, L. N.; Liu, S.-Y. "A Single-Component Liquid-Phase Hydrogen Storage Material" *J. Am. Chem. Soc.* **2011**, *133*, 19326-19329. [10.1021/ja208834v].

* Highlighted in:
Chemical & Engineering News (C&EN) (2011, November 28, page 35)
Nature Chemistry **2012**, *4*, 5 -
Nature Climate Change **2012**, *2*, 23

8) Campbell, P. G.; Marwitz, A. J. V.; Liu, S.-Y. "Recent Advances in Azaborine Chemistry" *Angew. Chem. Int. Ed.* **2012**, *51*, 6074-6092. [10.1002/anie.201200063]

9) Luo, W.; Neiner, D.; Karkamkar, A.; Parab, K.; Garner, E. B.; Dixon, D. A.; Matson, D.; Autrey, T.; Liu, S.-Y. "3-Methyl-1,2-BN-cyclopentane: a promising H_2 storage material?" *Dalton Trans.* **2013**, *42*, 611-614. [10.1039/C2DT31617J]

10) Campbell, P. G.; Ishibashi, J. S. A.; Zakharov, L. N.; Liu, S.-Y. "B-Methyl Amine Borane Derivatives: Synthesis, Characterization and Hydrogen Release" *Aust. J. Chem.* **2014**, *67*, 521-524. [10.1071/CH13198]

11) Chen, G.; Zakharov, L. N.; Bowden, M. E.; Karkamkar, A. J.; Whittemore, S. E.; Garner, E. B, III.; Mikulas, T. C.; Dixon, D. A.; Autrey, T.; Liu, S.-Y. "Bis-BN Cyclohexane: A Remarkably Kinetically Stable Chemical Hydrogen Storage Material" *J. Am. Chem. Soc.* **2015**, *137*, 134-137. [10.1021/ja511766p]

* Highlighted in:
C&EN online - [link]
JACS Spotlights (*J. Am. Chem. Soc.* **2015**, *137*, 551-552.) - [link]

12) Kukolich, S. G.; Sun, M.; Daly, A. M.; Luo, W.; Zakharov, L. N.; Liu, S.-Y. "Identification and Characterization of 1,2-BN Cyclohexene Using Microwave Spectroscopy" *Chem. Phys. Lett.* **2015**, *639*, 88-92. [10.1016/j.cplett.2015.09.009]

13) Kumar, A.; Ishibashi, J. S. A.; Hooper, T. N.; Mikulas, T. C.; Dixon, D. A.; Liu, S.-Y.; Weller, A. S. "The Synthesis, Characterization and Dehydrogenation of Sigma-Complexes of BN-Cyclohexanes" *Chem. Eur. J.* **2016**, *22*, 310-322. [10.1002/chem.201502986]

14) Giustra, Z. X.; Ishibashi, J. S. A.; Liu, S.-Y. "Homogeneous Metal Catalysis for Conversion Between Aromatic and Saturated Compounds" *Coord. Chem. Rev.* **2016**, *314*, 134-181. [10.1016/j.ccr.2015.11.006]

15) Whittemore, S. M.; Bowden, M.; Karkamkar, A.; Parab K.; Neiner, D.; Autrey T.; Ishibashi, J. S. A.; Chen, G.; Liu, S.-Y.; Dixon, D. A. "Blending Materials Composed of Boron, Nitrogen and Carbon to Transform Approaches to Liquid Hydrogen Stores" *Dalton Trans.* **2016**, *45*, 6196-6203. [10.1039/c5dt04276c]

16) Brooks, K. P.; Bowden, M. E.; Karkamkar, A. J.; Houghton, A. Y.; Autrey, S. T., Coupling of exothermic and endothermic hydrogen storage materials. *J. Power Sources* **2016,** *324*, 170-178.

17) Giustra, Z. X.; Chou, L.-Y.; Tsung, C.-K.; Liu, S.-Y. "Kinetics of $-CH_2CH_2-$ Hydrogen Release from a BN-cyclohexene Derivative" *Organometallics* **2016**, *35*, ASAP. [10.1021/acs.organomet.6b00412]

Table of Contents

1. Introduction

1.1. Background

Among the plans to increasingly meet the world's energy demands with sustainable and renewable resources, proposals to implement a molecular hydrogen-based fuel economy have garnered considerable support.[1] Much of this support has been directed specifically at efforts to replace existing fossil fuel-based transportation systems with hydrogen-powered equivalents.[2] In turn, recent technological advances have led to encouraging results in a number of pilot programs involving fuel cell electric vehicles (FCEVs) for both public and private use.[2c,3] Indeed, certain auto manufacturers, have already initiated small-volume production of FCEVs for general commercial distribution.[3b]

In spite of these gains, an acute need remains for a safe and efficient means of storing hydrogen for use in FCEVs, all current models of which are powered by proton exchange membrane (PEM) fuel stacks.[3b,4] The current state of the art for vehicular applications consists of carbon nano-fiber tanks that can store up to 700 bar (10,000 psi) of compressed hydrogen gas.[5] An analysis by Hua in 2011, however, concluded this technology was unlikely to successfully meet the DOE's ultimate targets[6] for volumetric H_2 capacity and cost.[7] The density of liquefied hydrogen is nearly two-fold higher than that of the compressed gas, but the condensation process is significantly energy intensive, potentially consuming up to 33% of the total storable energy.[8] The low temperatures also typically required for effective physisorption of H_2 in porous materials, e.g. metal-organic frameworks, likewise limit the practicality of this approach.[9]

The evident drawbacks to the methods discussed above have led to increased focus on hydrogen storage strategies involving chemisorption of hydrogen, i.e. the fixation of H_2 in the form of multiple X–H bonds, where X may be a metal, carbon, or heteratom.[10] In certain cases, this mode of storage can afford particularly high gravimetric H_2 capacities. The theoretical % wt. H_2 of ammonia borane (NH_3BH_3, AB), for example, is 19.6%. This, combined with favorable H_2 release kinetics under mild conditions, has attracted considerable research interest in AB and its derivatives as chemical hydrogen storage materials.[11] One serious obstacle to the adoption of AB for vehicular application, however, lies in the difficulty in cleanly regenerating the spent dehydrogenated fuel. Under conditions for thermal decomposition, AB often forms complex mixtures of BN-polymers and borazine,[12] with the latter acting as a notable poison to PEM fuel cells. While several general regeneration protocols have been developed for AB, none are particularly amenable to on-board implementation owing to the use of toxic or otherwise hazardous reagents.[13]

Another challenge to the use of AB as a fuel for hydrogen-based transportation lies in its relatively high melting point (mp = 104 ºC). Ideally, a new alternative vehicular fuel should instead be a pumpable liquid[14] under ambient conditions. This property is critical to the material's successful reception by the general public because it would allow for distribution and consumption *via* the same, well-established networks and technologies used for liquid petroleum-based energy resources today.[15, 16] Indeed, many assessments[1c,2] have pointed to the significant time and expense required to design,

construct, and regulate a wholly new distribution infrastructure for compressed H_2 as a major impediment to the early economic viability of such a fuel source.[17]

The particular imperative of a *liquid-phase* hydrogen storage material has reinvigorated interest in certain so-called organic chemical hydrides,[18] primarily cyclic hydrocarbons such as methylcyclohexane[19] and decalin. Both the dehydrogenation of these materials, and their corresponding regeneration from the aromatic spent fuels have been extensively studied since the early 1950s; the modern-day field thus features many examples of mature and sophisticated catalytic systems for achieving these reactions.[20] Owing to the intrinsically high endothermicity of H_2 release from vicinal C–H bonds,[21] however, nearly all dehydrogenation processes of cyclic hydrocarbons require temperatures between 200–400 ºC. This range lies well above the typical operating temperature of PEM fuel cells (~80 ºC), which in turn precludes the possibility of driving the reaction using only waste heat from an FCEV's engine.

In 2006, however, Crabtree and co-workers demonstrated that replacement of cycloalkane CH_2 units with NH groups could significantly lower the overall endothermicity of dehydrogenation.[22] Subsequently, numerous groups have investigated the potential of saturated nitrogen-containing heterocycles to act as liquid chemical hydrogen storage materials.[23,24] *N*-ethyl-perhydrocarbazole (NEC-H_{12}) in particular has since emerged as a leading candidate;[25] heterogeneous catalysts selective for full dehydrogenation to N-ethylcarbazole (NEC) have been reported by Pez[26] and others.[27] Although NEC is a solid under ambient conditions (mp = 68 ºC), modestly limiting conversion in dehydrogenation reactions yields a liquid product mixture.[27d] Likewise, Tsang has developed conditions for the complete hydrogenation of neat, molten NEC back to NEC-H_{12},[28] thereby establishing an efficient all-liquid fuel cycle.

1.2. Project Design

For the current project, we sought to achieve a similar measure of improvement over current amine-borane-based hydrogen storage materials by incorporating NH_2BH_2 units into carbocyclic structures to form saturated carbon-boron-nitrogen (CBN) heterocycles. We hypothesized this approach would confer a number of advantages, chief among them that the CBN materials' rigid carbon-based frameworks would enforce greater selectivity toward a single, well-defined dehydrogenation product. Such selectivity was deemed likely to correspond to less contamination of the H_2 released with additional volatile, oligomeric species. It would also presumably allow for simplified procedures to regenerate the starting material from the spent fuel. The highly organic, relatively low molecular weight characteristics of our proposed CBN heterocycles was also conjectured to more greatly favor the probability that they would be liquid under typical storage conditions. Lastly, the combination of exergonic BN and endergonic -CH_2–CH_2- (CC) dehydrogenation within the same molecular framework was predicted to result in net thermoneutrality with respect to free energy for the overall process (Table 1).[29] Such thermodynamics are indicative of reaction reversibility, which again would potentially facilitate more efficient methods to recycle spent fuel materials.

Table 1. Calculated (CCSD(T)) overall thermodynamics for isolated BN and CC dehydrogenation reactions and their combined occurrence in a single molecular entity.

Reaction	ΔH_{298K} (kcal mol^{-1})	ΔG_{298K} (kcal mol^{-1})
$H_3N{-}BH_3 \longrightarrow H_2N{-}BH_2 + H_2$ (AB)	–5.1	–13.6
$H_3C{-}CH_3 \longrightarrow H_2C{=}CH_2 + H_2$	+32.6	+23.9
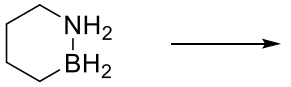 (J)	+27.9	+1.9

In our effort to meet the DOE technical targets for either vehicular or non-automotive applications, this project aimed to synthesize, characterize, and optimize the hydrogen storage properties of three different classes of CBN materials: 1) potentially liquid systems for efficient low-temperature, high-purity H_2 release, 2) potentially reversible systems for facile on-board regeneration, and 3) potentially high % wt. H_2 systems for long-term, off-board storage (Figure 1). Detailed summaries of the experimental findings for each individual material are provided in Section 2. Supplementary computational results are collectively reviewed in Section 3 as a separate topic.

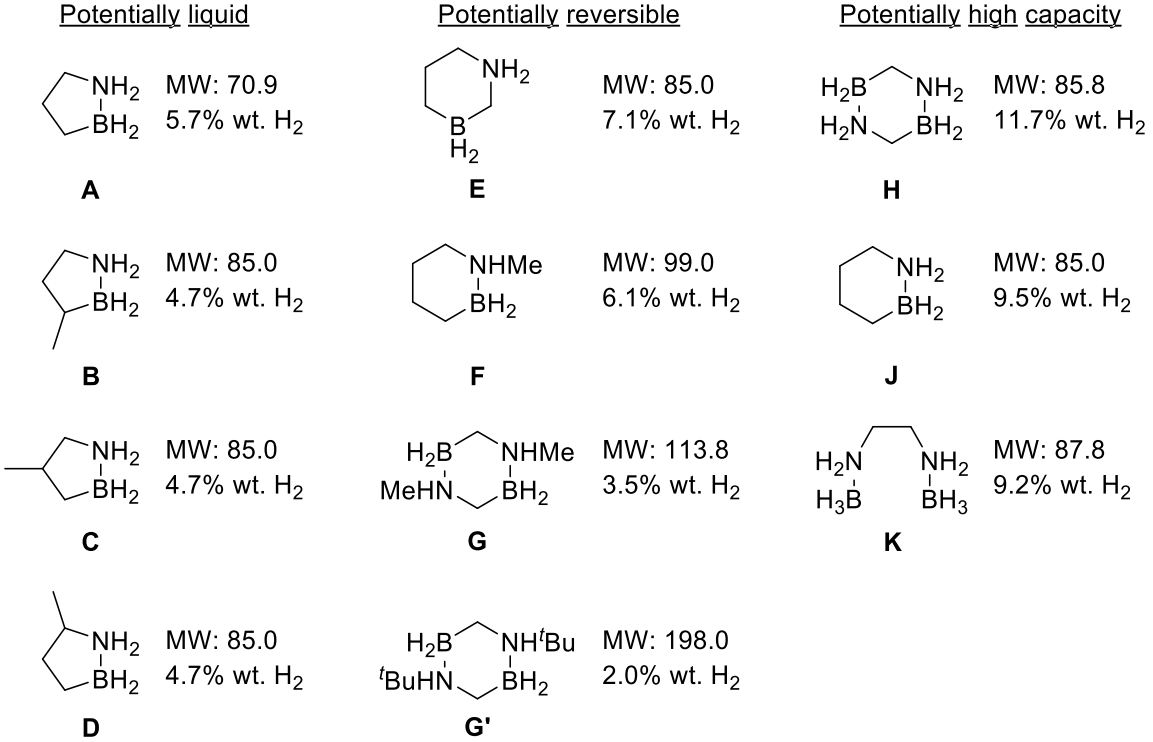

Figure 1. Theoretical gravimetric H_2 capacities of project target materials. For **A–D**, **G**, **G'**, and **K**, the given value is based on BN dehydrogenation alone.

1.3. Rationale for Target Material Classes

Reasons for the general desirability of a hydrogen storage material with an all-liquid fuel cycle have already been discussed in part in Section 1.1. In addition to the advantages enumerated above, effective manipulation of a liquid system either for transportation or consumption would presumably not require dilution by a solvent (as in the case of a solid material) nor the use of particularly cumbersome apparatus (as for compressed gas). A liquid material therefore affords the greatest opportunity to maximize storage efficiency through minimization of the mass and volume of auxiliary system components (Balance of Plant).

For reasons detailed in Section 1.2, we had initially postulated that members of the 1,2-BN-cyclopentane series **A**−**D** were the most likely candidates among our proposed CBN materials to exist as liquids under standard storage and operating conditions. Indeed, we had already found this to be so for **B** in the course of our previous DOE project.[30] Thus, for the current project, we focused on evaluating the second part of our hypothesis, i.e. that the well-defined, largely carbon-based architecture of these compounds would also contribute to mitigation of the formation of volatile impurities known to negatively impact PEM fuel cell performance (see Section 1.1 for examples). We proposed to verify the purity of the H_2 produced from **A**−**D** primarily through the use of residual gas analysis (RGA) and mass spectroscopy-coupled thermogravimetric analysis (TGA-MS)

It was assumed that as the proportion of inorganic units in the molecule increased, the bulk CBN material was more likely to be a solid, rather than a liquid, under ambient conditions. We surmised, however, that such solid materials would exhibit advantageously higher thermal stability than their liquid counterparts owing to more restricted molecular motion in the solid versus liquid state.[31] Additionally, incorporation of more NH_2BH_2 units would also increase the material's theoretical % wt. H_2 capacity (compare **H** versus **J**); moreover, release of the H_2 thus stored would presumably be exothermic, rendering it overall more thermodynamically favorable than endothermic release from carbon-carbon units. Thus, in addition to liquid materials appropriate for vehicular use, this project also targeted several high-stability, high-capacity hydrogen storage systems appropriate for use in conjunction with relatively stationary equipment.[4,32] Notable potential applications in this regard include emergency back-up[33] and remote-area[34] power supply systems, forklifts,[35] and residential combined heat and power (CHP) systems.[1d,e]

In addition to adequate % wt. H_2 capacity and material stability, recyclability is another feature vital to maximizing the efficacy of our CBN compounds. Early on, however, we discovered complete BN dehydrogenation of unsubstituted 1,2-BN-cycloalkanes resulted in the formation of trimeric products (see either Ref. 30 or Section 2 for details). Notably, the starting materials could not be directly recovered from these species; instead, a two-step protocol involving first digestion of the trimer and then reduction with some hydride source (either $LiAlH_4$ or BH_3•THF) was required.[30] To investigate the possible efficacy of milder regeneration methods (ideally using H_2 itself as the reductant), we targeted several *N*-substituted CBN materials. This substitution would presumably ensure the formation of monomeric spent fuel products. We hypothesized that as isolated aminoboranes, these species would be more amenable to undergo direct reduction back to the fully charged fuels. We also proposed that materials with partial

frustrated Lewis pair (FLP) characteristics, i.e. compound **E**, would similarly be more disposed to exhibit facile reversibility of BN dehydrogenation.

2. Individual Materials

2.1. Compound A

1,2-BN-Cyclopentane (**A**) was synthesized as shown in Scheme 1 starting from addition of $NaN(TMS)_2$ (TMS = trimethylsilyl) to allyl bromide.[36] Hydroboration of allylic amine **1** with BH_3•NEt_3 afforded cyclized intermediate **2** with loss of trimethylsilane. Hydride addition to crude **2** followed by desilylation-protonation with HF•pyridine then furnished **A** as a white solid (mp = 36–37 ºC).

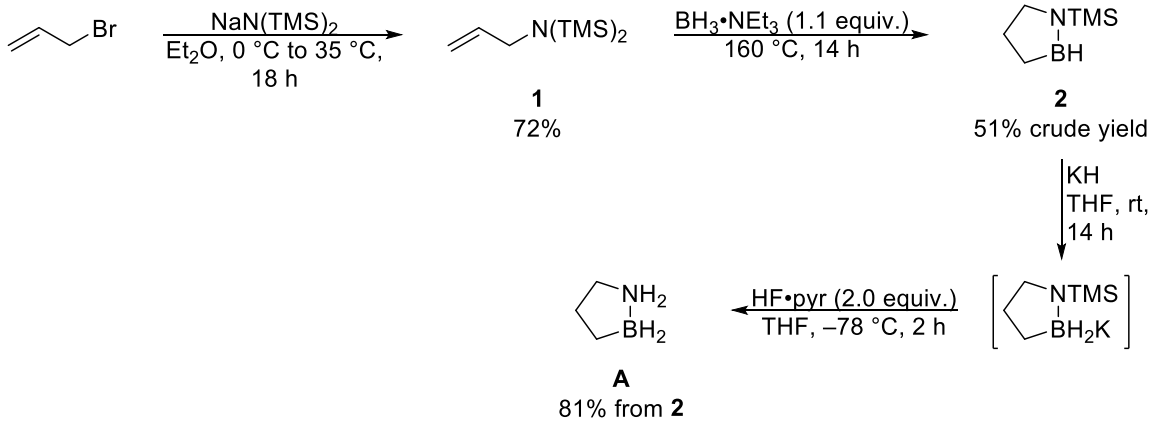

Scheme 1. Synthesis of **A** starting from allyl bromide. (Note: HF•pyridine is both corrosive and toxic; calcium gluconate should be kept on hand during any manipulation.)

Thermal decomposition of neat **A** at 150 ºC results in release of two H_2 equivalents. Residual gas analysis revealed no contamination of the gas stream thus produced by other volatile species. Compound **A** was not selected for further detailed investigation because it is not a liquid at room temperature and because of its low thermal stability at room temperature.

2.2. Compound B

3-Methyl-1,2-BN-cyclopentane (**B**) was originally synthesized [37] from crotyl bromide according to the same procedures as **A**. In order to efficiently prepare the decagram quantities of material required for fuel cell testing (*vide infra*), however, a more optimized protocol was required. For this large-scale route, crotyl alcohol was chosen as a more cost-effective starting material than crotyl bromide; alcohol-to-bromide conversion could be readily achieved with PBr_3 on mole scale (Scheme 2). Displacement of the bromide with NaHMDS also proceeded smoothly on mole scale. Hydroboration of the resulting allylic amine **3** with BH_3•NEt_3 afforded cyclized intermediate **4**; in order to enable simpler purification schemes for subsequent steps, at this stage, **4** was not carried through crude as done previously, but rather partially purified by fractional vacuum distillation (65 ºC @ 53 Torr).

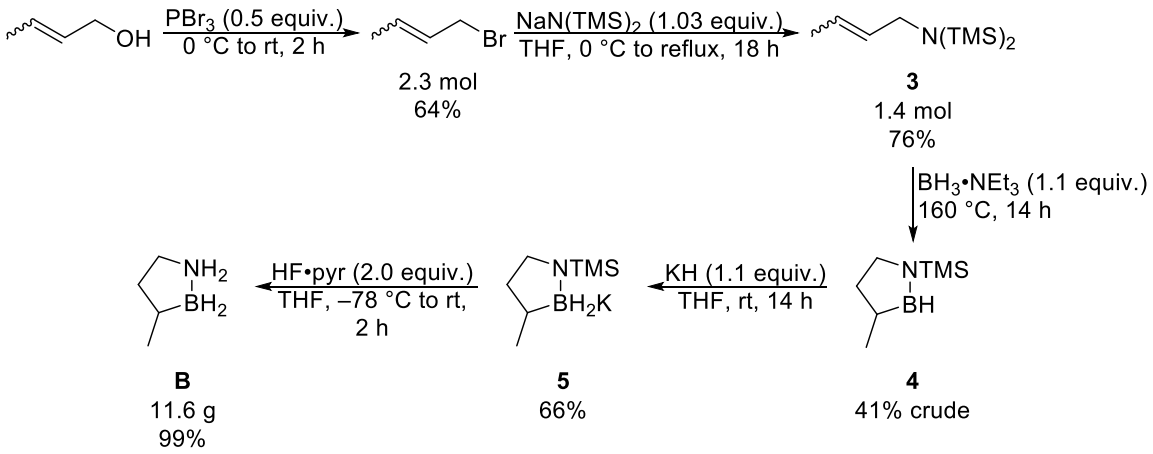

Scheme 2. Large-scale synthesis of **B** starting from crotyl alcohol. (Note: HF•pyridine is both corrosive and toxic; calcium gluconate should be kept on hand during any manipulation.)

As an aside, while BH_3•NEt_3 proved at the time a serviceable reagent for the hydroboration reaction, other borane adducts were later investigated in the hopes of achieving higher product selectivity. While BH_3•THF appeared to react with **3** at room temperature, the formation of **4** was only observed at higher temperatures (>70 ºC) (Figure 2); under such conditions, product selectivity proved worse than with BH_3•NEt_3. Likewise, BH_3•PPh_3 only reacted at high temperatures and did not afford any improved selectivity (Figure 3). Gratifyingly, however, the use of BH_3•SMe_2 at 65 ºC for 24 h appeared to yield **4** with only trace boron-containing impurities (Figure 4).

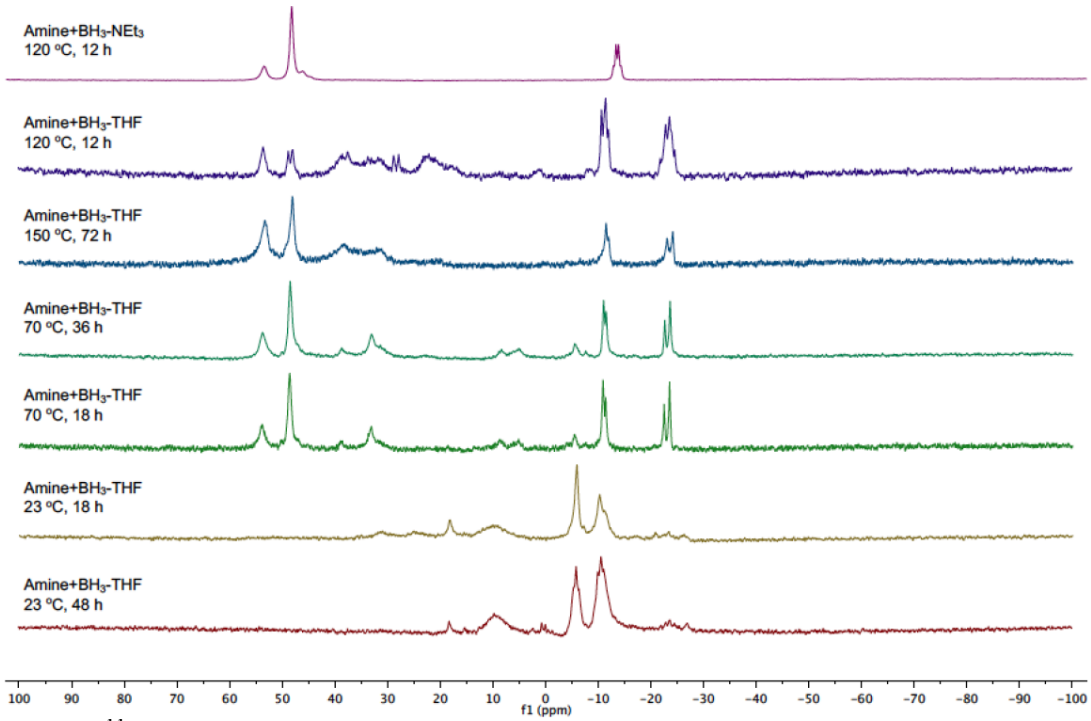

Figure 2. ^{11}B NMR spectra of hydroboration reactions of **3** with BH_3•THF under various conditions; spectrum from reaction with BH_3•NEt_3 (top) included for comparison.

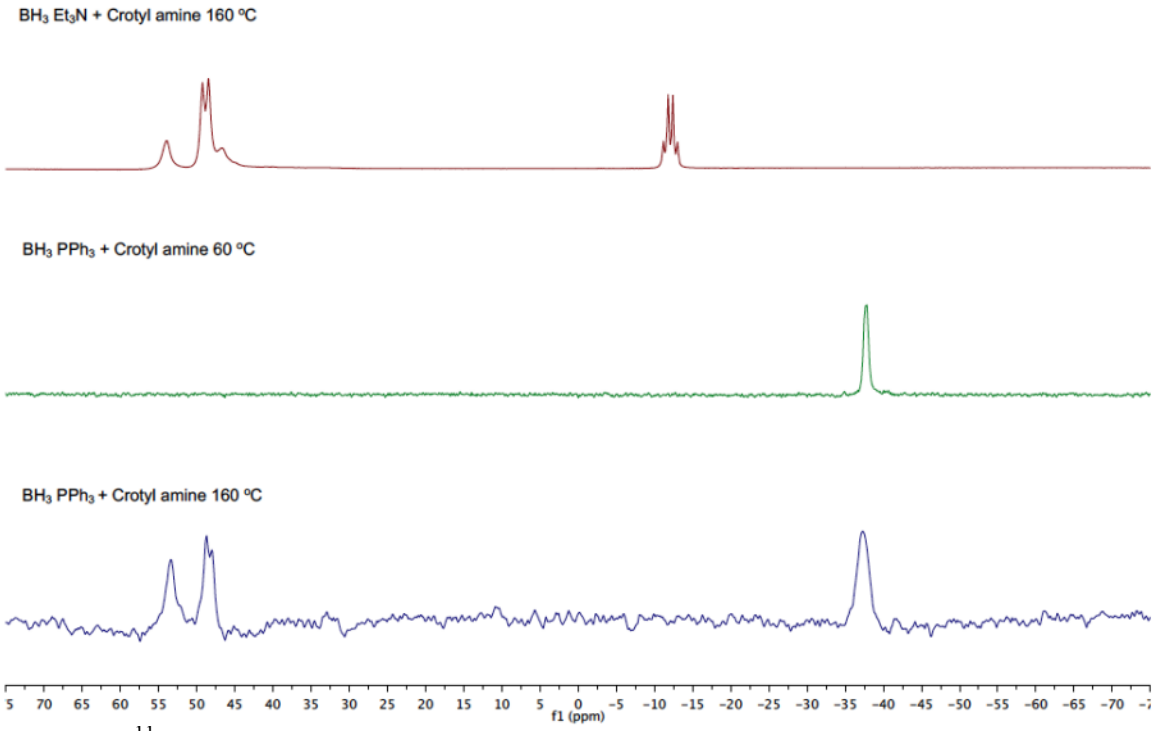

Figure 3. ^{11}B NMR spectra of hydroboration reactions of **3** with BH_3•PPh_3 at 60 °C (middle) and 160 °C (bottom); spectrum for reaction with BH_3•NEt_3 (top) included for comparison.

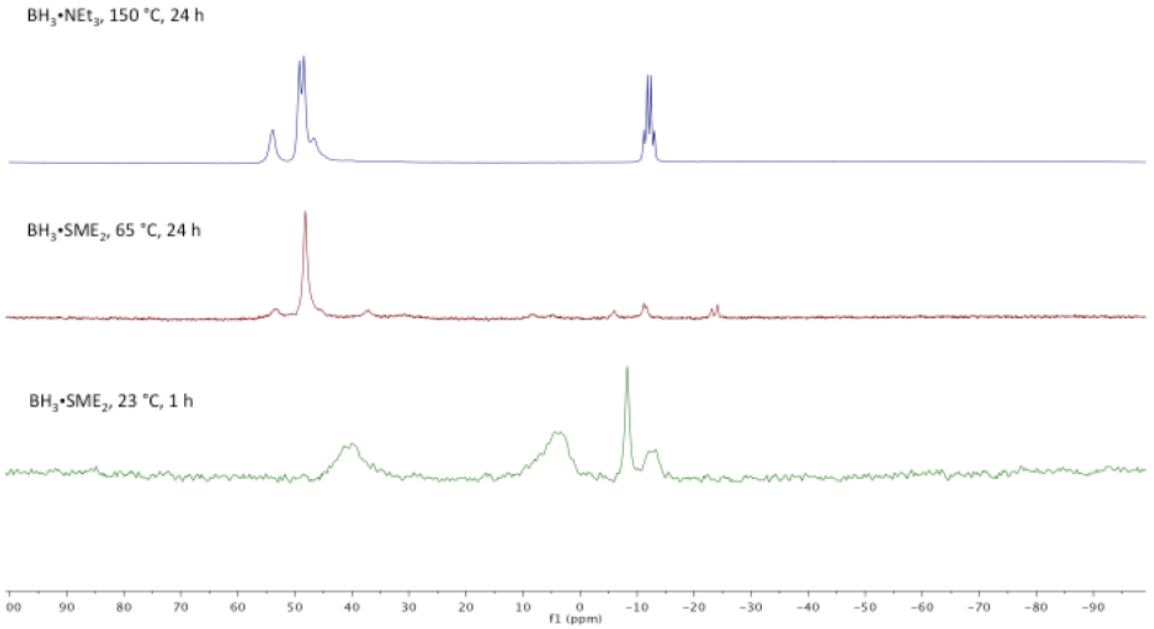

Figure 4. ^{11}B NMR spectra of hydroboration reactions of **3** with BH_3•SMe_2 at 65 °C (middle) and 23 °C (bottom); spectrum for reaction with BH_3•NEt_3 (top) included for comparison.

Addition of KH to **4** produced intermediate **5**, which could be purified by trituration

with pentane. Desilylation-protonation of **5** with HF•pyridine at –78 ºC now proceeded in near quantitative yield on a multi-gram scale. Based on this synthetic sequence, a process flow diagram was developed for the production of **B** at a rate of 100 kg-h^{-1} (Figure 5).

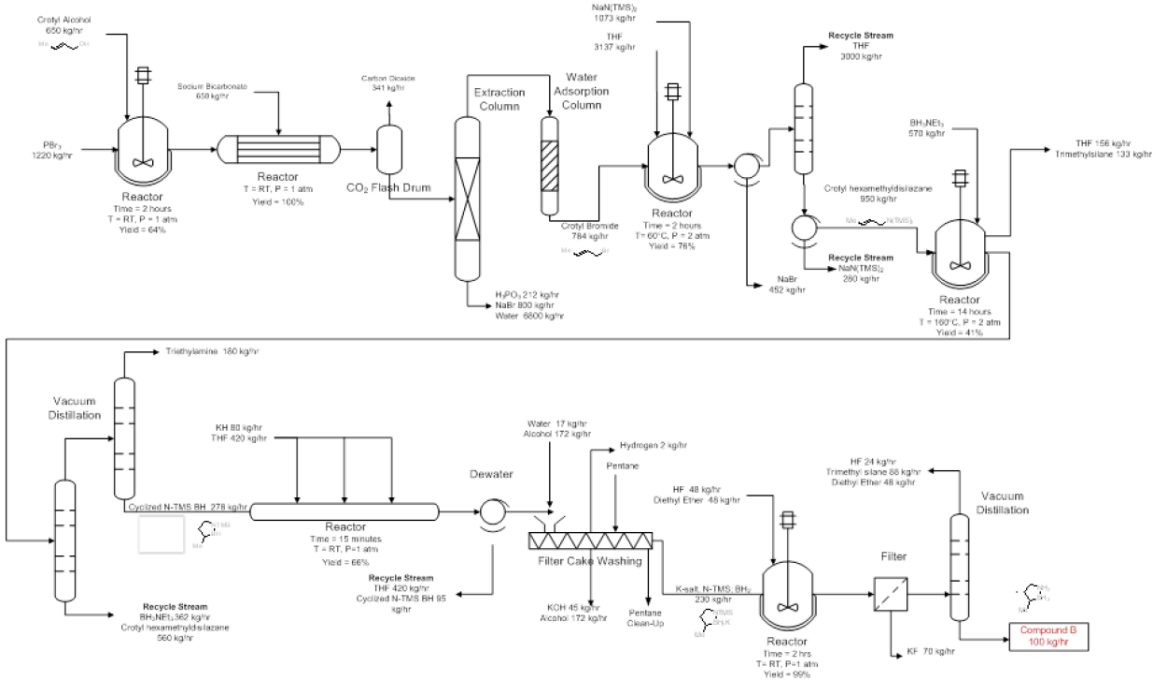

Figure 5. Process flow diagram for proposed synthesis of **B** at at a rate of 100 kg-h^{-1}.

The viscosity of **B** was measured using a dynamic mechanical rheometer;[38] at room temperature, it was found to be 25±5 cP, comparable to that of ethylene glycol (16 cP)[39] and suitable for pumping (<500 cP).[40] The viscocity did not display significant variation over a temperature range of 15–50 ºC.

The gas-phase dipole moment of **B** was calculated (MP2/aug-c-pVTZ) as 4.71 D along the B–N axis, similar in magnitude to that predicted for DMSO (4.23 D).[38] The polarity of **B** was also experimentally evaluated via solvatochromic studies with Reichardt's dye (Figure 6). Based on the $E_T(30)$ scale,[41] the polarity of **B** appeared most similar to that of methanol ($E_T(30)$ = 54.9 kcal-mol^{-1} for **B** versus 55.5 kcal-mol^{-1}).

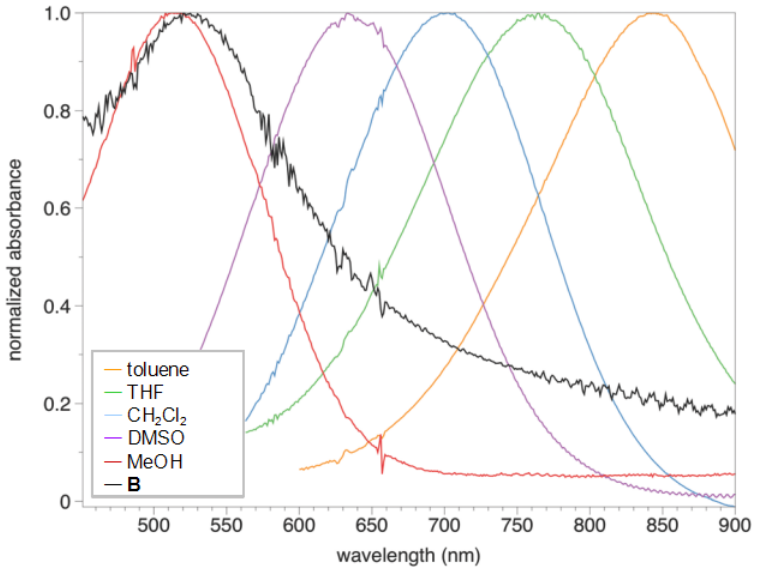

Figure 6. Solvatochromic studies of **B** using Reichardt's dye and comparison with some common organic solvents.

The thermal stability of neat **B** was evaluated using TGA-MS (Figure 7).[38] No weight loss was observed below 40 ºC, but beginning at 50 ºC, 0.25% weight loss occurred over 3 h; this loss increased to 1.5% at 60 ºC. The coupled mass spectrometer revealed the lost mass to consist almost exclusively of H_2, with residual solvent making up the rest.

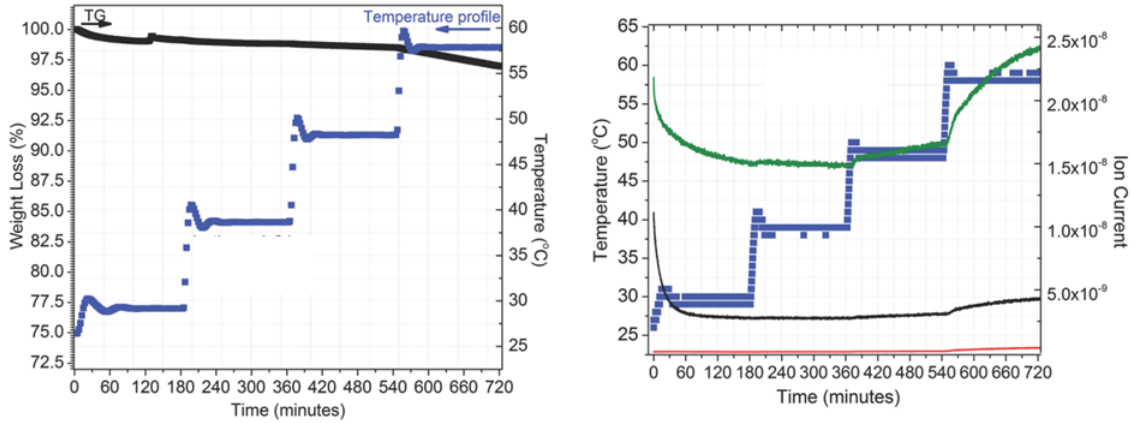

Figure 7. TGA (left) and coupled MS (right) of **B** from 30–60 ºC with ramping at 10 ºC-min^{-1} between isothermal periods (3 h). For MS traces, green: H_2, black: Et_2O, and red: THF).

Thermal decomposition of **B** at 150 ºC proceeds cleanly to form the trimer **6**,[37] a low melting solid[42] (mp = 28–30 ºC; Scheme 3). Residual gas analysis of the reaction detected only H_2 and trace amounts of **B** (Figure 8).[38] Other volatile species such as borazine were not observed, in contrast to the decomposition of ammonia borane. Based on the experimentally extrapolated boiling point of 335 ºC,[37] the vapor pressure of **B** was calculated as between 1–3 Torr at 150 ºC, consistent with the RGA indications of non-volatility at that temperature. (The vapor pressures of **B** and **6** at 80 °C were also calculated using COSMO-RS; see Section 3.1.)

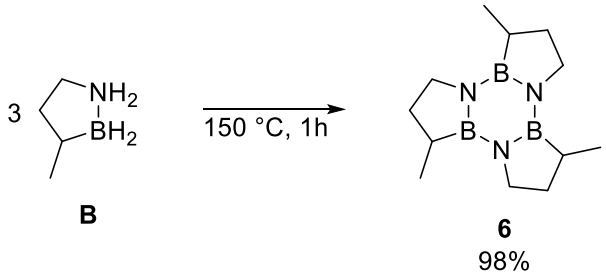

Scheme 3. Thermal decomposition of neat **B** to trimer **6** at 150 ºC.

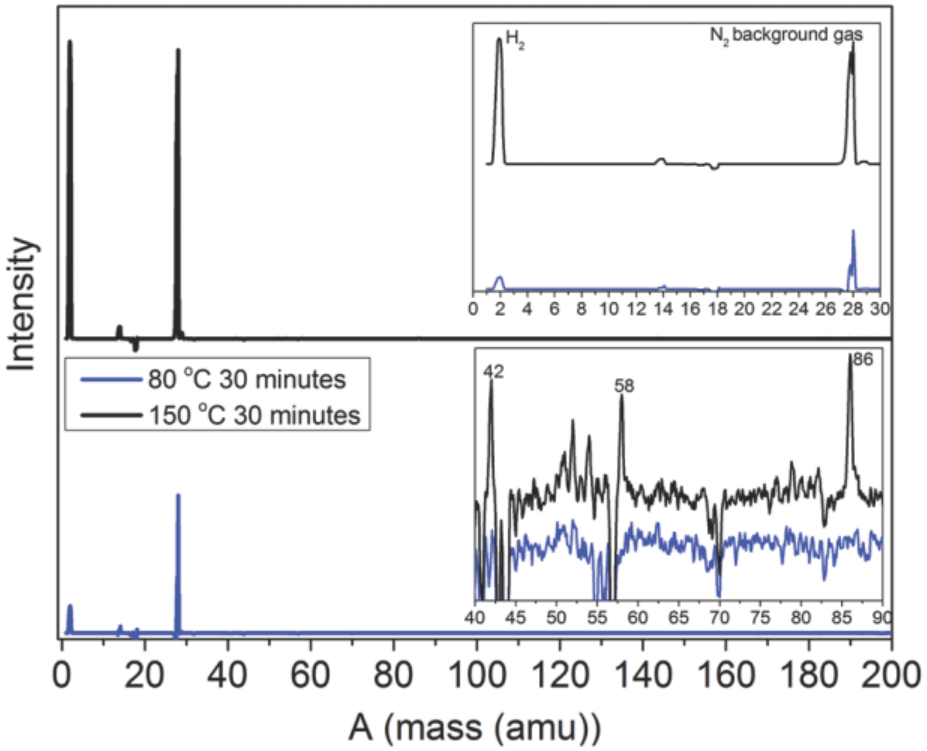

Figure 8. RGA spectrum of the gas stream produced by decomposition of neat **B** at 80 ºC (blue) and 150 ºC (black).

Notably, clean regeneration of **B** from trimer **6** could be achieved using methanol digestion to first form amine borate **7**, followed by reduction with $LiAlH_4$ (Scheme 4).[37]

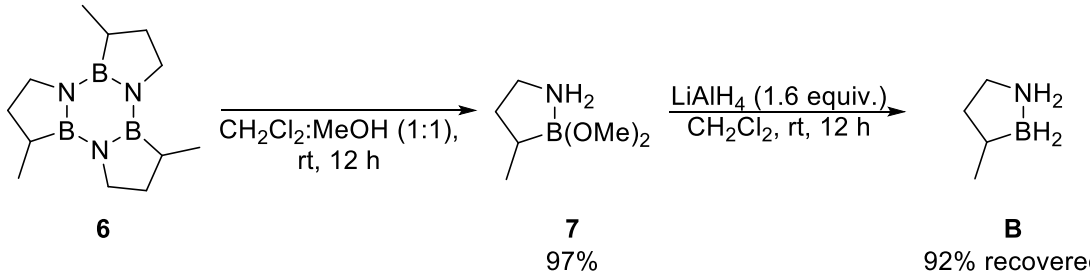

Scheme 4. Regeneration of **B** from **6** using step-wise methanol digestion and reduction with $LiAlH_4$.

The thermal decomposition of **B** at lower temperatures (90–140 ºC) was also studied using an automated gas burette (Figure 9). While the rate of decomposition did not appear to follow simple first- or second-order kinetic behavior, a linear relationship was determined to exist between $\ln(\tau_n)$ and 1/T, where τ_n is the time required to release *n* H_2 equivalents. The rate of decomposition at lower temperatures could thus be extrapolated from this relationship. Thus, the loss of one H_2 equivalent from **B** was predicted to occur in 2 d at 60 ºC and 150 d at 25 ºC.

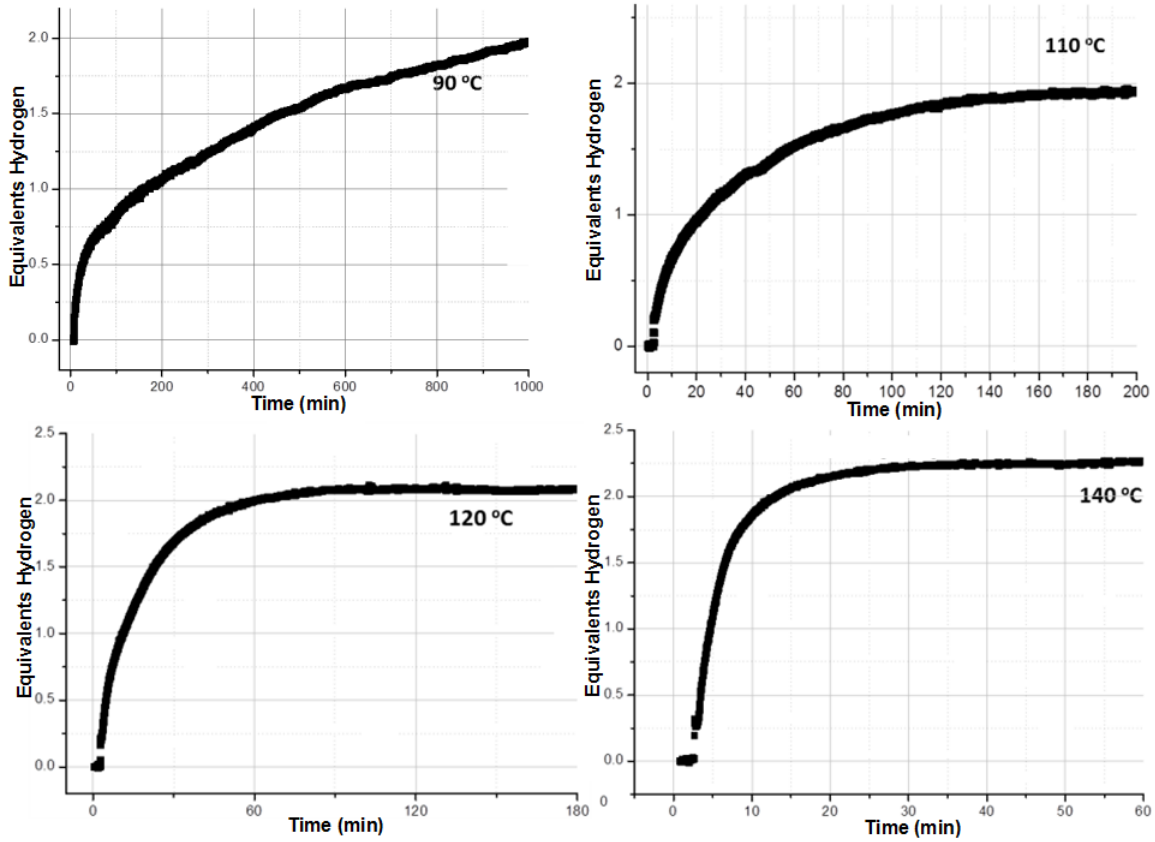

Figure 9. Automated gas burette measurements of thermal decomposition of neat **B** at various temperatures.

The above H_2 evolution traces were eventually found to fit a kinetic model of two first-order reactions occurring in series (Figure 10). This model could be represented by the equation:

$$C_{H_2} = 2 - e^{-k_1 t} + \left(\frac{k_1 e^{-k_2 t} - k_2 e^{-k_1 t}}{k_2 - k_1} \right)$$

in which C_{H_2} is the number of H_2 equivalents generated, and k_i are rate constants from the Arrhenius equation for the two sequential dehydrogenation reactions. Solving for k_1 and k_2 afforded activation energies for release of the first and second H_2 equivalents from **B** as 22.8 kcal-mol^{-1} and 34.6 kcal-mol^{-1}, respectively; the pre-exponential factors were likewise estimated as 1.30 x 10^{10} s^{-1} and 9.70 x 10^{15} s^{-1}, respectively.

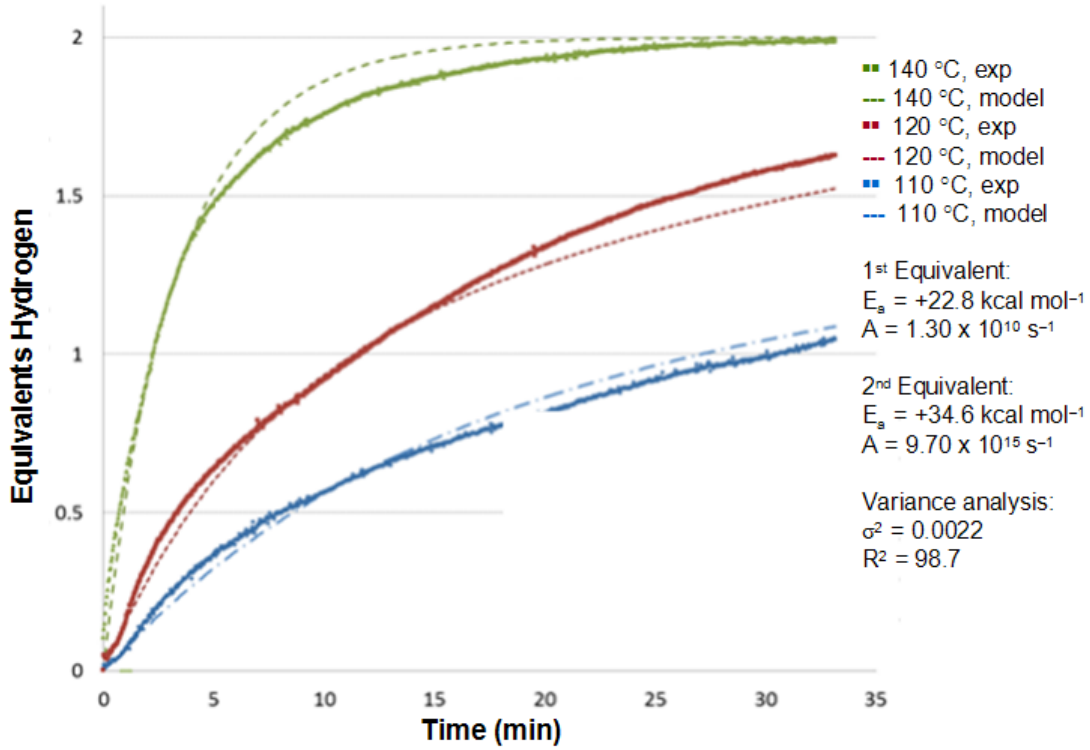

Figure 10. Overlay of experimental and modeled H_2 evolution traces from neat **B** heated at various temperatures, and derived Arrhenius parameters.

The solution-phase kinetics of the initial loss of H_2 from **B** were also studied using ReactIR. An N–H bending mode of **B** exhibits a unique IR frequency at 1600 cm^{-1}, thereby enabling quantitative monitoring of the disappearance of starting material. The initial concentration of **B** ($[\mathbf{B}]_0$) in a tetraglyme solution at 140 ºC was varied between 0.560 M and 1.283 M, and initial rates (r_i) were estimated based on linear regression of the respective portions of the substrate disappearance trends representing up to 20% conversion. A linear fit of $\ln(r_i)$ vs. $\ln([\mathbf{B}]_0)$ yielded a slope of 2 (Figure 11), indicating the rate of initial H_2 release from **B** follows a second-order concentration dependence. A subsequent Arrhenius analysis was performed by maintaining a constant initial concentration of 0.742 M and varying the reaction temperature from 100–160 ºC (Figure 12). This analysis yielded an activation energy (E_a) of 18.8 kcal-mol^{-1} and a pre-exponential factor (A) of 2.02 x 10^7 M^{-1}-s^{-1} for the initial dehydrogenation reaction of **B**.

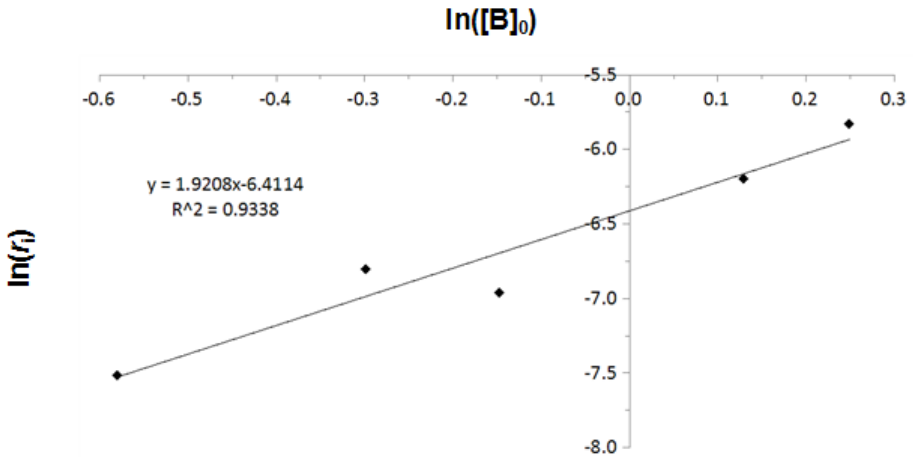

Figure 11. Reaction order determination by the initial rates method for the loss of the first H_2 equivalent from **B**.

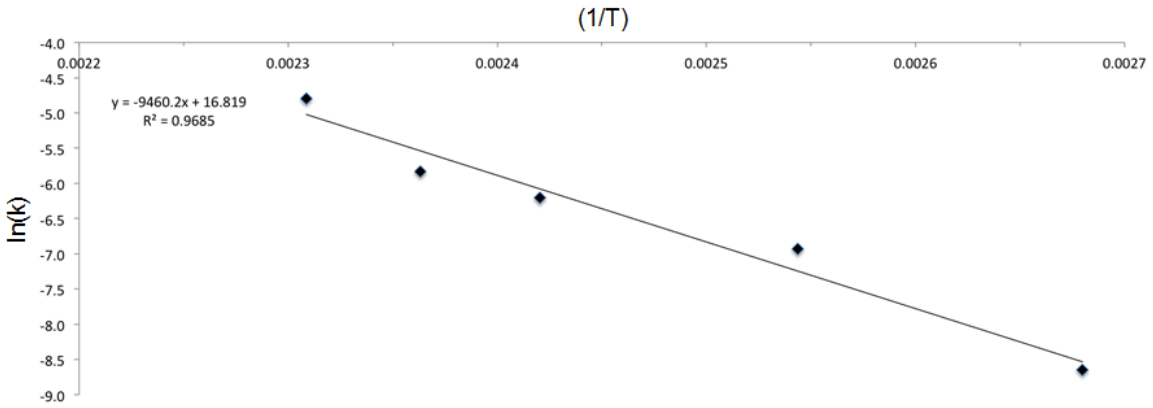

Figure 12. Arrhenius plot for for the loss of the first H_2 equivalent from **B**.

The mechanism of this reaction was also investigated computationally (geometry optimization using B3LYP/DZVP2 and energy calculations using G3MP2). Experimental evidence for a bimolecular process as the rate-determining step led us to consider the possibility of one unit of **B** first undergoing heterolytic B–N bond cleavage to generate the ring-opened isomer **B'**. Such bond dissociation has been previously invoked by Nguyen and Dixon[43] as part of their proposed mechanism for the overall decomposition reaction of AB. In their model, the free BH_3 thus generated subsequently interacted with a still intact molecule of AB to catalyze H_2 release.

Figure 13 depicts the analogous process in terms of **B**; starting from two separate molecules of **B**, B–N bond cleavage first generates one unit of **B'**. A bridging hydride interaction between the BH_2 groups of **B** and **B'** results in formation of complex **[B-B']**, which is lower in energy than the separate mixed species, but still less stable than the ring-closed starting materials. The lowest energy transition state (**TS-B**) for H_2 release from **[B-B']** involves intramolecular transfer of the bridging hydride from **B** to **B'**, while a proton from the NH_2 group of **B** simultaneously combines with another hydride of the **B'** unit to release H_2. Based on this calculated potential energy surface, the theoretical gas-phase enthalpy ($\Delta H^{\ddagger}$), entropy ($\Delta S^{\ddagger}$), and free energy of activation ($\Delta G^{\ddagger}$) of the

reaction could be determined (Table 2). The sizeable, negative $\Delta S^{\ddagger}$ value (–27.8 (cal-mol^{-1}-K^{-1}) in particular accords well with the experimental evidence for a bimolecular rate-determining step.

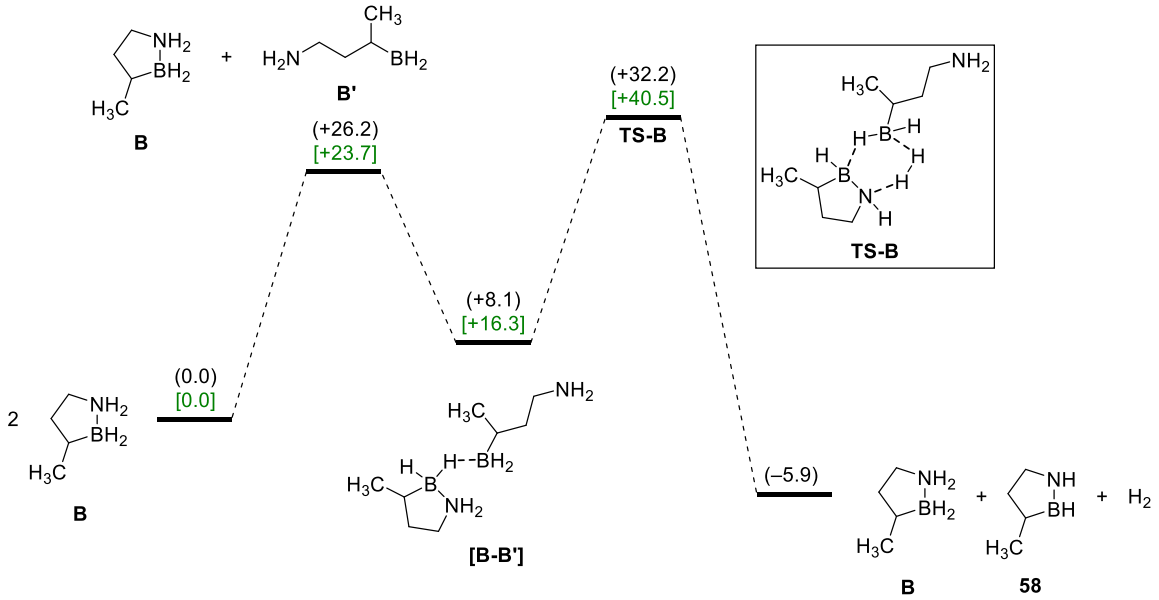

Figure 13. Potential energy surface for a proposed bimolecular H_2 release mechanism for **B**. Gas-phase enthalpy (black) and free energy [green] values (kcal-mol^{-1}) were calculated using G3MP2 (298K) based on geometries optimized using DFT at the B3LYP/DZVP2 level of theory.

Table 2. Computationally determined gas-phase enthalpy ($\Delta H^{\ddagger}$), entropy ($\Delta S^{\ddagger}$), and free energy of activation ($\Delta G^{\ddagger}$) (298 K) based on the potential energy surface shown in Figure 13. $\Delta S^{\ddagger}$ values are extrapolated from the calculated $\Delta H^{\ddagger}$ and $\Delta G^{\ddagger}$ values.

Reaction	$\Delta H^{\ddagger}$ (kcal mol^{-1})	$\Delta S^{\ddagger}$ (cal mol^{-1} K^{-1})	$\Delta G^{\ddagger}$ (kcal mol^{-1})
B → 58 + H_2	+32.2	–27.8	+40.5

The decomposition of **B** to **6** could also be catalyzed at 80 ºC either in toluene or neat using a variety of metal chloride salts.[37] Automated gas burette measurements revealed that $CoCl_2$ and $NiCl_2$ actually catalyzed release of the second H_2 equivalent from **B** more rapidly than the first (Figure 14). While $FeCl_2$ proved the least efficient catalyst in terms of rate of H_2 evolution (2 H_2 equiv. in 15 min), it was chosen for further study given its availability and low toxicity. It was found that the iron catalyst could be directly reused several times without loss of activity (Figure 15). Attempts to lower the catalyst loading from 5 mol% to 1 mol%, however, resulted in a significant decrease in the rate of H_2 evolution. The addition of mercury also drastically inhibited the catalyst's activity, suggesting the formation of iron nanoparticles as the active species (Figure 16). Indeed, X-ray analysis of the catalyst material after the reaction revealed a pattern consistent with that of Fe^0 nanoparticles with an average size of 3 nm (Figure 17).

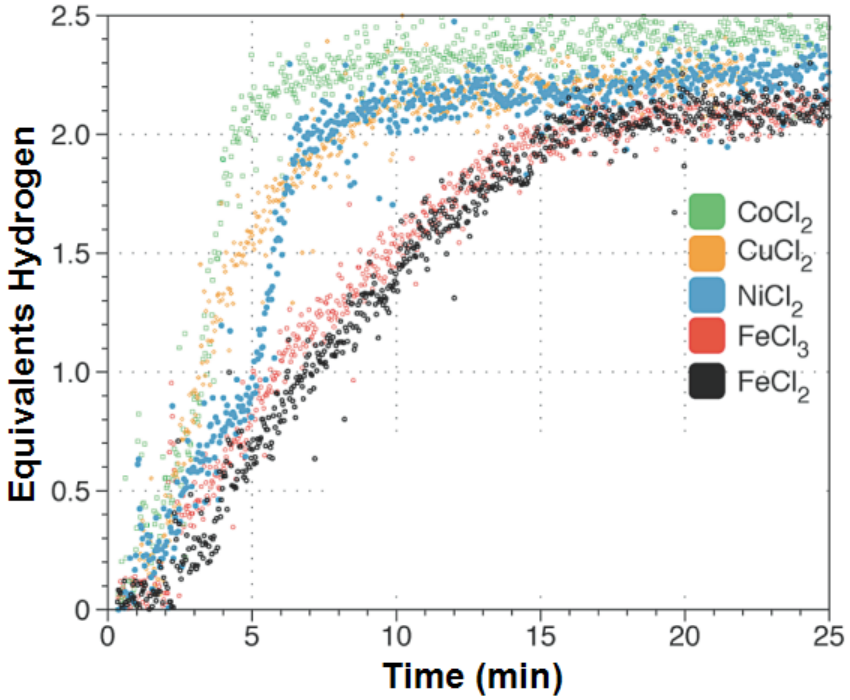

Figure 14. Automated gas burette measurements of metal chloride-catalyzed dehydrogenation of **B**. Conditions: 5 mol% catalyst, toluene, 80 ºC.

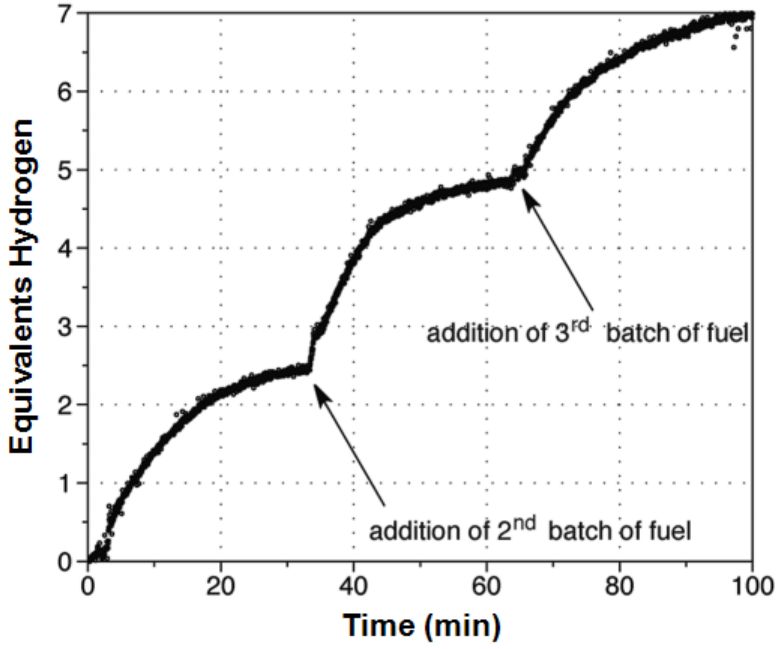

Figure 15. Automated gas burette measurements of $FeCl_2$-catalyzed dehydrogenation of **B** with multiple successive additions of substrate. Conditions: 5 mol% catalyst, neat, 80 ºC.

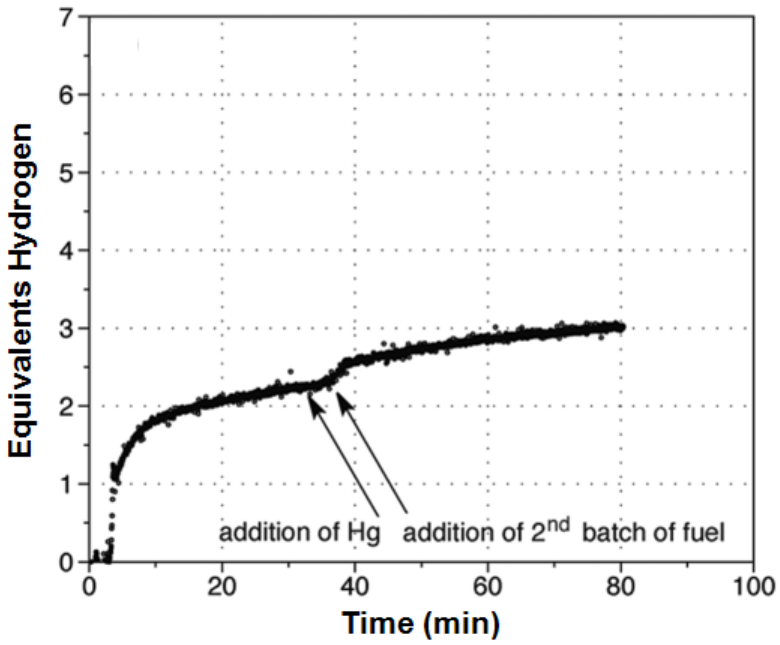

Figure 16. Automated gas burette measurements of $FeCl_2$-catalyzed dehydrogenation of **B** in the absence and presence of mercury. Conditions: 5 mol% catalyst, neat, 80 ºC.

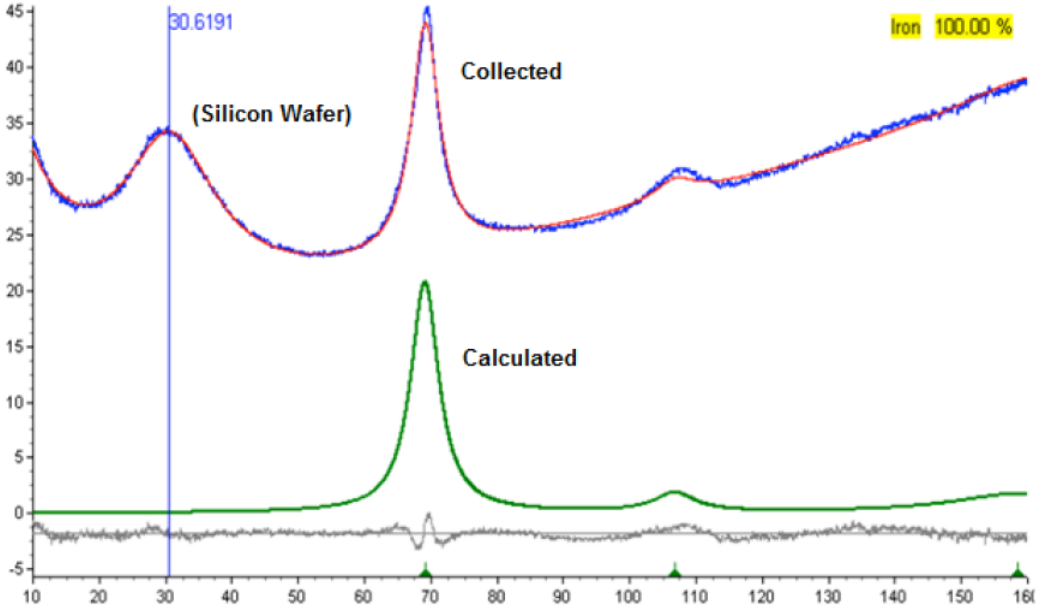

Figure 17. XRD spectrum measured for $FeCl_2$ catalyst material recovered from dehydrogenation reactions with **B**.

The ability to rapidly generate a clean stream of H_2 from substantial quantities of material led us to consider testing **B** as a means of powering a fuel cell. Specifically, we selected a 12 cell, 9.5 cm^2 active area PEM fuel cell stack developed by Protonex to provide 30 W of power (8.5 V at 4 A) at 0.3 sLpm H_2 consumption under steady state conditions. Based on such H_2 consumption requirements, it was predicted that 20 g of **B**

could supply sufficient H_2 (10 L) to power the stack for 30 minutes.

As shown in Figures 18 and 19, the test setup consisted of four major apparatus: a H_2 generation assembly, a H_2 storage assembly, a gas flow system assembly, and the fuel cell stack itself. It was found during initial testing that a dry ice condenser and activated carbon filter needed to be integrated into the flow system in order to isolate trace volatile organic contaminants from the H_2 supply generated from **B**. Flow of H_2 to the stack was controlled by a solenoid actuated pinch valve set to open for 250 ms at 10 s intervals. Air from a humidifier was fed separately to the stack at 60 ºC and 100% relative humidity. The stack operating temperature was maintained at 60 ºC while connected to a load bank operating in constant current mode.

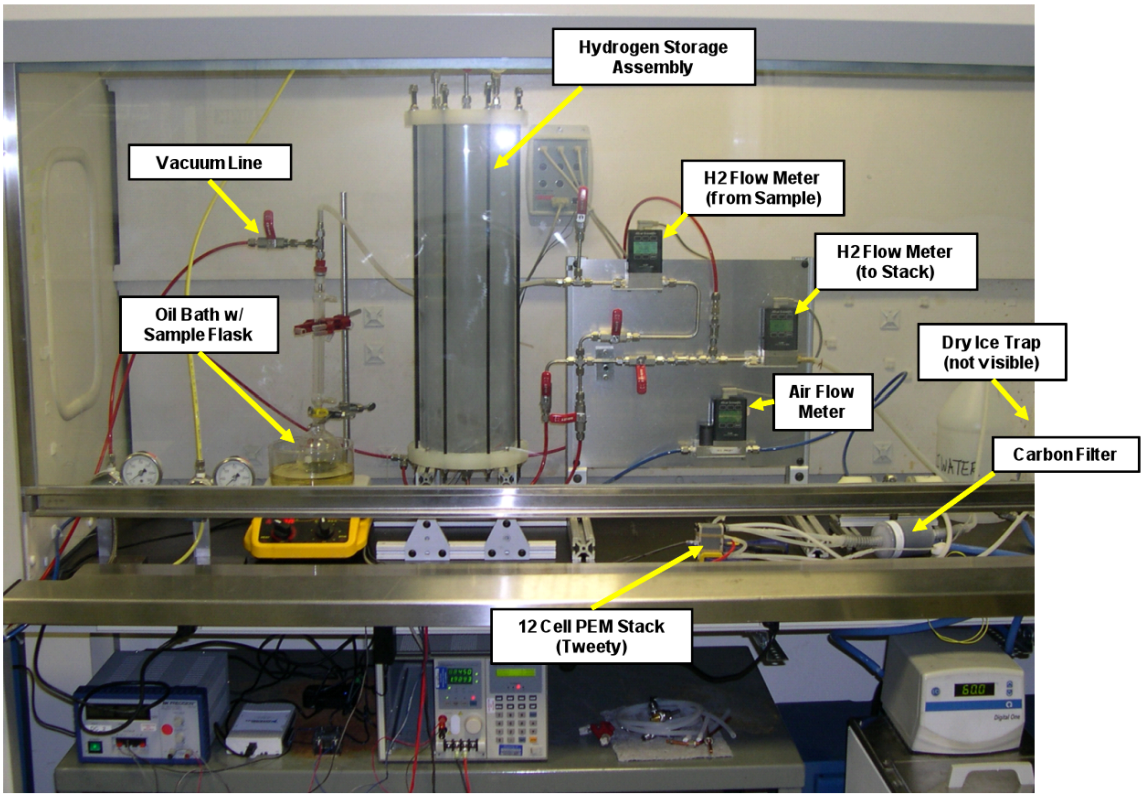

Figure 18. Photograph of actual fuel cell stack test assembly.

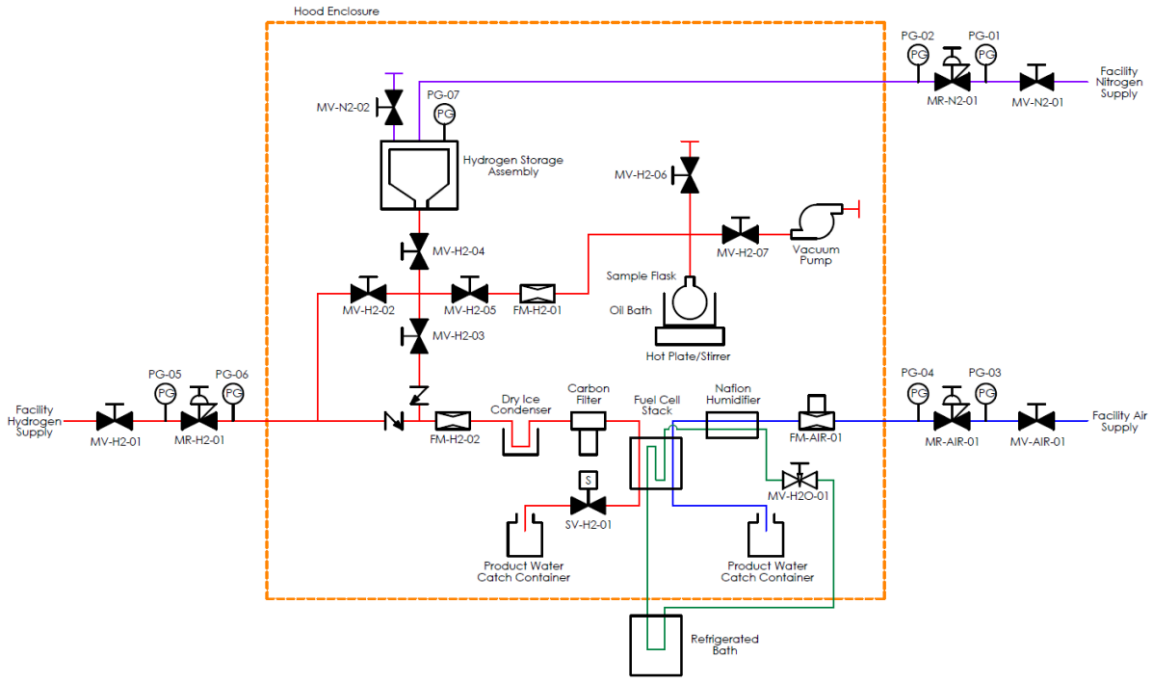

Figure 19. Engineering diagram of fuel cell stack test setup components and connections.

The stack was initially powered using facility H_2 before switching to H_2 collected and stored from $FeCl_2$-catalyzed decomposition of **B** at 80 ºC. While operating using H_2 from **B**, the stack voltage remained constant at 8.5 VDC (Figure 20), the same as when running on facility H_2. Notably, no change in stack performance was observed upon reverting to facility H_2 after the supply of H_2 from **B** had been exhausted.

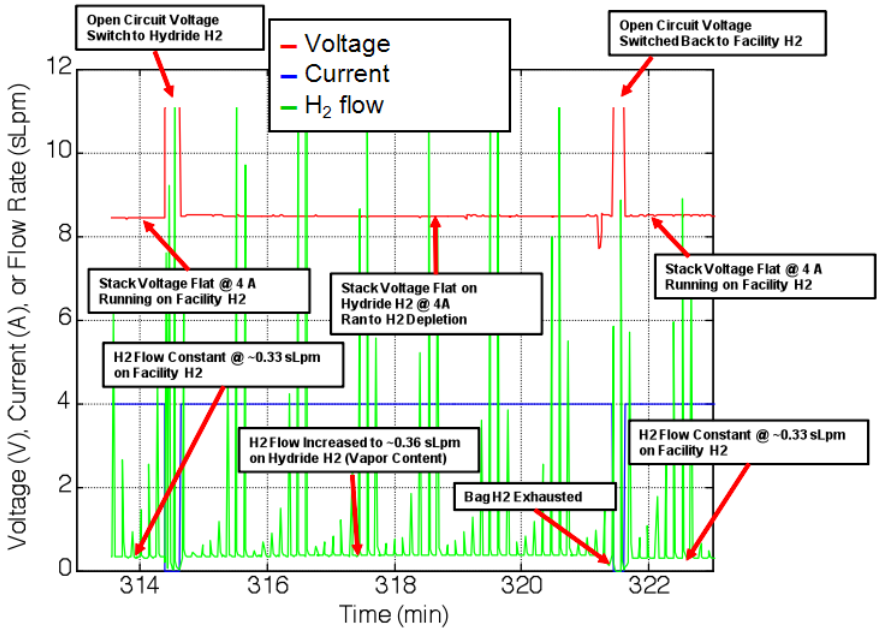

Figure 20. Real-time monitoring of fuel cell stack operating parameters.

It was hypothesized that combining **B** with other amine-borane hydrogen storage

materials might produce liquid fuel blends with improved properties regarding H_2 release, e.g. thermal stability, product selectivity, etc. To that end, the relative solubilities of **A**, **D**, ethane 1,2-diamineborane (**K**),[44] and AB in **B** were first investigated.[36] Based on ^{11}B NMR, less than 1% **K** dissolved in **B** at room temperature, and so this combination was down-selected and not considered further. Fortunately, however, **A**, **D**, and AB all proved readily soluble in **B**, leading to further characterization of these blends. While ^{11}B NMR ultimately demonstrated the mix of **A** and **B** to be thermally unstable with respect to **A**, a 1:1 liquid mixture of **D** and **B** proved more stable, releasing H_2 only at more elevated temperatures. Additionally, the mixture of products resulting from dehydrogenation of this blend remained a liquid material throughout the reaction; this stands in stark contrast to the formation of solid trimer **6** from the decomposition of neat **B**.

A blend of **B** and AB in a 2:1 molar ratio produced a fluid slurry which also demonstrated the same feature, again affording a completely liquid mixture of products after dehydrogenation (Figure 21). Additionally, automated gas burette measurements revealed H_2 release from the blend proceeded at a faster initial rate than from either of the two separate components (Figure 22). The dehydrogenation of the blend could be further accelerated through the use of catalytic amounts of carbon-supported (Pt)-Ni (core)-shell nanoparticles (~1 wt. % metal) to achieve 5.8 wt. % H_2 release in 150 min, close to the theoretical maximum of 6.0 wt. % (Figure 23).

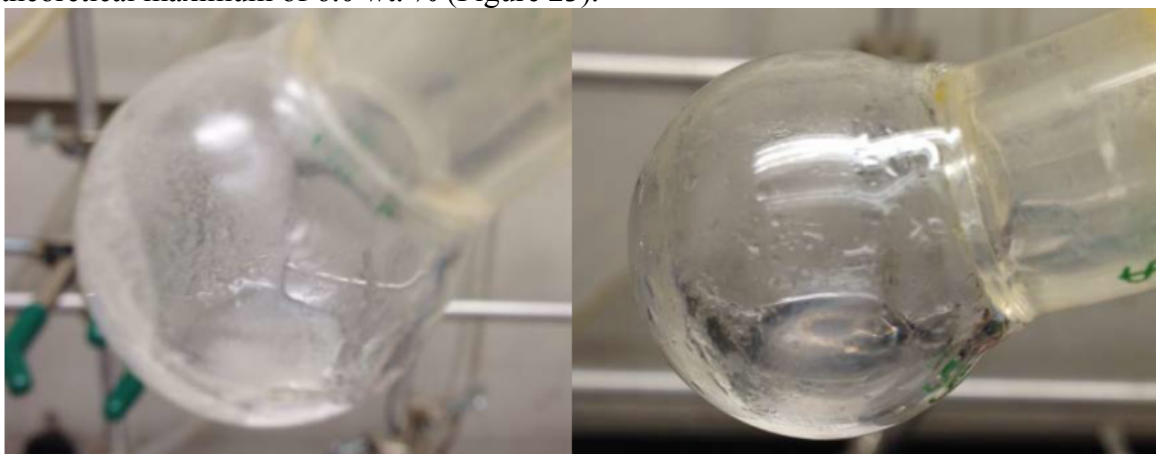

Figure 21. Photographs of a slurry of AB in **B** (2:1 **B**:AB molar ratio) before (left) and after (right) complete H_2 release at 110 ºC.

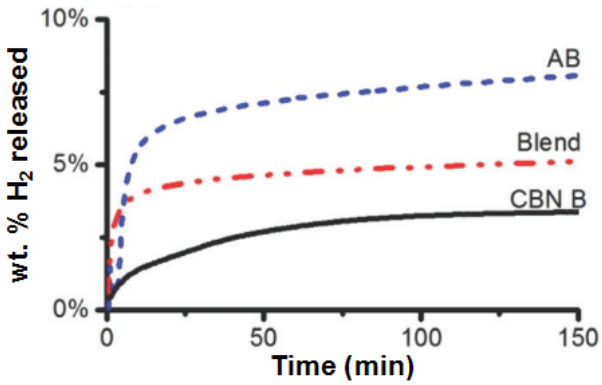

Figure 22. Automated gas burette measurements of thermal H_2 release from neat **B** (black), AB (blue), and a 2:1 molar ratio **B**:AB blend (red) at 110 ºC.

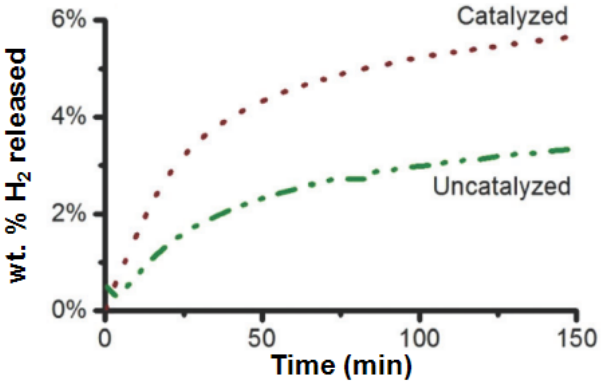

Figure 23. Automated gas burette measurements of H_2 release from a 2:1 molar ratio **B**:AB blend in the presence (maroon) and absence (green) of (Pt)-Ni (core)-shell nanoparticles on carbon support at 80 ºC.

The observed increased rate of decomposition of the blend versus its separate components suggested that AB and **B** were reacting together, possibly to form mixed trimers **8** and **9** in addition to **6** and borazine (Scheme 5). Indeed, all four species were observed by mass spectrometry-coupled gas chromatography (GC-MS) in the product mixture of the dehydrogenation reaction. Furthermore, the product distribution proved strongly dependent on the molar ratio of AB to **B** in the starting blend: higher ratios of **B** relative to AB resulted in decreased borazine formation and correspondingly increased amounts of **9** and **6** beyond the levels expected for simple dilution effects (Table 3). This presumably occurs as more dehydrogenated intermediates of **B** are present to trap dehydrogenated intermediates of AB as either **8** or **9**. This trend was also observed by RGA of the H_2 stream produced from blends of various **B**:AB ratios (Table 4), with only 0.01% borazine content detected when the (Pt)-Ni/C catalyst was used with a 2:1 molar ratio **B**:AB blend at 80 ºC. This marks a significant improvement over the performance of neat AB, whose decomposition produced a gas stream consisting of over 7% borazine.

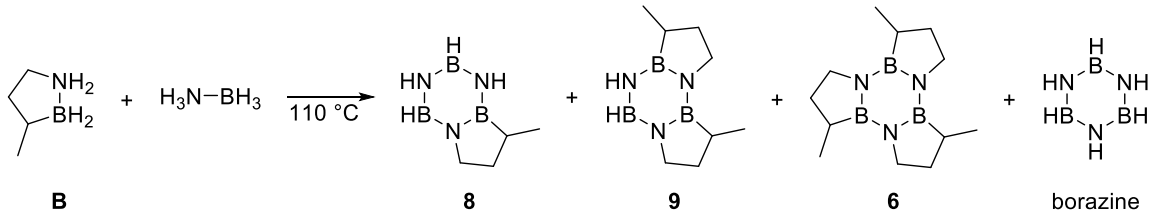

Scheme 5. Generation of various products from thermal dehydrogenation of AB:**B** blend at 110 ºC.

Table 3. Product distribution from decomposition of **B**:AB blends of various compositions based on analysis with GC-MS.

	% composition			
B:AB (molar ratio)	**8**	**9**	**6**	borazine
1:1	12	73	7.3	7.3
2:1	2.5	56	38	3.0
3:1	1.5	45	53	0.9
4:1	nd	18	81	0.9

Table 4. RGA of borazine content in the gas stream produced from decomposition of **B**:AB blends of various compositions.

B:AB (molar ratio)	% borazine content
0:1	7.32
1:1	1.26
2:1	0.48
3:1	0.35
4:1	0.16
2:1[a]	0.01

[a] Using (Pt)-Ni/C catalyst at 80 ºC.

As demonstrated above in Scheme 4 for pure **6**, the mixture of trimers from the dehydrogenated 2:1 **B**:AB blend can be digested with methanol to selectively produce borate **7** and ammonia trimethylborate; based on our previous work (*vide supra*), it should be feasible to collectively reduce these species with a suitable hydride reagent to regenerate the original fuel blend.

2.3. Compound C

4-Methyl-1,2-BN-cyclopentane (**C**) was synthesized as shown in Scheme 6 starting from addition of $NaN(TMS)_2$ to 3-bromo-2-methylpropene.[45] The same hydroboration, hydride/proton addition sequence as for **A** then furnished **C** as a white solid (mp = 50 °C).

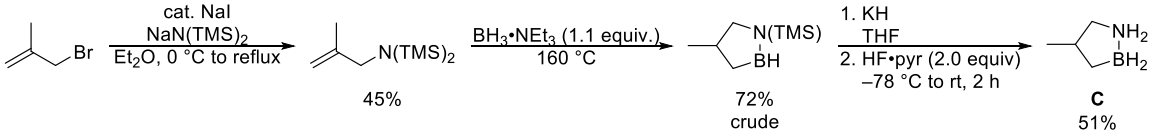

Scheme 6. Synthesis of 4-methyl-1,2-BN-cyclopentane (**C**) from 3-bromo-2-methylpropene. (Note: HF•pyridine is both corrosive and toxic; calcium gluconate should be kept on hand during any manipulation.)

As the other members of the BN-cyclopentane series (**A**, **B**, and **D**), **C** cleanly releases two H_2 equivalents to form trimer **10** upon thermal decomposition (150 ºC) or in the presence of catalytic $CoCl_2$ at 80 ºC (Scheme 7, top). Under slightly milder conditions, however, dehydrogenation of **C** was found to proceed to the isolable dimer **11**, whose structure was confirmed by X-ray crystallography (Scheme 7, bottom). A further two equivalents of H_2 were rapidly released from this dimeric species at 80 ºC to ultimately form trimer **10**. Thus, **11** was identified as a kinetically competent intermediate in the overall decomposition of **C** to **10**.

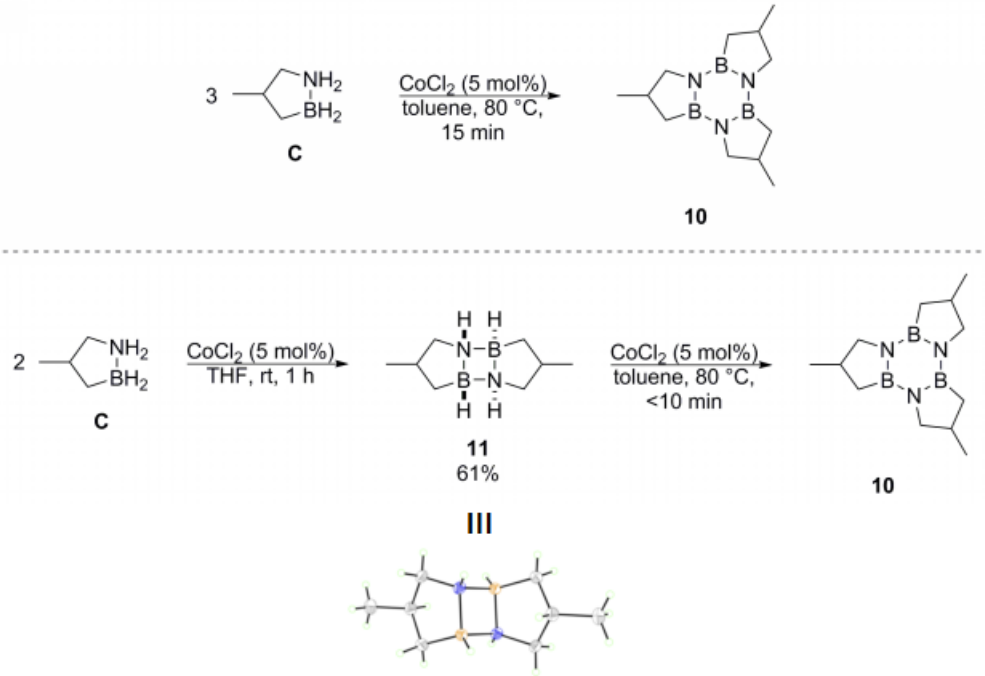

Scheme 7. Catalytic decomposition of **C** directly to trimer **10** (top), or sequentially through isolable dimer **11** (bottom).

Automated gas burette measurements revealed the release of two H_2 equivalents from **11** to occur at approximately the same rate with or without the addition of catalyst (Figure 24). In the absence of catalyst, however, **C** itself does not decompose at 80 ºC. Taken together, these results indicate the cobalt's primary catalytic function lies in the acceleration of the formation of **11** from **C**.

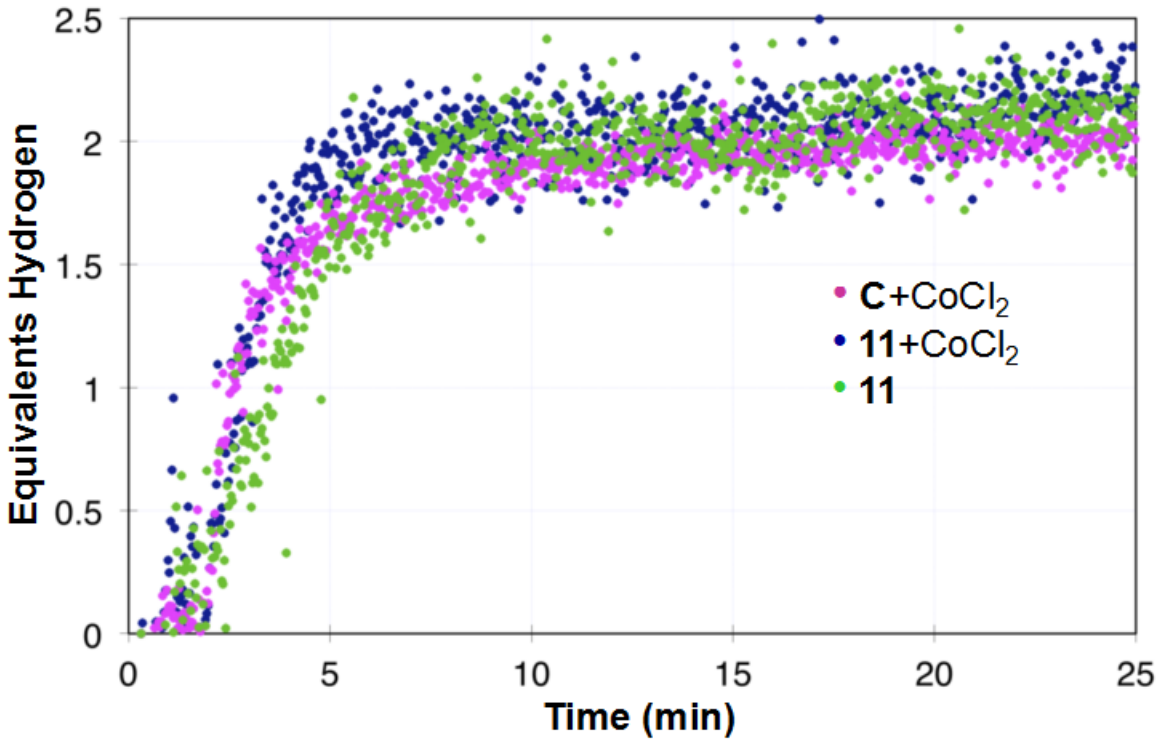

Figure 24. Automated gas burette measurements of $CoCl_2$-catalyzed H_2 release from **C** (purple) and **11** (blue) and uncatalyzed release from **11** (green). Conditions: toluene, 80 ºC.

The effect of the concentration of **11** on the rate of dehydrogenation was also investigated. Specifically, doubling the concentration of **11** resulted in a corresponding two-fold increase in the H_2 evolution rate (Figure 25). This relationship suggests decomposition of **11** to **10** proceeds according to a first-order concentration dependence with respect to **11**.

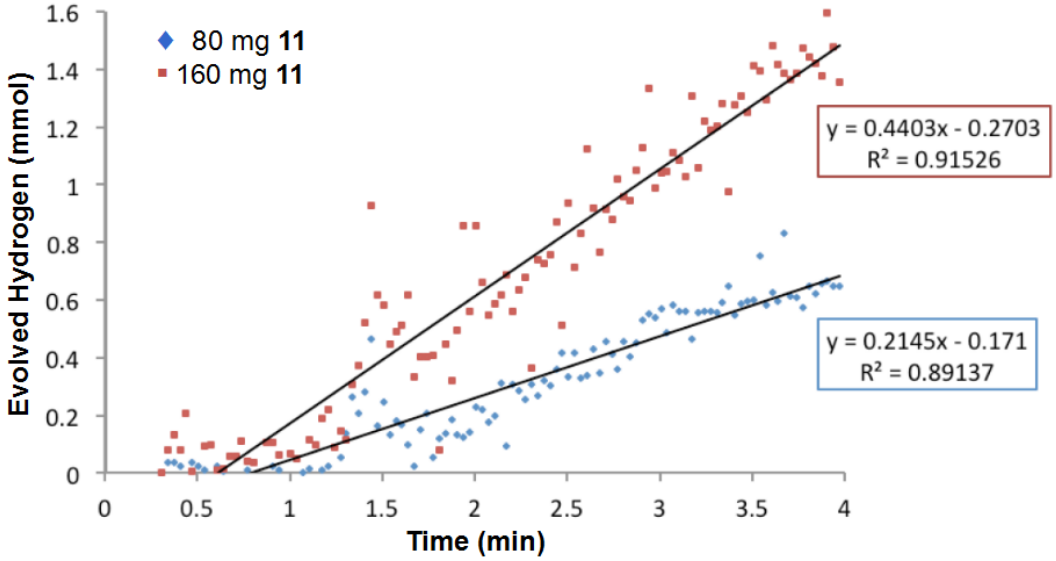

Figure 25. Comparison of H_2 evolution rates from **11** at two different concentrations.

2.4. Compound D

5-Methyl-1,2-BN-cyclopentane (**D**) was synthesized[36] as shown in Scheme 8 starting from addition of potassium phthalimide to 3-chloro-1-butene.[46] The allyl phthalimide intermediate **12** was treated first with ethanolamine and then gaseous HCl to afford 3-amino-1-butene hydrochloride. Amine protection with 1,2-bis(chlorodimethylsilyl)ethane (**13**), followed by the same hydroboration, hydride/proton addition sequence as for **A** furnished gram quantities of **D** as a low-melting solid (mp = 25−27 °C).

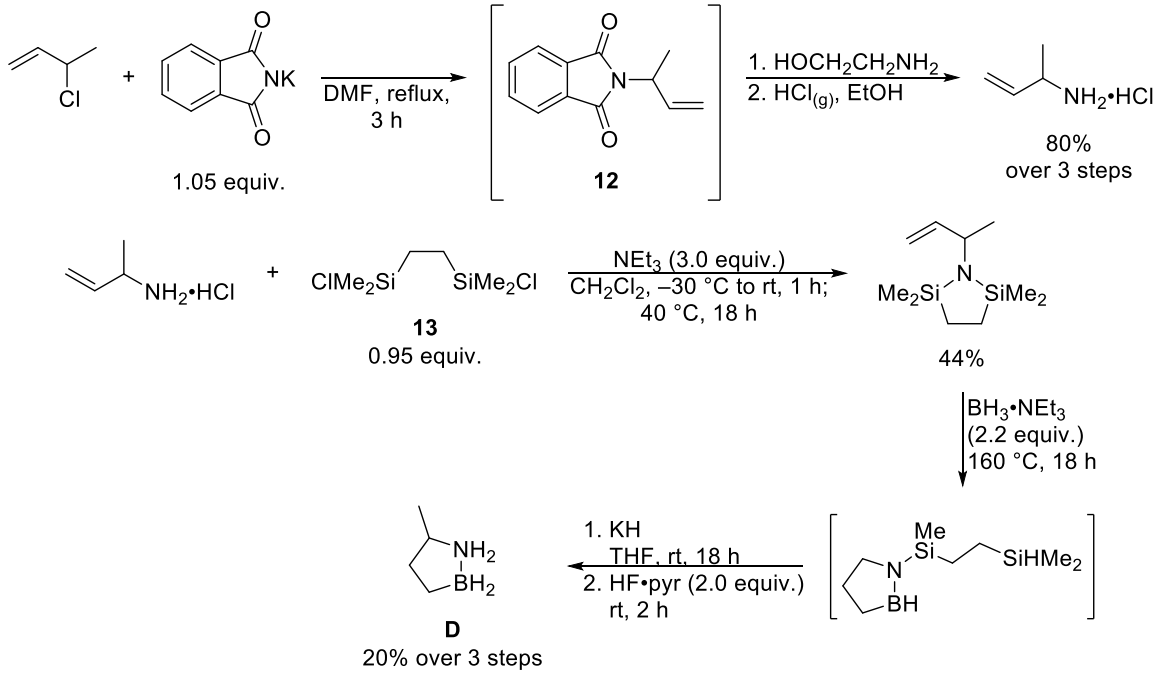

Scheme 8. Synthesis of **D** starting from 3-chloro-1-butene. (Note: HF•pyridine is both corrosive and toxic; calcium gluconate should be kept on hand during any manipulation.)

Using an automated gas burette to monitor the $CoCl_2$-catalyzed release of H_2 from **D** revealed the reaction to be significantly slower than that of the other members of the BN-cyclopentane series (**A**−**C**); in the presence of 5 mol% catalyst in diglyme at 80 °C, **D** released two H_2 equivalents only after 100 min (Figure 26).

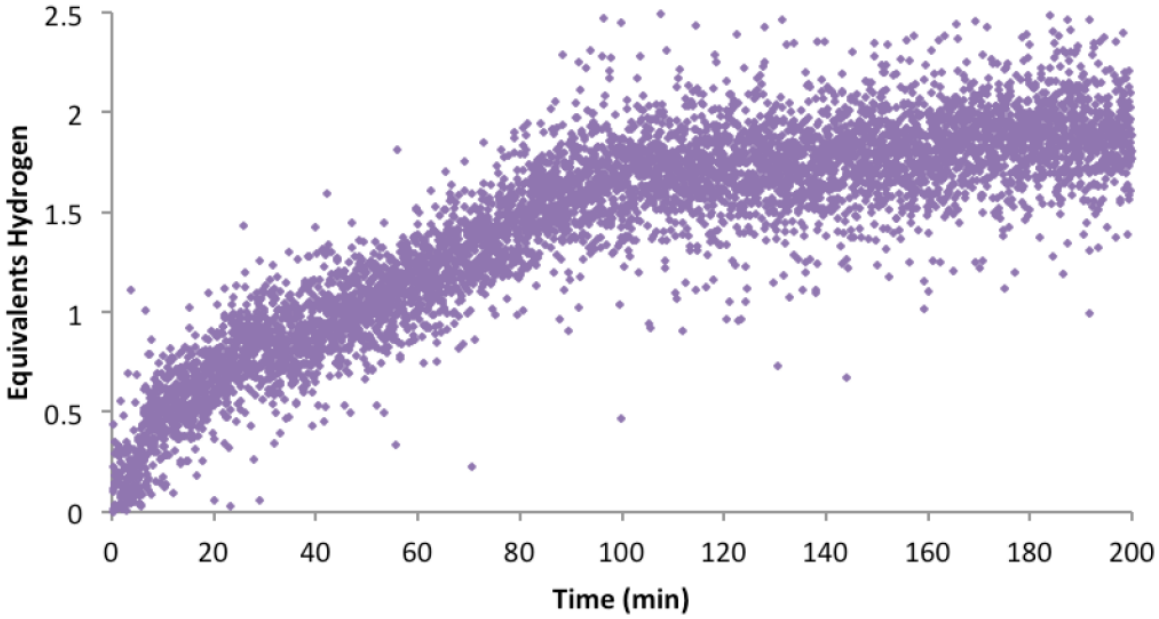

Figure 26. Automated gas burette measurements of catalyzed H_2 release from **D**. Conditions: $CoCl_2$ (5 mol%), 0.59 M diglyme, 80 °C.

2.5. Compound E

1,3-BN-cyclohexane (**E**) was conceived as a possibly reversible hydrogen storage material with potential to activate H_2 across the BN unit in an FLP-type manner. The loss of three H_2 equivalents from **E** was calculated (G3MP2) as approximately thermoneutral (ΔG_{298K} = −5.3 kcal-mol^{-1}; Scheme 9), suggesting facile reversibility of dehydrogenation. As shown in Table 5, computations also predicted elimination of the first H_2 equivalent from across the BN unit to be only slightly endothermic (ΔH_{298K} = +0.8 kcal-mol^{-1}) and exergonic overall (ΔG_{298K} = −8.5 kcal-mol^{-1}), which likewise supported the proposed idea of FLP-like behavior. Only initial H_2 desorption from the N−C(2) bond was calculated to have similar thermodynamics; all other starting dehydrogenation reactions were predicted to be both significantly endothermic and endergonic.

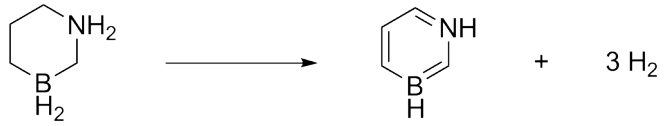

E

ΔH_{298K} = −20.5 kcal-mol^{-1}
ΔG_{298K} = −5.3 kcal-mol^{-1}

Scheme 9. Calculated (G3MP2) overall thermodynamics for complete dehydrogenation of **E**.

Table 5. Calculated (G3MP2) thermodynamics for initial loss of H_2 from **E**.

Reaction	ΔH_{298K} (kcal mol^{-1})	ΔG_{298K} (kcal mol^{-1})	$\Delta G_{298K,THF}$ (kcal mol^{-1})
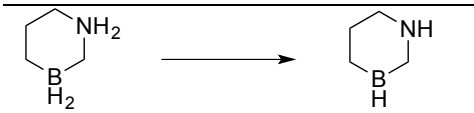 **E**	+0.8	–8.5	–0.6
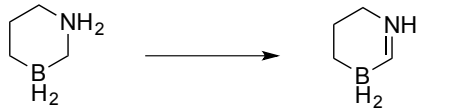 **E**	+7.1	–2.1	–0.2
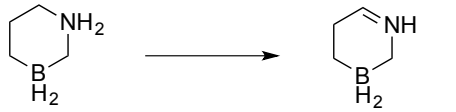 **E**	+19.9	+10.8	+6.8
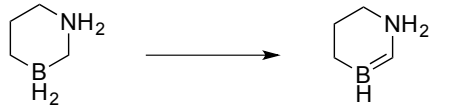 **E**	+22.5	+13.6	+10.5
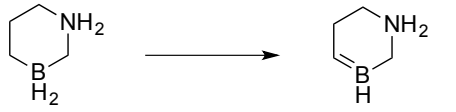 **E**	+29.9	+21.1	+14.4

It was perceived, however, that **E** could spontaneously dimerize after BN dehydrogenation, which could interfere with further reactivity and regeneration. Thus, preparation of *N*-mono- and *B,N*-disubstituted versions of **E** was attempted with the intent that sufficient steric encumbrance would prevent this dimerization. Hydrogenation of the known 1,3-azaborines **14**[47] and **15**[48] was proposed to afford facile access to such substituted derivatives. As shown in Scheme 10, however, both the hydrogenated products **16** and **17** were observed to undergo subsequent dimerization to **18** and **19**, respectively. A variant with an even bulkier *B*-(2,4,6-triisopropylphenyl) group proved synthetically inaccessible.

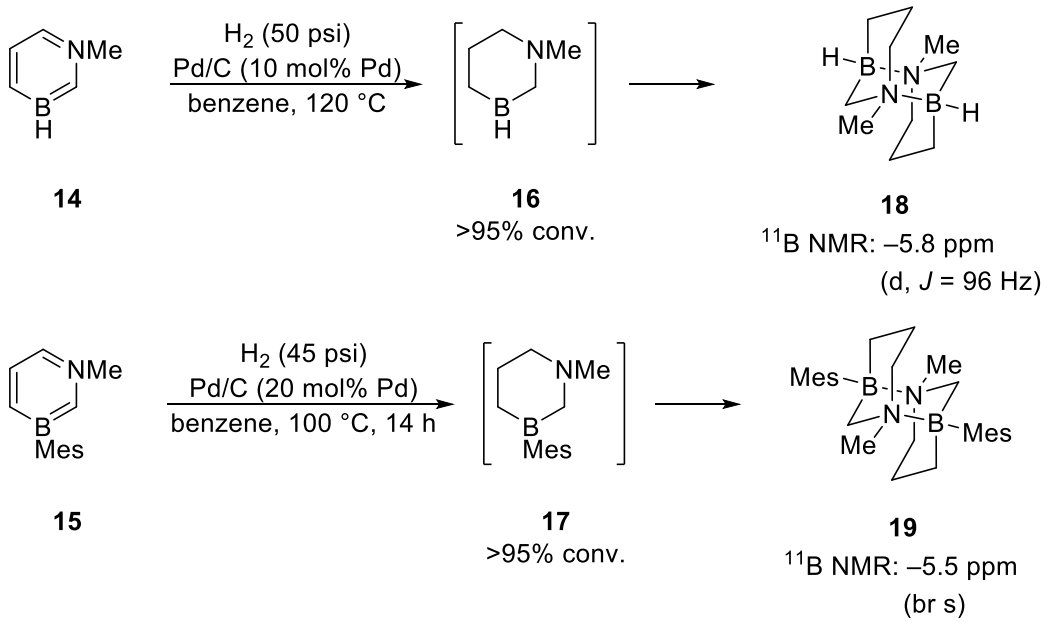

Scheme 10. Attempted synthesis of substituted **E** derivatives **16** and **17** via hydrogenation of 1,3-azaborines **14** and **15**, respectively.

2.6. Compound F

N-Methyl-1,2-BN-cyclohexane (**F**) was synthesized as shown in Scheme 11 starting with addition of $MeNH_2$ to 4-bromo-1-butene to form homoallylamine **20**.[49] Treatment of **F-1** with BH_3•THF at ambient temperature initially generated amine-borane adduct **21**; this adduct underwent intramolecular hydroboration at elevated temperatures to produce a separable mixture of **F** and the BN-dehydrogenated species **22**. Fortuitously, recovered **22** could be converted to **F** through a facile hydride/proton addition sequence using KH and HCl.

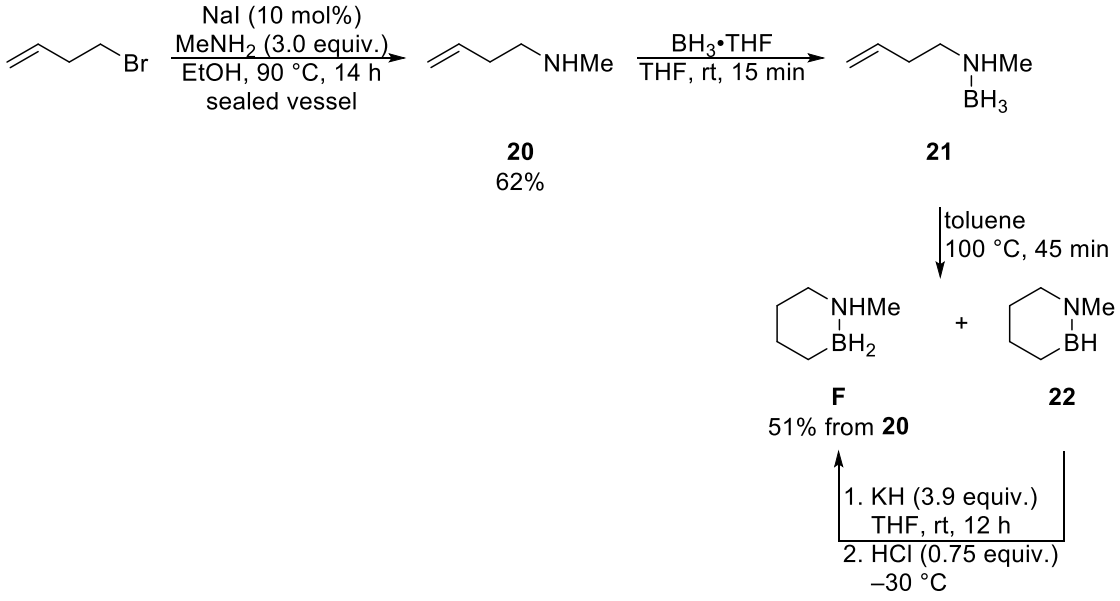

Scheme 11. Synthesis of **F** from 4-bromo-1-butene.

Although **F** is a solid under ambient conditions, it melts at 72−73 °C, a range notably below the standard operating temperature of many fuel cells (~80 °C). It was therefore considered potentially feasible to employ neat **F** as a liquid hydrogen storage material under such conditions. Indeed, based on a measured liquid density of 0.87±0.08 kg-L^{-1}, the theoretical volumetric H_2 capacity (assuming release of 3 equiv. of H_2) of neat **F** was calculated as 53 g H_2-L^{-1} (Table 6). Similar evaluations were also performed for saturated THF and Et_2O solutions of **F**. Of the two solvents, THF was found the more effective at dissolving **F** (292±5 g **F**-L^{-1}). Based on this degree of solubility, a saturated THF solution of **F** was thus predicted to afford a volumetric H_2 capacity of 18 g H_2-L^{-1}.

Table 6. Properties of **F** as a neat liquid and in organic solvents.

composition	density (kg L^{-1})	solubility (g L^{-1})	volumetric capacity[a] (g H_2 L^{-1})
neat	0.87±0.08	n/a	53
sat. THF solution	0.8992	292±5	17.8
sat. Et_2O solution	0.7134	106±18	6.5

[a] Assuming loss of three H_2 equivalents.

The BN-dehydrogenation of **F** was found to be catalyzed under homogeneous conditions using $RuCl_2(PPh_3)_3$ (Scheme 12). Using this system, the enthalpy of the initial loss of H_2 from **F** could be measured using reaction calorimetry. A ΔH value of −3.4±0.8 kcal-mol^{-1} was measured experimentally; a computationally determined (G3MP2) value of −4.9 kcal-mol^{-1} accorded well with this value.

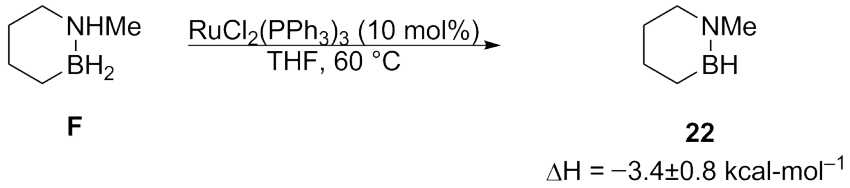

Scheme 12. Catalytic dehydrogenation of **F** using $RuCl_2(PPh_3)_3$.

It appears that intermediate **22** represents a thermodynamic sink on the reaction pathway toward complete H_2 desorption. The existence of such a sink would ultimately prevent reversible H_2 uptake. Thus compound **F** was not further pursued as a reversible material.

2.7. Compounds G and G'

N-substituted bis-BN-cyclohexane compounds **G** and **G'** were synthesized by addition of either $MeNH_2$ or $^tBuNH_2$ to potassium (bromomethyl)trifluoroborate (**23**) to form zwitterions **24** and **25**, respectively (Scheme 13). Deprotonation with NEt_3 and subsequent fluoride abstraction by TMSCl facilitated formation of dimers **26** and **27**, which were reduced with $LiAlH_4$ to the desired final compounds.

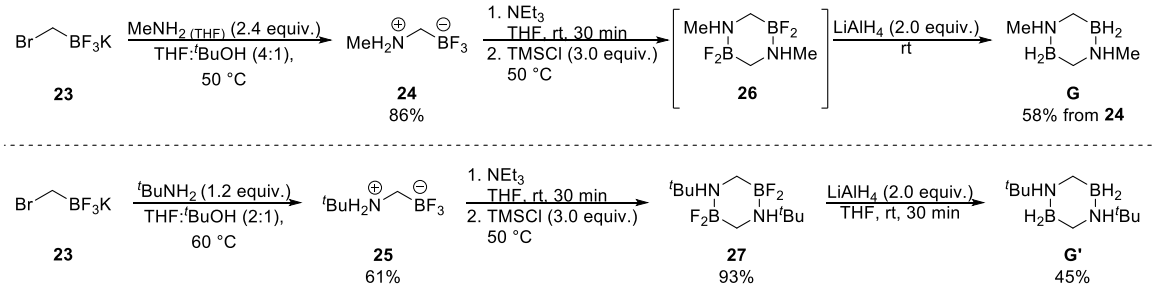

Scheme 13. Synthesis of **G** (top) and **G'** (bottom) from potassium (bromomethyl)trifluoroborate (**23**).

Automated gas burette measurements revealed **G** and **G'** to rapidly release two H_2 equivalents in the presence of catalytic Pd/C in diglyme at 120 °C (Figure 27). Of the two materials, **G** demonstrated the more rapid dehydrogenation activity, presumably as a result of the lesser steric hindrance of its methyl substituents compared to that of the *tert*-butyl groups on **G'**.

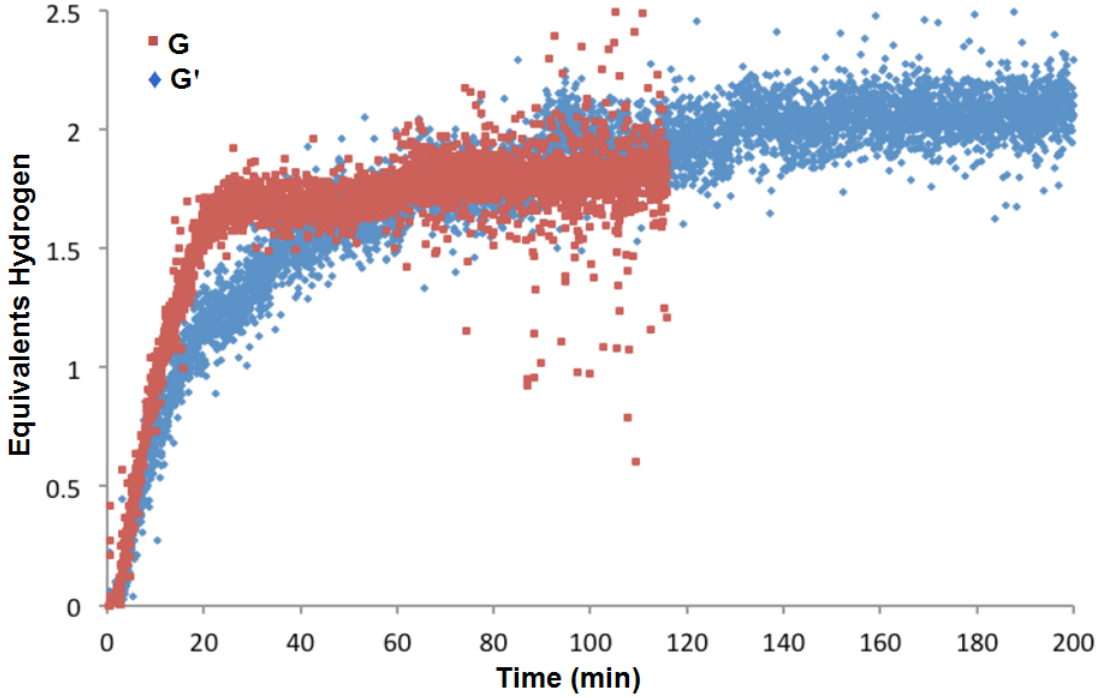

Figure 27. Automated burette traces for Pd/C-catalyzed H_2 release from **G** (red) and **G'** (blue). Conditions: 0.17 M in diglyme, 120 °C.

Similar to compound **F** intermediates associated with H_2 desorption from the B-N portion of **G** and **G'** represent thermodynamic sinks on the reaction pathway toward complete H_2 desorption. Thus compounds **G** and **G'** were not further pursued as reversible materials.

2.8. Compound H

1,2,4,5-bis-BN-Cyclohexane (**H**) was synthesized[50] as shown in Scheme 14 starting

from a one-pot procedure involving addition of bromomethyllithium (generated *in situ*[51]) to triisopropyl borate, hydrolysis with $MeSO_3H$, and esterification with pinacol to give boronic ester **28**. Bromide displacement with $NaN(TMS)_2$,[52] followed by reduction with $LiAlH_4$ then produced lithium borohydride **29**. Dimerization of **29** to form *N,N'*-bis-silylated bis-BN-cyclohexane **30** was achieved with ethereal HCl at −78 °C; facile silyl deprotection with TBAF then afforded **H** as a white solid.

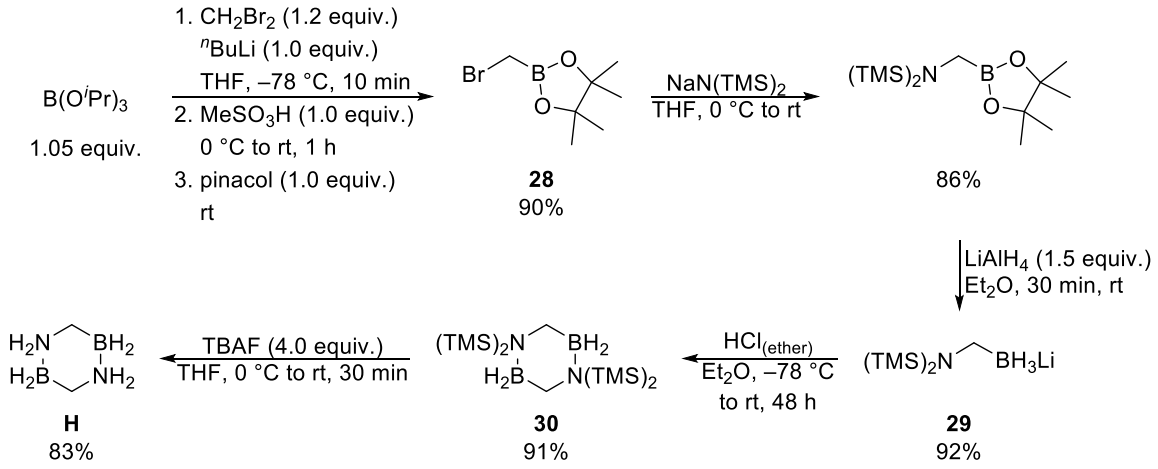

Scheme 14. Synthesis of **H** starting from triisopropylborate.

The thermal stability of **H** proved remarkably high, both neat and in solution. As observed by differential scanning calorimetry-coupled thermogravimetric analysis (TGA-DSC) experiments (Figure 28), a neat sample sublimed between 150–200 ºC with no loss of H_2 evident by ^1H and ^{11}B NMR.[50] Likewise no dehydrogenation occurred in a toluene solution at 150 °C within 24 h.

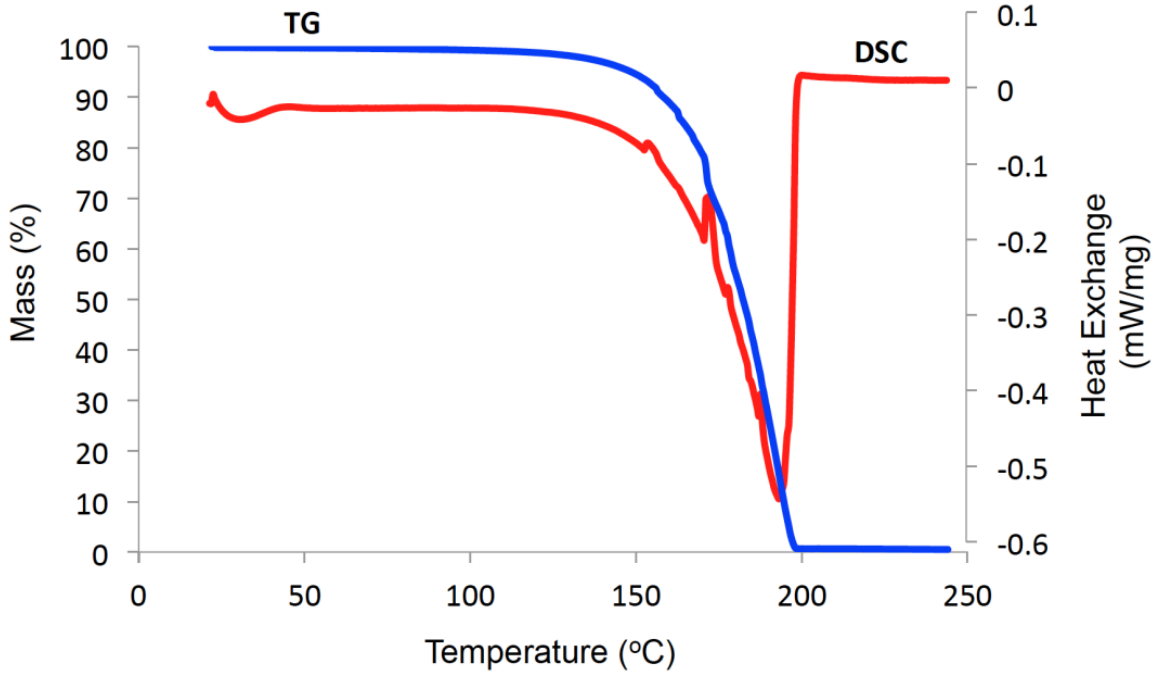

Figure 28. TGA-DSC measurements of **H** at a heating rate of 1 ºC-min^{-1}.

Fortuitously, however, H_2 release could be achieved under catalytic conditions: either Pd/C at 120 °C, or activated ruthenium precatalyst **31**[53] at 85 °C (Scheme 15). (Dehydrogenation with **31** also occurred at room temperature if the catalyst loading was increased to 5 mol%). Interestingly, while both catalytic systems produced some polymeric materials, the major product of Pd/C-catalyzed dehydrogenation was determined to be the six-four cage compound **32**; a different, six-five cage compound, **33**, was similarly produced using activated **31**. The gas-phase thermodynamics for the dimerization of **H** to form either cage-compound **32** or **33** were calculated (G3MP2) at 298 K (Table 7). The formation of both cage products was predicted to be significantly exergonic, with **33** more thermodynamically stable than **32** by approximately 8 kcal-mol^{-1}.

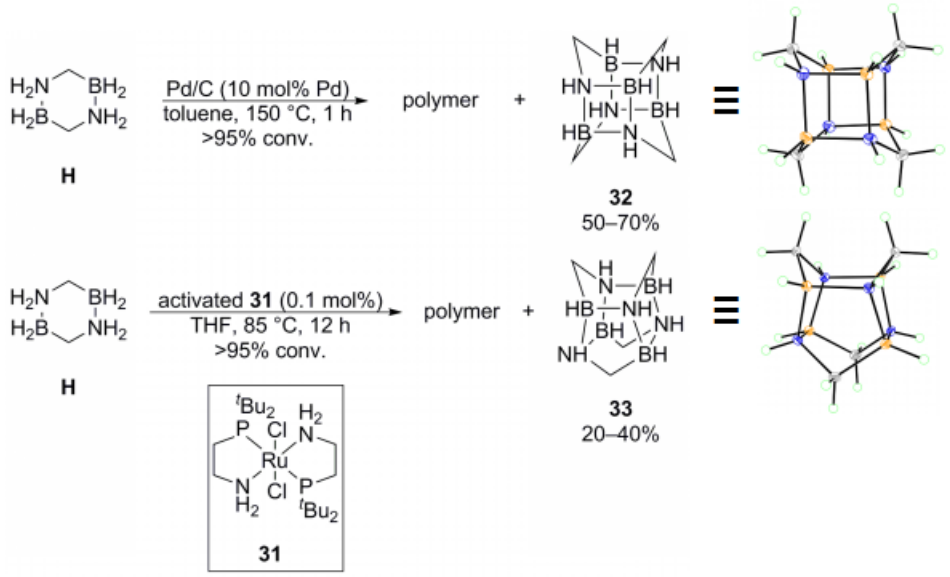

Scheme 15. Catalytic dehydrogenation of **H** using Pd/C (top) or ruthenium catalyst **31**.

Table 7. Calculated (G3MP2) gas-phase thermodynamics for formation of **32** and **33** from **H** at 298 K.

Reaction	ΔH_{298K} (kcal mol^{-1})	ΔG_{298K} (kcal mol^{-1})
2 **H** → **32**	–38.8	–56.0
2 **H** → **33**	–48.2	–64.3

The purity of the gas stream produced using **31** at 65 ºC was evaluated using RGA; gratifyingly, no volatile species other than H_2 were detected (Figure 29). Automated gas burette measurements revealed, however, only two H_2 equivalents were released under such conditions (Figure 30).

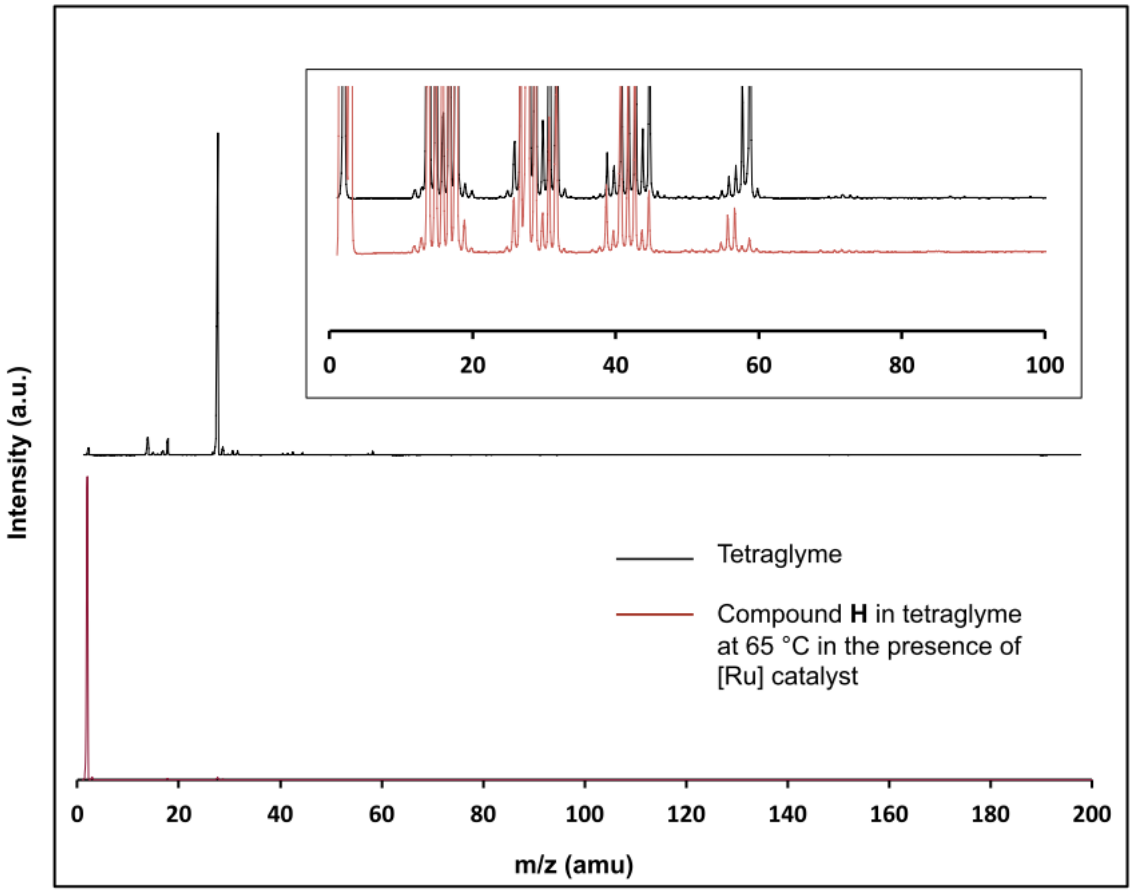

Figure 29. RGA spectrum of the gas stream produced by dehydrogenation of **H** at 65 ºC using ruthenium catalyst **31**.

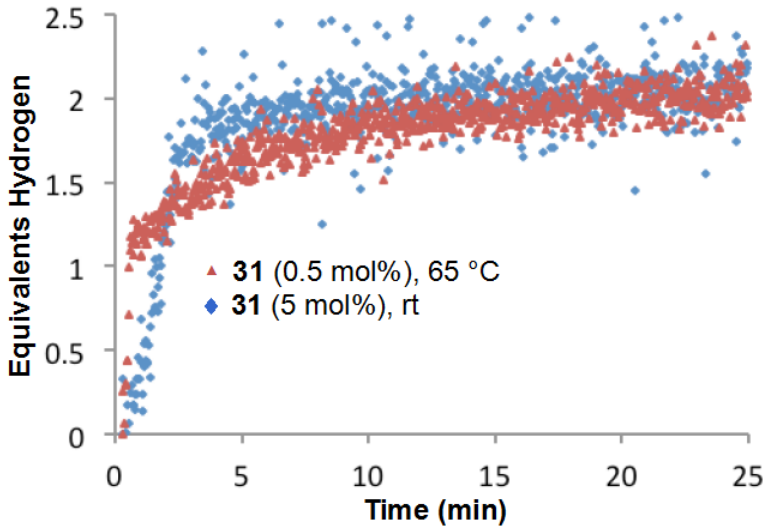

Figure 30. Automated gas burette traces of catalyzed H_2 release from **H** using ruthenium catalyst **31**.

It was hypothesized that the formation of polymers and cage compounds might be avoided and full dehydrogenation thereby facilitated if the catalysis occurred in a confined space such as the internal cavities of a metal-organic framework (MOF). To this end, two Pd nanoparticle-bearing metal-organic frameworks (MOFs), ZIF-8[54] and UiO-66-NH_2[55], were investigated as dehydrogenation catalysts for **H**. While the use of Pd@ZIF-8 yielded the same product profile (based on ^{11}B NMR) as previously observed with Pd/C, after reaction with Pd@UiO-66-NH_2, no ^{11}B NMR signal of any kind could be detected from the crude reaction mixture. Based on this result, it seemed possible that an insoluble, extensively dehydrogenated material had formed under the reaction conditions. To determine whether or not additional H_2 equivalents were indeed being released, the amount of H_2 produced was quantified using an automated gas burette. As shown in Figure 31, however, only two H_2 equivalents were evolved using Pd@UiO-66-NH_2, even after a prolonged reaction time (>8 h). Similar results were also observed for controls using Pd adsorbed to the outer surface of the MOF and Pd/C. To reconcile these results with the disappearance of soluble boron-containing species, it is possible the free NH_2 group of the MOF backbone binds an initially dehydrogenated intermediate and thus sequesters it from solution.

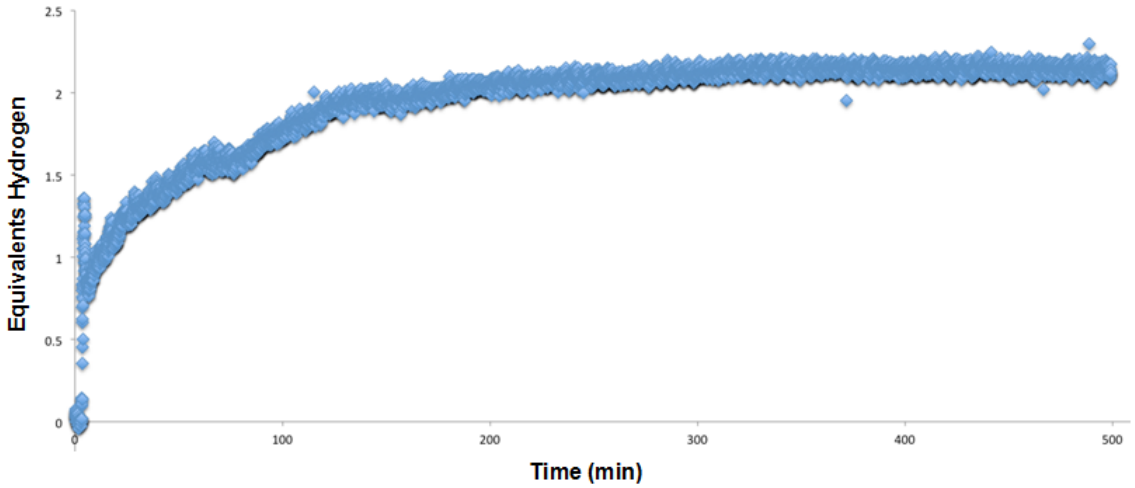

Figure 31. Automated gas burette trace of catalyzed dehydrogenation of **H** using Pd@UiO-66-NH_2. Conditions: Pd@UiO-66-NH_2 (10 mol% Pd), 1,2-dichlorobenzene, 160 ºC.

2.9. Compound J[56]

1,2-BN-Cyclohexane (**J**) was synthesized as shown in Scheme 16 starting from addition of $NaN(TMS)_2$ to chloromethyl methyl ether.[57] Subsequent addition of allylmagnesium bromide then formed homoallylamine **34**, which underwent a similar hydroboration, hydride/proton addition sequence as for **A** to furnish **J** as a white solid (mp = 75 ºC).[58]

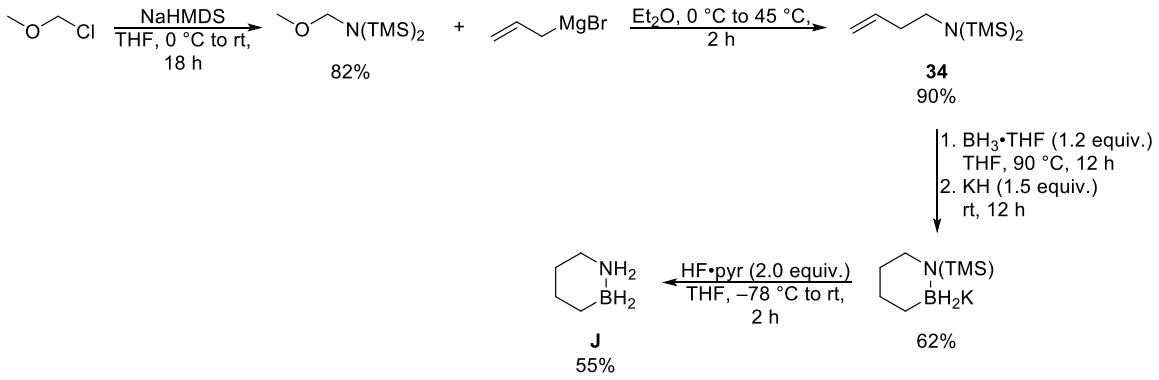

Scheme 16. Synthesis of **J** starting from chloromethyl methyl ether. (Note: Chloromethyl methyl ether is a known volatile carcinogen; use only in a well-ventilated fume hood. HF•pyridine is both corrosive and toxic; calcium gluconate should be kept on hand during any manipulation.)

As with the BN-cyclopentane series (**A–D**), **J** undergoes thermal decomposition to selectively form trimer **35** (Scheme 17). Significant H_2 release from neat **J** was determined by TGA to initiate at 70 ºC (Figure 32). (This result accorded well with a previous evaluation of thermal stability in which a sample of **J** heated at 60 ºC for six days showed no signs of decomposition by ^{11}B NMR.) At slow heating rates (0.05 ºC-min^{-1}), almost complete mass loss was observed by TGA at approximately 100 ºC (Figure 33). Interestingly, however, a neat sample of trimer **35** (as well as **6** (trimer of compound **B**)) experienced no appreciable mass loss at this temperature (Figure 34). This suggested that intermediates resulting from only partial dehydrogenation of **J** might themselves be significantly volatile under such thermal decomposition conditions.

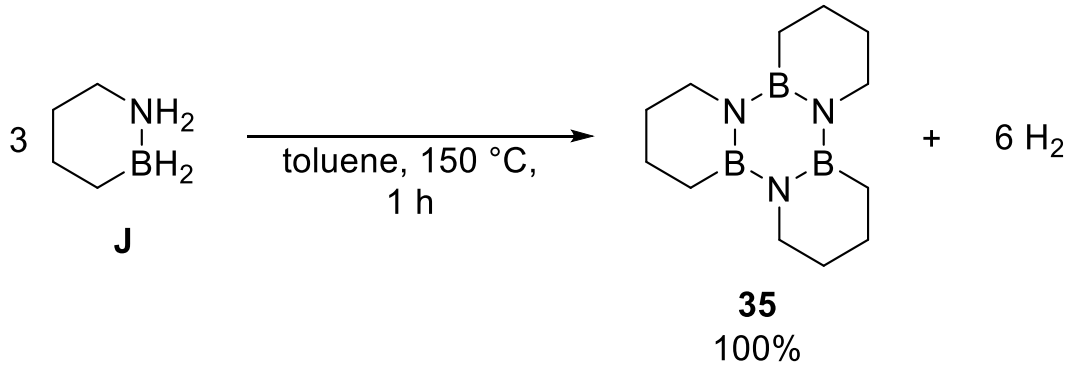

Scheme 17. Thermal decomposition of **J** to form trimer **35**.

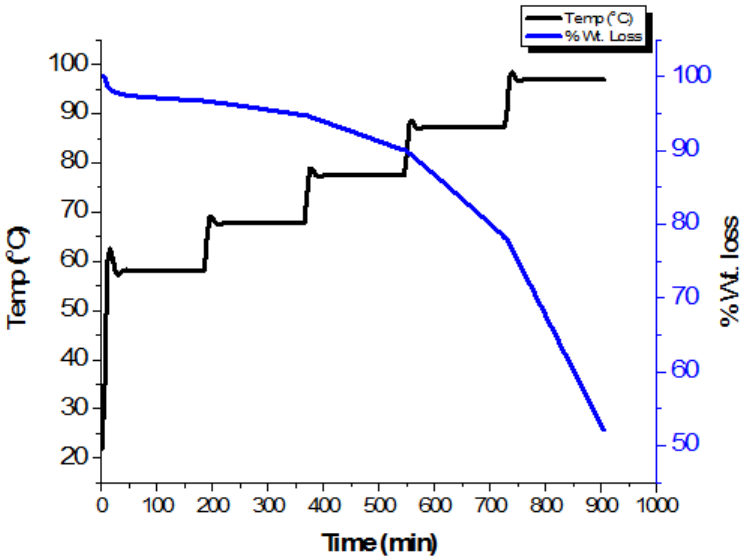

Figure 32. TGA of **J** from 60–100 ºC with ramping at 10 ºC-min^{-1} between isothermal periods (3 h).

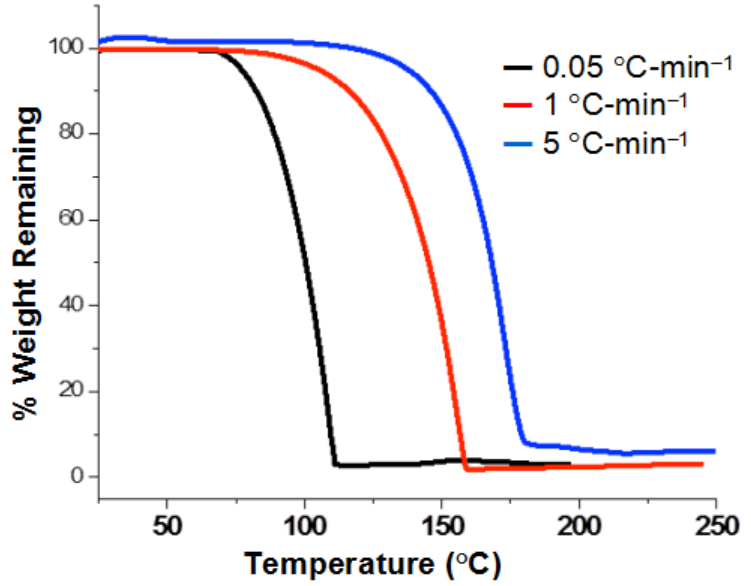

Figure 33. TGA of **J** at various continuous heating rates.

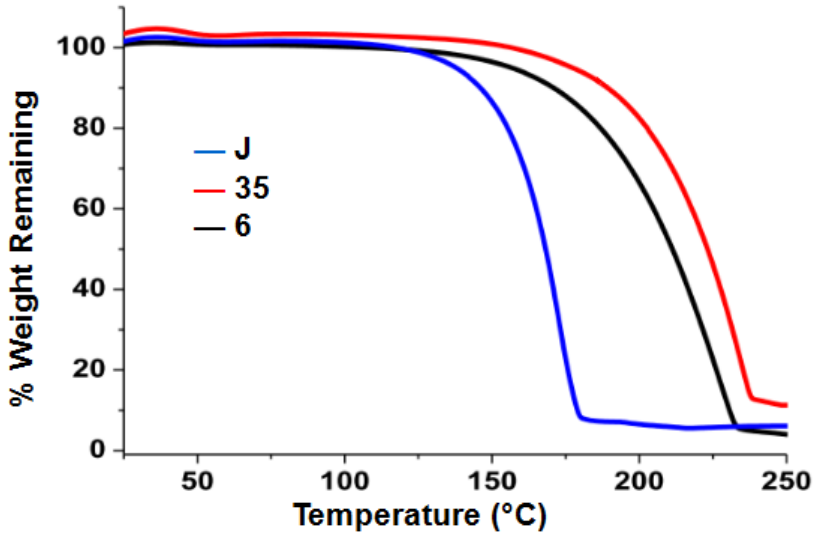

Figure 34. Comparison of TGA for samples of **J**, **35**, and **6** continuously heated at 5 ºC-min^{-1}.

While 1,2-BN-cyclohexene (**36**) had been purportedly observed by *in situ* ^{11}B NMR as the product of initial H_2 loss from **J**, it could not be isolated for characterization under dehydrogenation conditions owing to its propensity to undergo facile decomposition to **35**. Thus, in collaboration with Prof. Stephen Kukolich at the University of Arizona, the generation of **36** from **J** was attempted under conditions amenable to microwave spectroscopy.[59] This entailed heating a neat sample of **J** in a neon gas stream to generate measurable levels of gas-phase **36** (Scheme 18). Significantly, the experimentally determined rotational constants and quadrupole coupling parameters for the observed species agreed with those predicted by computation for **36** and moreover, differed significantly from those calculated for **J** itself. The experimental ^{11}B isotopologue inertial defect (Δ_0) was measured as −20.78 amu Å^2, indicating a non-planar structure and strikingly unlike that previously observed for the planar, aromatic species 1,2-dihydro-1,2-BN-azaborine (Δ_0 = +0.02 amu Å^2).[60]

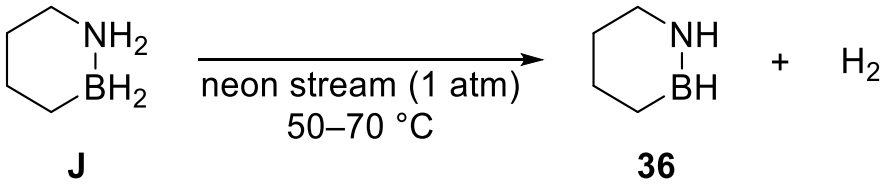

Scheme 18. Conditions for generation of **36** from **J** for microwave spectroscopy.

The kinetics of the Pd/C-catalyzed loss of two H_2 equivalents from neat **J** were measured at various temperatures using an automated gas burette (Figure 35). As for **B**, the rates of H_2 evolution were treated as those of a pair of first-order reactions occurring in series and were fitted to an appropriate model to obtain the activation parameters for each dehydrogenation reaction. The activation energies derived from this model for release of the first and second H_2 equivalents from **J** were +19.0 kcal-mol^{-1} and +39.7 kcal-mol^{-1}, respectively; the pre-exponential factors were likewise estimated as 8.04 x 10^8 s^{-1} and 3.53 x 10^{19} s^{-1}, respectively. These values were used in subsequent COMSOL

modeling as the kinetic parameters for exothermic BN H_2 release in a theoretical thermodynamically-coupled exothermic-endothermic dehydrogenation reaction (see Section 3.3).

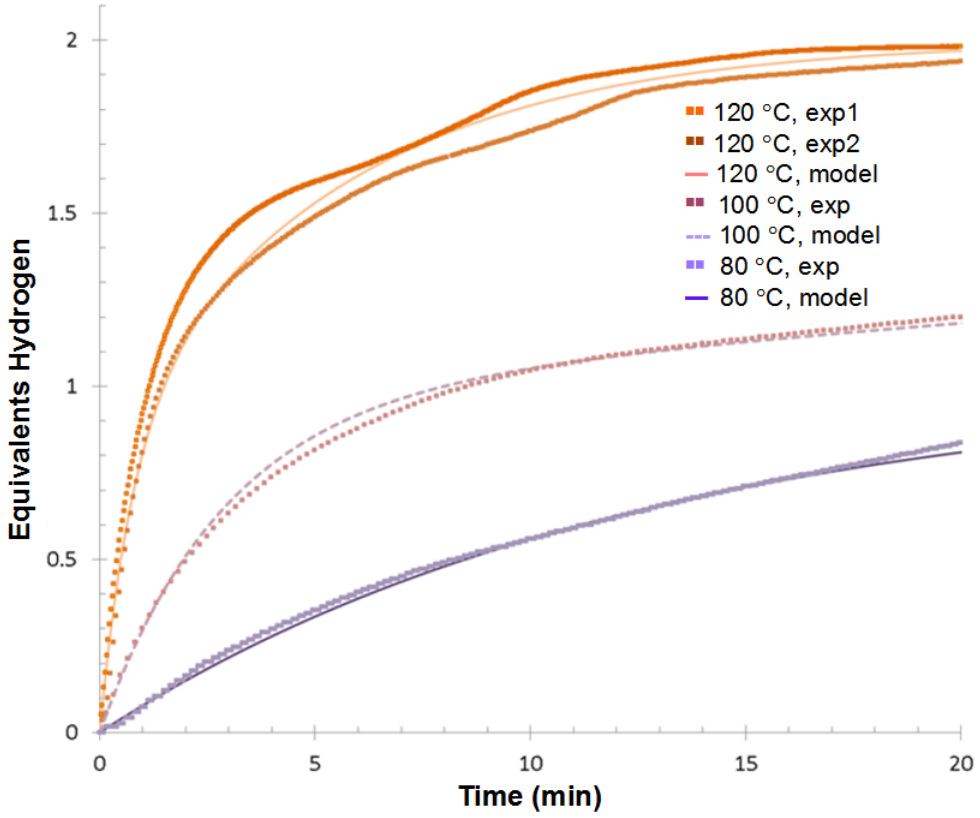

Figure 35. Automated gas burette traces of catalyzed dehydrogenation of **J** at various temperatures, overlaid with kinetic model-predicted traces. Conditions: Pd/C (4 mol% Pd), neat.

The solution phase kinetics of the initial loss of H_2 from **J** were also studied using ReactIR in the same manner as for **B** (see Section 2.2). As for **B**, a second order concentration dependence was observed when the initial concentration of **J** ($[\mathbf{J}]_0$) was varied from 0.560 M to 1.283 M at 140 °C (Figure 36). Subsequent Arrhenius analysis (Figure 37), however, revealed a more complex set of trends *vis-à-vis* **B**. As shown in Table 8, while the activation energy (E_a) for initial loss of H_2 from **J** was found to be 5 kcal-mol^{-1} higher than that of **B**, the pre-exponential factor (A) for the reaction with **J** was also an order of magnitude greater. Overall, however, the difference in enthalpic terms (E_a) dominates such that the rate constants for **J** are an order of magnitude smaller than those of **B**. This result is consistent with the observed greater thermal stability of **J** versus **B** (onset temperature for H_2 release of 70 °C versus 50 °C), and points to enthalpic, rather entropic, factors as the origin of this differing behavior.

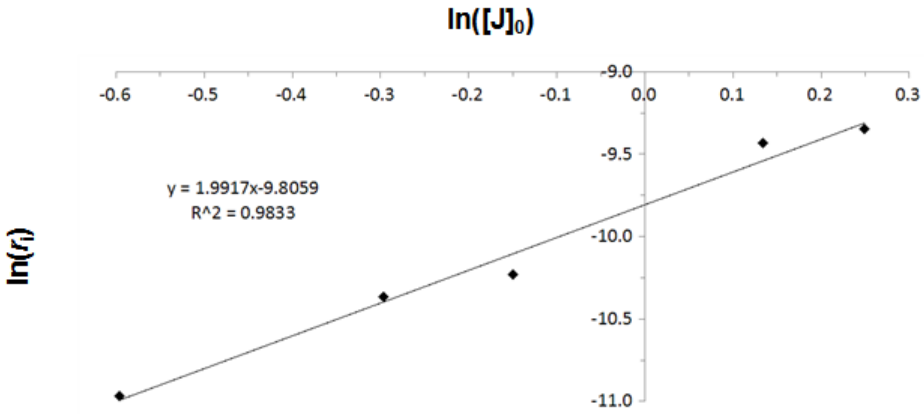

Figure 36. Reaction order determination by the initial rates method for the loss of the first H_2 equivalent from **J**.

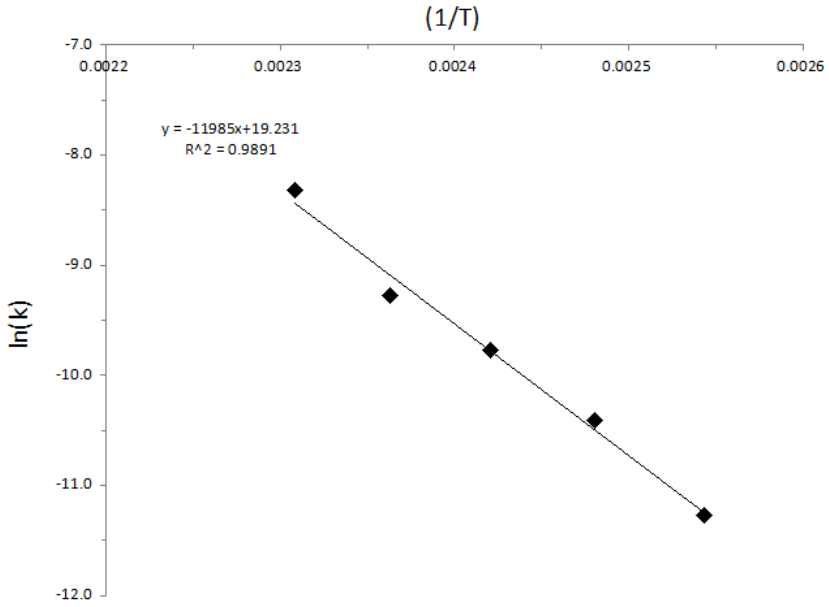

Figure 37. Arrhenius plot for the loss of the first H_2 equivalent from **J**.

Table 8. Comparison of experimentally determined Arrhenius parameters for **J** and **B**.

Reaction	E_a (kcal mol^{-1})	A (M^{-1} s^{-1})
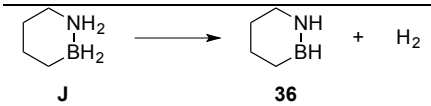 **J** **36**	+23.8	2.25×10^8
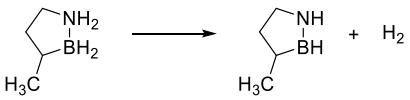 **B** **58**	+18.8	2.02×10^7

By applying the same bimolecular mechanistic model developed for **B**, a potential energy surface for initial H_2 release from **J** was calculated (Figure 38). As shown in Table

9, these calculations predicted a larger enthalpy ($\Delta H^{\ddagger}$), a less negative entropy ($\Delta S^{\ddagger}$), and an overall larger free energy ($\Delta G^{\ddagger}$) of activation for **J** compared to **B**, in complete agreement with the trends of the experimentally determined results.

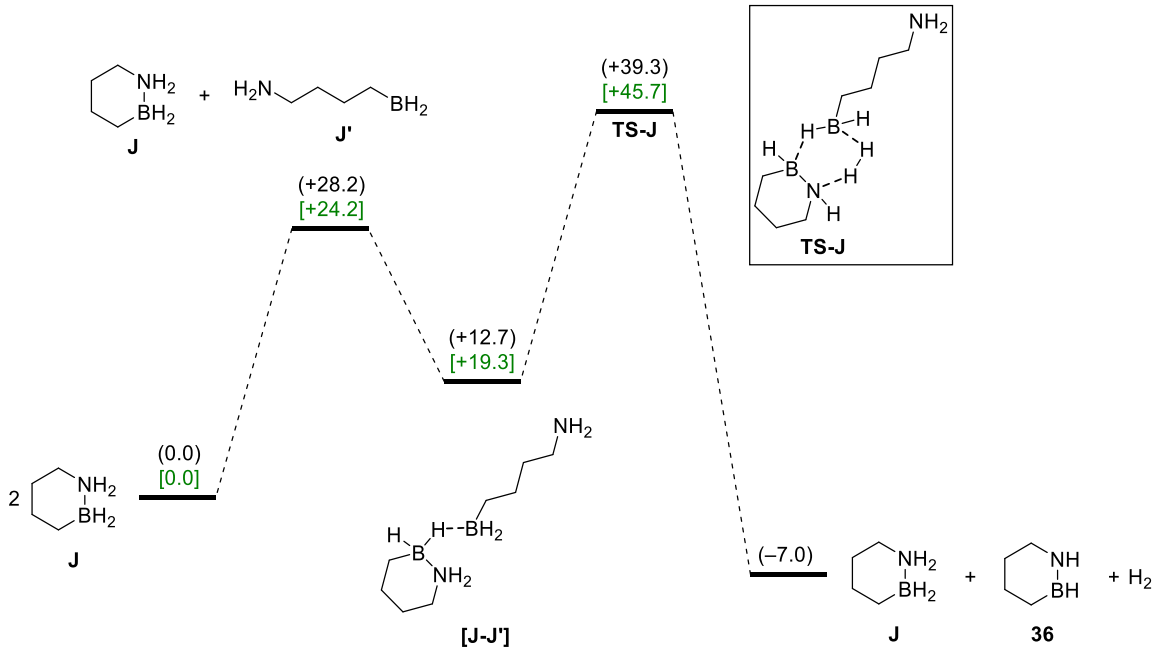

Figure 38. Potential energy surface for a proposed bimolecular H_2 release mechanism for **J**. Gas-phase enthalpy (black) and free energy [green] values (kcal-mol^{-1}) were calculated using G3MP2 (298K) based on geometries optimized using DFT at the B3LYP/DZVP2 level of theory.

Table 9. Computationally determined gas-phase enthalpy ($\Delta H^{\ddagger}$), entropy ($\Delta S^{\ddagger}$), and free energy of activation ($\Delta G^{\ddagger}$) (298 K) for **J** based on the potential energy surface shown in Figure 38 and comparison with values for **B**. $\Delta S^{\ddagger}$ values are extrapolated from the calculated $\Delta H^{\ddagger}$ and $\Delta G^{\ddagger}$ values.

Reaction	$\Delta H^{\ddagger}$ (kcal mol^{-1})	$\Delta S^{\ddagger}$ (cal mol^{-1} K^{-1})	$\Delta G^{\ddagger}$ (kcal mol^{-1})
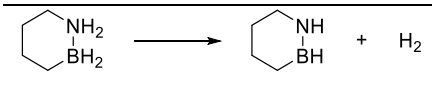 **J** **36**	+39.3	–21.5	+45.7
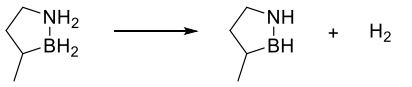 **B** **58**	+32.2	–27.8	+40.5

In collaboration with Prof. Andrew Weller at the University of Oxford, iridium and rhodium sigma-complexes of both **J** and **F** were prepared and characterized.[61] Specifically, stoichiometric addition of **J** or **F** to $[Ir(PCy)_3)_2(H)_2(H_2)_2][BAr^F{}_4]$ (**37**) afforded complexes **38** and **39** (Figure 39, top), respectively, while addition of two equivalents of either BN-heterocycle to $[Rh\{^{i}Pr_2P(CH_2)_3P^{i}Pr_2\}(\eta\text{-}C_6H_5F)][BAr^F{}_4]$ (**40**) likewise yielded complexes **41** and **42** (Figure 39, bottom). While isolated **38** and **39** proved stable in solution, in the presence of excess (5 equiv.) **J** or **F**, they appeared to

slowly catalyze BN-dehydrogenation to **35** and **22**, respectively (Scheme 19, top). Similar, somewhat more rapid reactivity was likewise observed for **41** and **42** (Scheme 19, bottom). At the conclusion of these latter reactions, the *tris*-μ-H rhodium dimer **43** was isolated (Figure 40). This species proved a significantly more active catalyst (TOF = 5 h^{-1} at 10 mol% loading) for the dehydrogenation of **F** compared to **42**. Kinetic studies also revealed a half-order concentration dependence with respect to **43**, suggesting it exists in a rapid equilibrium with another, monomeric species that serves as the actual active catalyst.

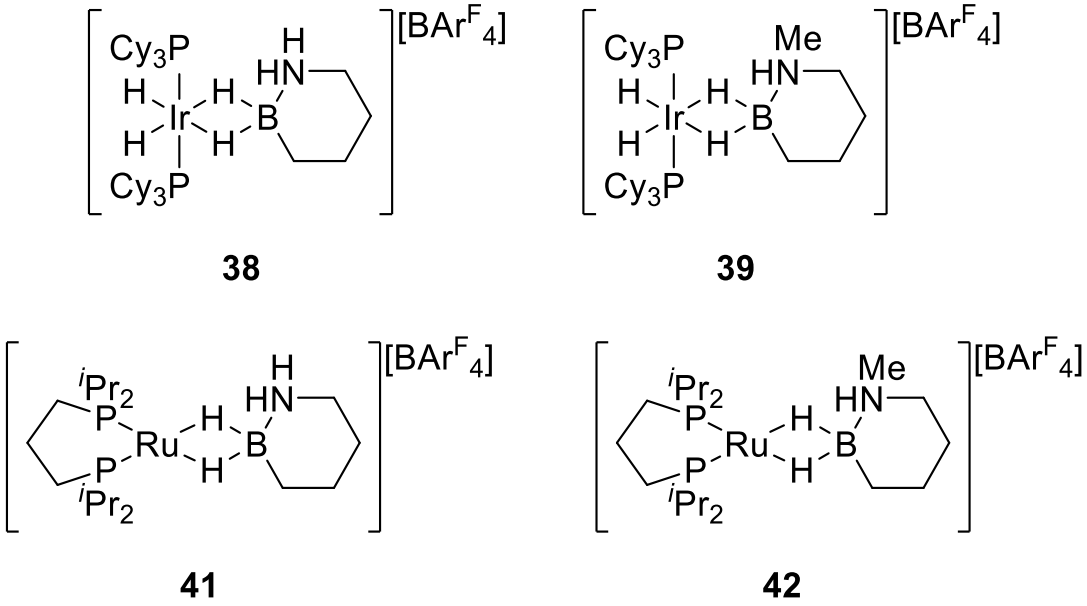

Figure 39. Iridium (top) and rhodium (bottom) sigma-complexes formed with **J** or **F**.

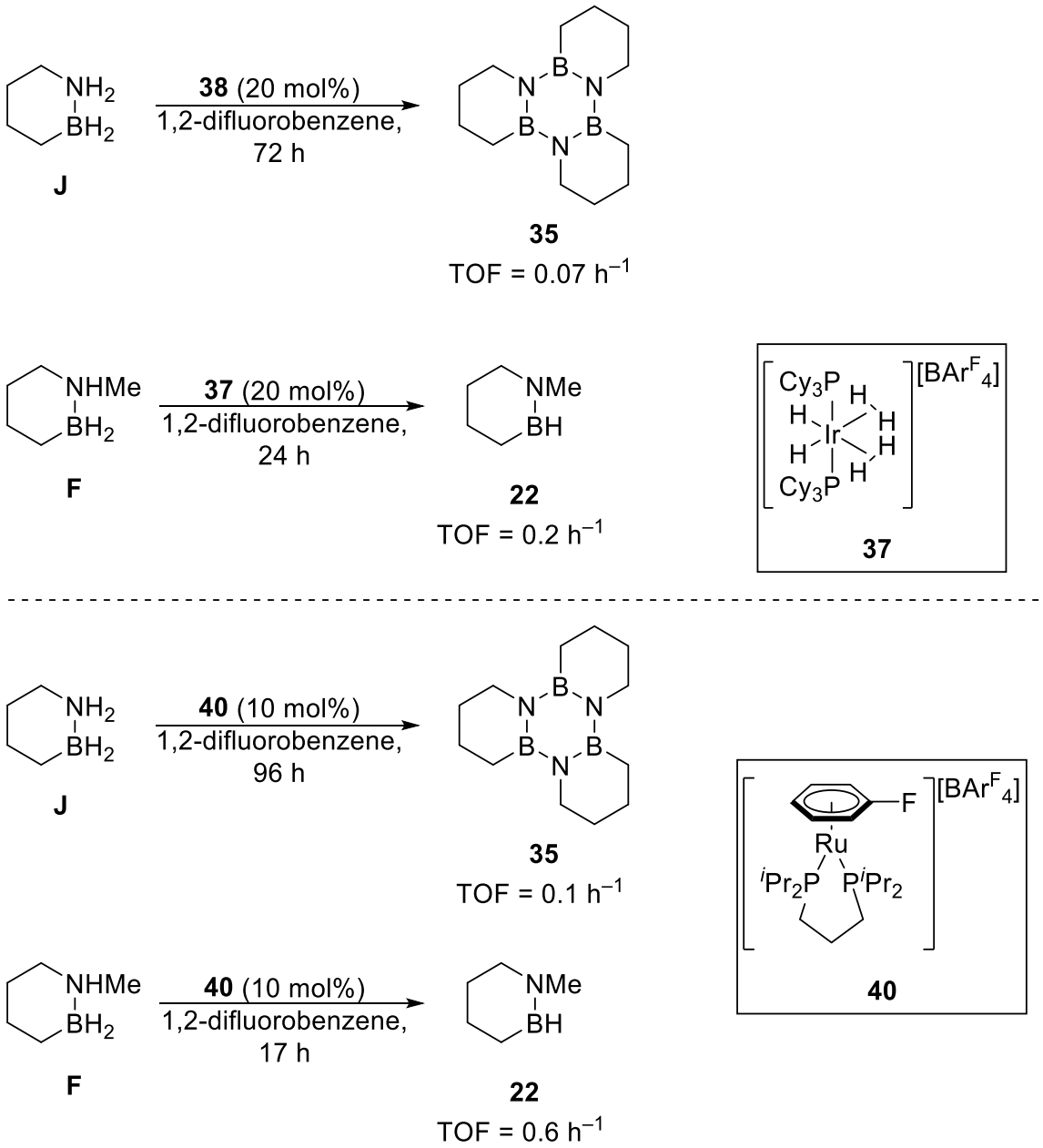

Scheme 19. Dehydrogenation of **J** and **F** catalyzed by homogeneous iridium (top) or rhodium (bottom) catalysts.

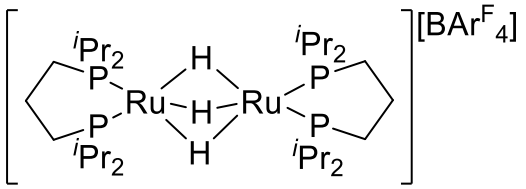

43

Figure 40. Kinetically competent *tris*-μ-H rhodium dimer **43** isolated from dehydrogenation reactions of **F** with rhodium pre-catalyst **40**.

2.10. Compound X

1,2-dimethyl-1,2-BN-cyclohexene (**X**) was designed as a model substrate to facilitate development of a heterogeneous catalytic system for gas-phase CC dehydrogenation of saturated BN-heterocycles. In solution, this reaction had previously proven possible only through the use of a homogeneous iridium complex and transfer hydrogenation using a hydrogen acceptor (*trans*-stilbene).[30] Hence, it appeared a shift to gas-phase catalysis was necessary in order to achieve dehydrogenation with production of free H_2. This would in turn require a sufficiently volatile, liquid substrate, and so **X** was selected as the material of lowest molecular weight that would still avoid the possibility of competitive -CH_2–NH- or -CH_2–BH- dehydrogenation.

The synthesis of **X** began with the addition of *N*-allyl-*N*-methylamine to allylboron difluoride, generated *in situ* from potassium allyltrifluoroborate and TMSCl (Scheme 20). Ring-closing metathesis of diene **44**, followed by *B*-methylation with methylmagnesium bromide then yielded unsaturated intermediate **45**. Conveniently, this compound afforded access to both **X** itself (via Pd/C-catalyzed hydrogenation) and the fully dehydrogenated product **46** (via Pd/C-catalyzed dehydrogenation).

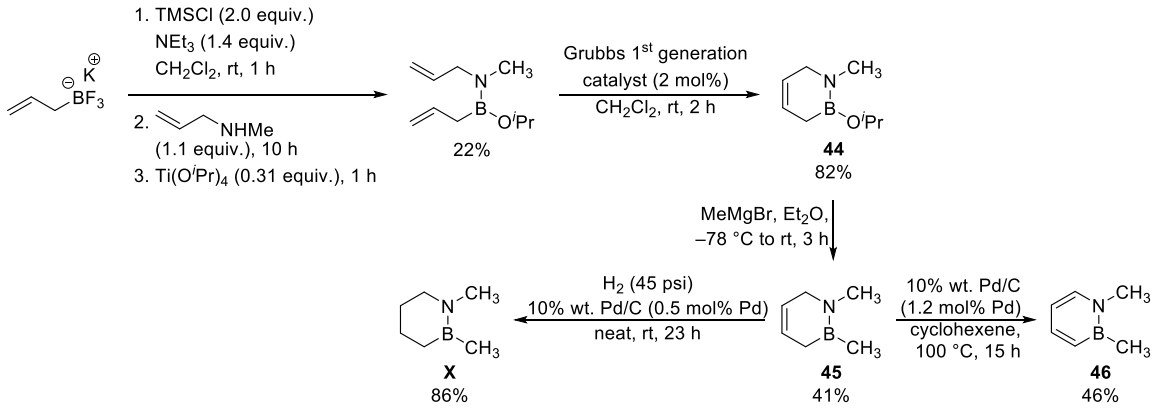

Scheme 20. Synthesis of CC dehydrogenation model substrate **X** and product **46** from potassium allyltrifluoroborate.

Gas-phase dehydrogenation reactions of **X** were performed using the flow system shown in Figure 41-A. A syringe pump (Figure 41-B) was used to inject neat **X** into an argon stream directly above a U-bend quartz reactor tube (Figure 41-C) packed on one side with layers of glass wool, loose quartz, and a mixture of quartz and catalyst above a porous glass frit. A digitally controlled furnace was used to heat the tube to the desired reaction temperature, and the reactor outflow was sent directly to a mass spectrometer (EI ionization mode) for real-time reaction monitoring.

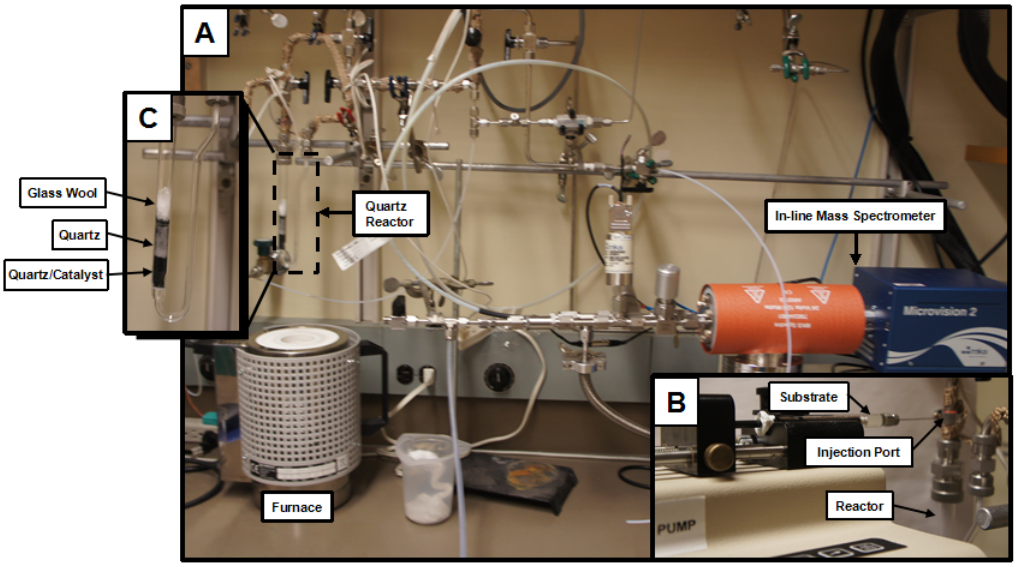

Figure 41. (A) Gas flow system for dehydrogenation reactions with in-line mass spectrometer for product analysis; (B) substrate injection syringe pump set-up; and (C) quartz reactor tube assembly.

A number of commercially available heterogeneous catalysts were screened for CC dehydrogenation activity using this set-up. Gratifyingly, simple Pd/C (10 wt. % Pd) was found to effect continual dehydrogenation of **X** beginning at 170 ºC under flow conditions (Figure 42-A). Significantly, at all temperatures studied, H_2 and **46** were consistently evolved in a 2:1 molar ratio, indicating the former to derive entirely from complete CC dehydrogenation of **X** (Figure 42-B).

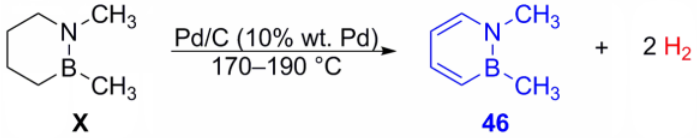

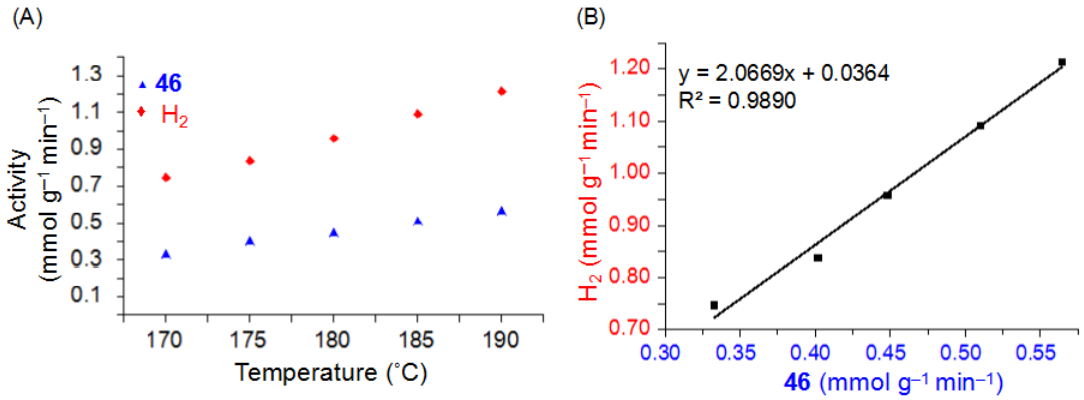

Figure 42. (A) Rates of **46** and H_2 formation normalized by mass catalyst; (B) comparison of H_2 and **46** evolution rates.

Having established reliable conditions for dehydrogenation of **X**, the kinetics of the reaction were studied at various temperatures (170–190 ºC) in order to determine the

Arrhenius activation parameters using the Basset-Habgood equation;[62] these were compared to those determined for the all-carbon analogue dimethylcyclohexene (DMC)[63] under similar experimental conditions.[64] Although we formally assigned **X** to the same cyclohexene-type oxidation level as DMC, it was unknown at the outset whether or not the B−N bond in **X** would indeed predispose the substrate to CC dehydrogenation to the same extent as the isosteric C=C bond in DMC. We reasoned that less favorable Arrhenius terms would be indicative of a correspondingly less activated substrate, more akin kinetically to a cyclohexane-like molecule.[65]

We thus first compared the dehydrogenation kinetics of unsubstituted, all-carbon cyclohexene and cyclohexane in order to establish that substrates at different levels of oxidation would indeed exhibit different kinetic profiles in our particular reactor system. As shown in entries 1 and 2 of Table 10, the dehydrogenation kinetics of cyclohexene and cyclohexane are indeed clearly distinguishable on the basis of their Arrhenius terms; the activation energy (E_a) for cyclohexane is 2.0 kcal-mol^{-1} greater than that for cyclohexene, and its pre-exponential factor (A) is also more than two orders of magnitude smaller. In a similar vein, the E_a for **X** is 1.7 kcal-mol^{-1} greater than that for DMC, and its pre-exponential factor is approximately an order of magnitude smaller. In this respect, the relationship between the activation parameters for **X** and DMC mirrors that for those of cyclohexane and cyclohexene, indicating there does appear to be a disparity between the B−N and C=C bonds with respect to the kinetic favorability of CC dehydrogenation.

Table 10. Measured Arrhenius activation parameters for dehydrogenation of **X**, cyclohexene, and cyclohexane.

Entry	Reaction[a]	E_a (kcal mol^{-1})	log(A)
1[b]	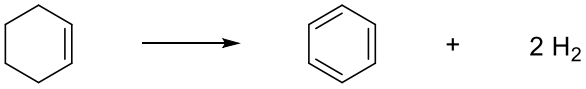	10.9±0.2	5.6±0.2
2[b]	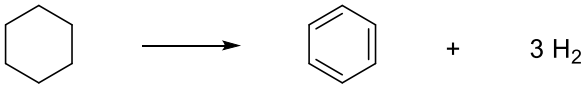	12.9±0.1	3.1±0.4
3[c,d]	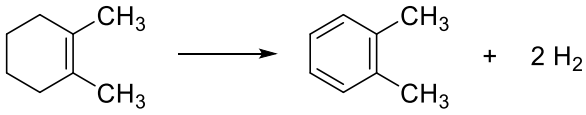	8.6±0.3	3.6±0.1
4[b]	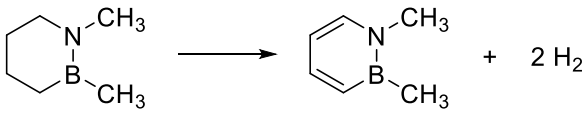	10.3±0.3	2.2±0.2

X **46**

[a] Conditions: 50 mL-min^{-1} Ar carrier gas, 20 mg 10 wt% Pd/C; substrate injection rates (mmol s^{-1}): cyclohexene (1.10×10^{-4}), cyclohexane (1.03×10^{-4}), dimethylcyclohexene (1.03×10^{-4}), **X** (1.04×10^{-4}); hydrogen evolution rates measured from 70–110 °C at 10 °C increments for cyclohexene, from 170–190 °C at 5 °C increments for cyclohexane, **1**, and 1,2-dimethylcyclohexane, and from 70–90 °C at 5 °C increments for dimethylcyclohexene. All reactions were repeated in triplicate. Error ranges were calculated as the standard deviation from the mean.

[b] Values based on quantification of dehydrogenated product mass signal. Complementary analysis based on the H_2 mass signal gave similar results for **X**.

[c] A 5:1 mixture of 1,2- and 1,6-dimethylcyclohexene was used.

[d] Values based on quantification of the H_2 mass signal.

Successful dehydrogenation of **X** led to the hypothesis that it might be possible to *kinetically* couple endothermic CC H_2 release with exothermic BN H_2 release in an intramolecular fashion. To test this idea, 1,2-dimethyl-1,2-BN-cyclohexane (**XH_2**) was prepared from **X** by step-wise reduction with $LiAlH_4$, followed by protonation with MeOH at –78 ºC (Scheme 21). X-ray crystallography confirmed the isolation of **XH_2** as a single diastereomer with both methyl groups occupying the equatorial positions of a chair conformation (Figure 43). Calculations (G3MP2) indicated this conformation to be lower in free energy than the form with diaxial methyl substituents and either conformer of the *cis*-dimethyl diastereomer ($\Delta\Delta G_{298K}$ = 1.3–2.5 kcal-mol^{-1}).

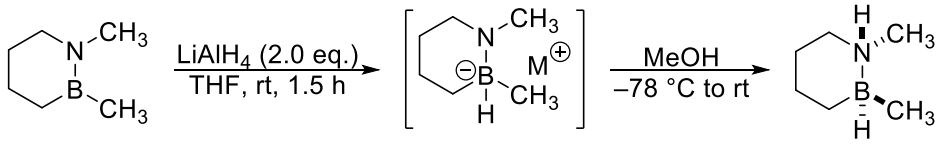

X **XH_2**

58%

Scheme 21. Synthesis of **XH_2** from **X**.

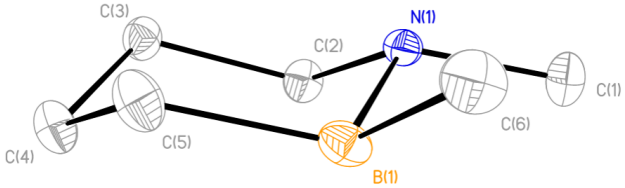

Figure 43. X-ray crystal structure of **XH_2** showing thermal ellipsoids at 35% probability. Hydrogen atoms omitted for clarity.

Although **XH_2** itself proved to be a solid at room temperature (mp = 56 ºC), it was found to be appreciably soluble in **X**. It could thus be introduced into the flow reactor system as a 2:1 **XH_2**:**X** molar ratio blend. Unfortunately, under the standard reaction conditions, the amounts of H_2 produced separately from BN and CC dehydrogenation could not be deconvoluted. This problem was circumvented by the use of a BN-di-deutero-labelled variant of the BN-cyclohexane component (**XD_2**). A control reaction of the dehydrogenation of **XD_2**:**X** (2:1) in the *absence* of Pd/C, however, revealed the formation of scrambled HD (Figure 44). Furthermore, the amounts of D_2 observed could not account for the measured increase in **X** (expected from the thermal decomposition of **XD_2**) above the initial amounts injected. The combined levels of HD and D_2, however, exceeded the amount of additional **X** generated. Based on these results, it appears that **XD_2** undergoes multiple decomposition pathways in the presence of **X** to other as yet unidentified products. Given the complexity of the system, further investigation of the **XD_2**:**X** mix for evidence of kinetic coupling was not pursued.

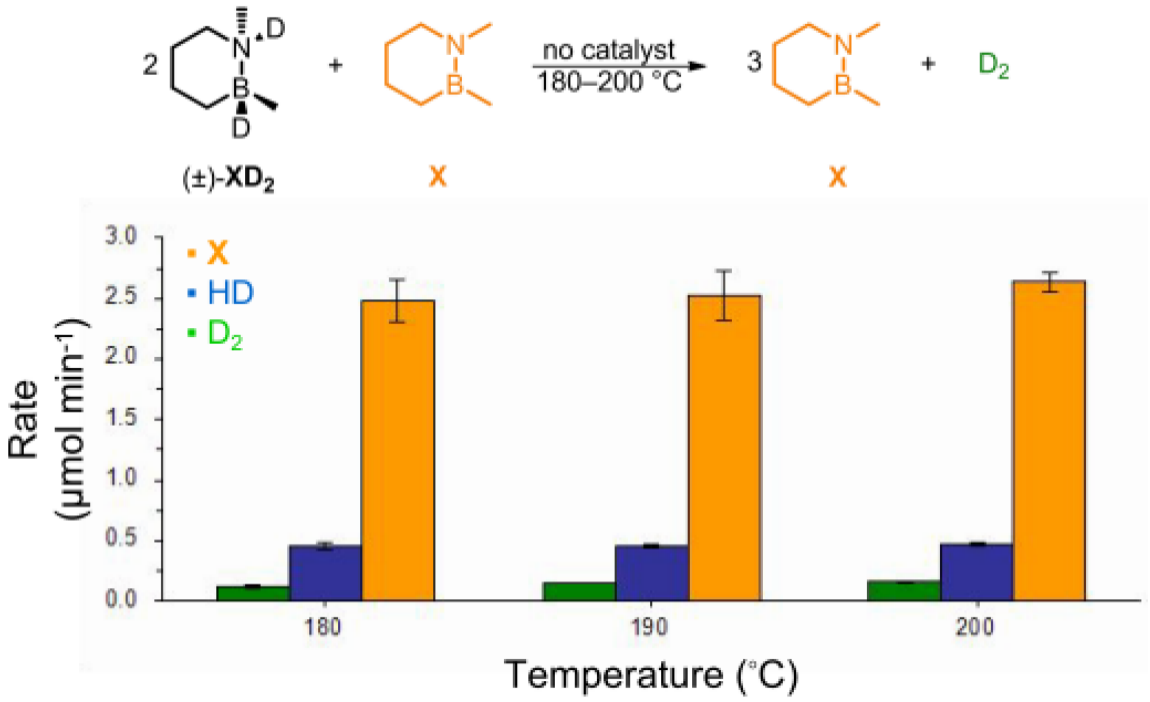

Figure 44. Quantification of species detected in control dehydrogenation reactions of **XD_2**:**X** (2:1 molar ratio) mixture at 180–200 ºC in the absence of Pd/C catalyst.

2.11. Linear B-Methyl Compounds

To complement our investigation of cyclic *B*-alkyl substituted amine-borane hydrogen storage materials, e.g. **B**, **J**, **H**, we also investigated the properties of linear variants of these compounds, which had received comparatively little prior attention.[66,67] Thus, we performed a salt metathesis[68] of $LiMeBH_3$[69] and either NH_4Cl or $MeNH_3Cl$ to furnish either *B*-methylamine borane (**47**) or *B,N*-dimethylamine borane (**48**), respectively (Scheme 22).[70] While neat **47** was found to decompose upon melting (mp = 58 °C) or in solution (55 °C, THF), **48** was stable to successive melt-freeze cycles (mp = 47 °C) and heating in solution (55 °C, THF) for up to 2 d.

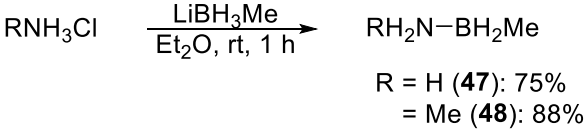

Scheme 22. Synthesis of **47** and **48** via salt metathesis.

The $CoCl_2$-catalyzed dehydrogenation activities of **47** and **48** were evaluated using an automated gas burette (Figure 45). In digylme at 80 °C, loss of 1.75 H_2 equivalents was achieved in 20 min for **47** and 35 min for **48**. Notably, these rates are similar to that observed for **B**, and approximately twice that of unsubstituted ammonia borane itself under the same conditions (0.75 H_2 equiv. in 45 min).

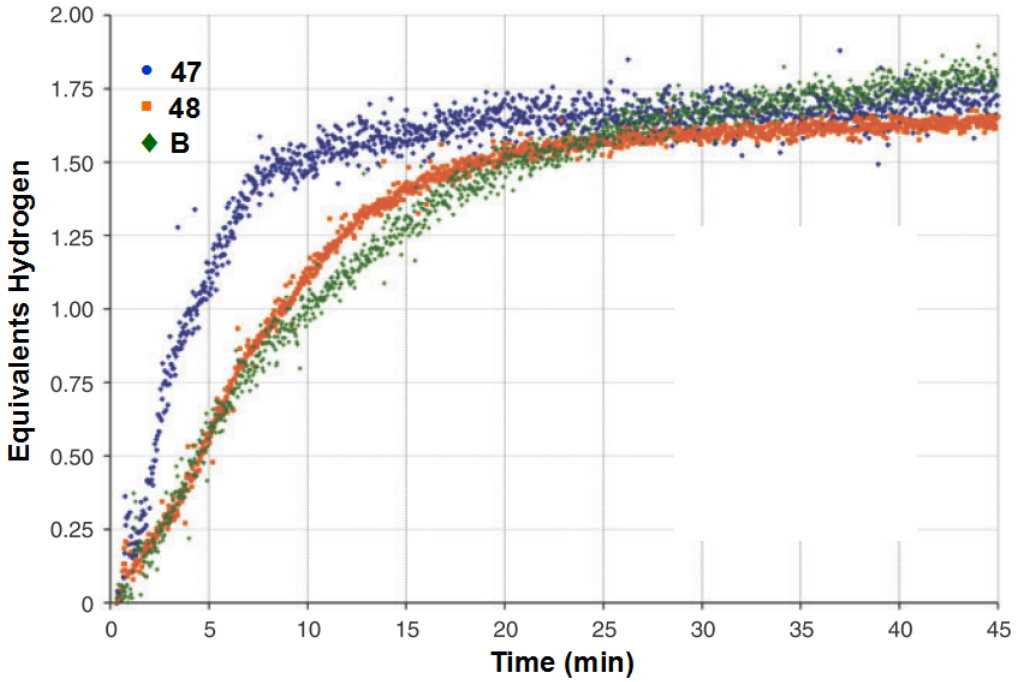

Figure 45. Automated gas burette traces of catalyzed H_2 release from **47**, **48**, and **B**. Conditions: 75 mg substrate, $CoCl_2$ (5 mol%), diglyme (3 mL), 80 °C.

Also in contrast to the well-known unselective decomposition of AB, both **47** and **48** converted exclusively to the fully dehydrogenated trimeric species **49** and **50**, respectively after prolonged heating (Scheme 23). Significantly, addition of formic acid to **49** resulted in clean formation of the tris(formyloxy) adduct **51**, whose structure was confirmed by X-ray crystallography (Scheme 24, top). Reduction of **51** with $LiAlH_4$ then regenerated **48** in modest yield following protic workup (Scheme 24, bottom).

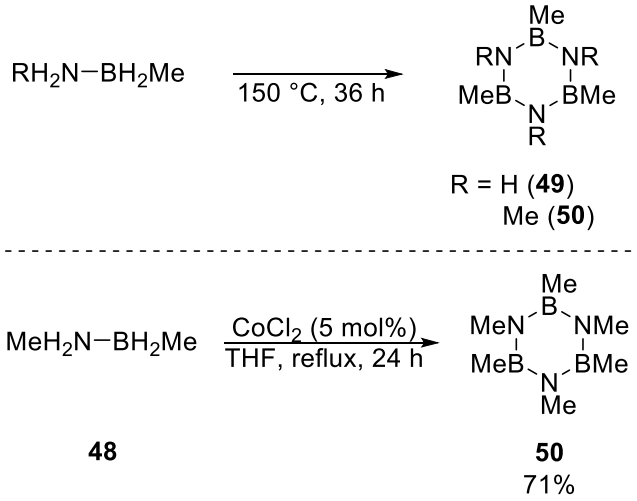

Scheme 23. Formation of trimers **49** and **50** by thermal decomposition of **47** and **48**, respectively (top), and isolation of **50** from $CoCl_2$-catalyzed dehydrogenation of **48** (bottom).

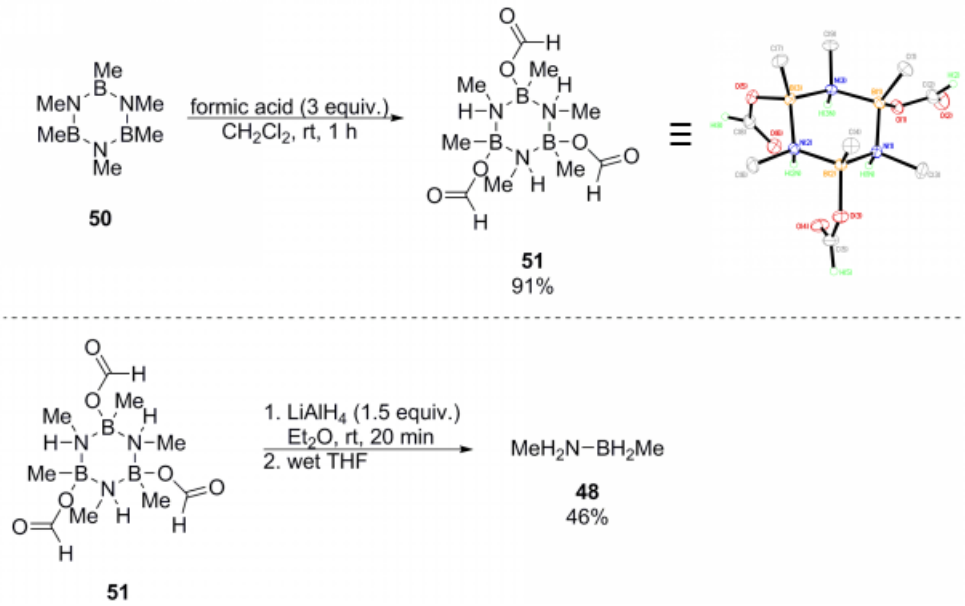

Scheme 24. Formation of tris(formyloxy) adduct **51** (top), and regeneration of **48** with $LiAlH_4$ (bottom).

2.12. Frustrated Lewis Pairs

In addition to 1,3-BN-cyclohexane (**E**), substituted 1,4-BN-heterocycles were also investigated as possible FLP-type hydrogen storage materials. Dehydrogenation of the C(3)– and C(5)–CH_3 bonds in **52-54** was calculated (B3LYP/DZVP2) to be highly endothermic and endergonic, regardless of the electronic nature of the exocyclic boron substituent (Table 11). In contrast, the thermodynamics of H_2 release from across the 1,4-BN unit was predicted to vary considerably with differing boron substitution, with the reaction becoming less exothermic and exergonic as the electron-withdrawing power of the substituent increased (Table 12). (For a more comprehensive theoretical examination of the thermodynamics of complete dehydrogenation of **52-54**, see Section 3.2.)

Table 11. Calculated (B3LYP/DZVP2) thermodynamics for dehydrogenation of the exocyclic methyl groups on 1,4-BN-heterocycles **52-54**.

Reaction	ΔH_{298K} (kcal mol^{-1})	ΔG_{298K} (kcal mol^{-1})
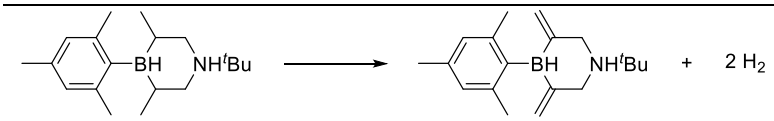 **52**	+46.8	+29.0
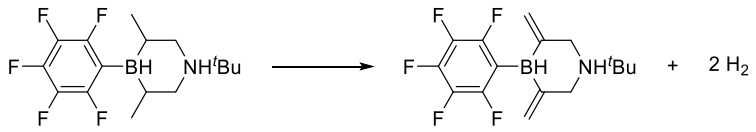 **53**	+50.6	+33.5
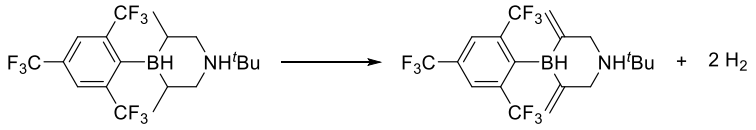 **54**	+47.4	+31.0

Table 12. Calculated (B3LYP/DZVP2) thermodynamics for H_2 loss across the BN unit of various substituted 1,4-BN-heterocycles.

Reaction	ΔH_{298K} (kcal mol^{-1})	ΔG_{298K} (kcal mol^{-1})
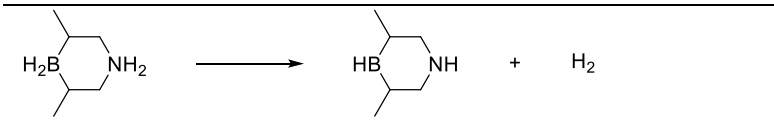	–9.3	–18.7
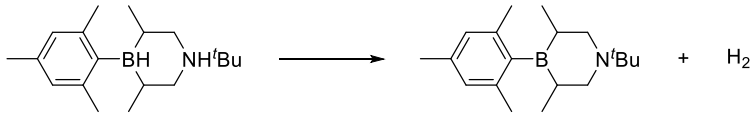 **52**	–11.0	–21.7
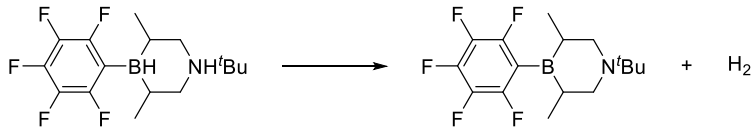 **53**	+2.9	–7.3
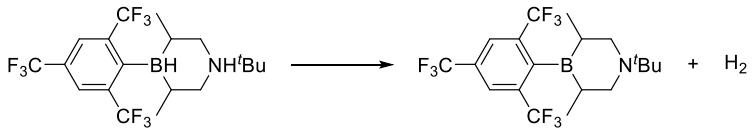 **54**	–5.4	–15.7

B,*N*-didehydro-1,4-BN-cyclohexane **55** was synthesized by dihydroboration of *N*-(*tert*-butyl)-*N*,*N*-di-(1-propen-1-yl)amine (**56**) with (2,4,6-tris(trifluoromethyl)phenyl)borane (**57**; Scheme 25, bottom). A dichloromethane solution of **55** was placed under a hydrogen atmosphere (600 psi) in a sealed NMR tube and monitored by ^{11}B NMR for H_2 splitting activity (Figure 46). After 21 h, in addition to remaining starting material, additional peaks at +35, +7, and –2 ppm had appeared

(Figure 46c); the splitting of the –2 ppm peak appeared to correspond to the formation of a B–H bond, but when the hydrogen pressure was released, this peak disappeared (Figure 46d), indicating the associated species is possibly unstable.

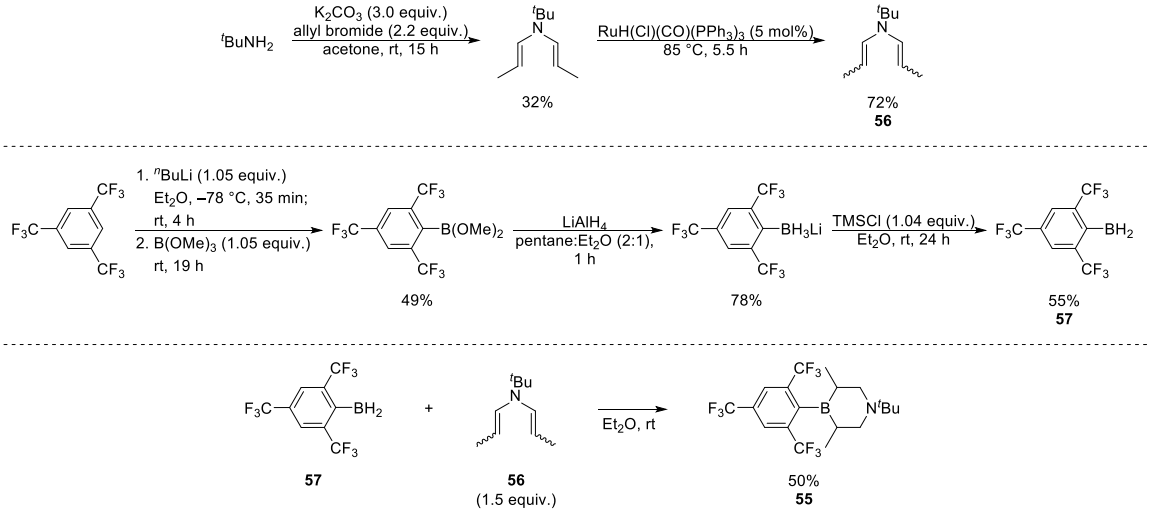

Scheme 25. Synthesis of **55** starting from *tert*-butylamine (top) and (2,4,6-tris(trifluoromethyl)phenyl)borane (middle).

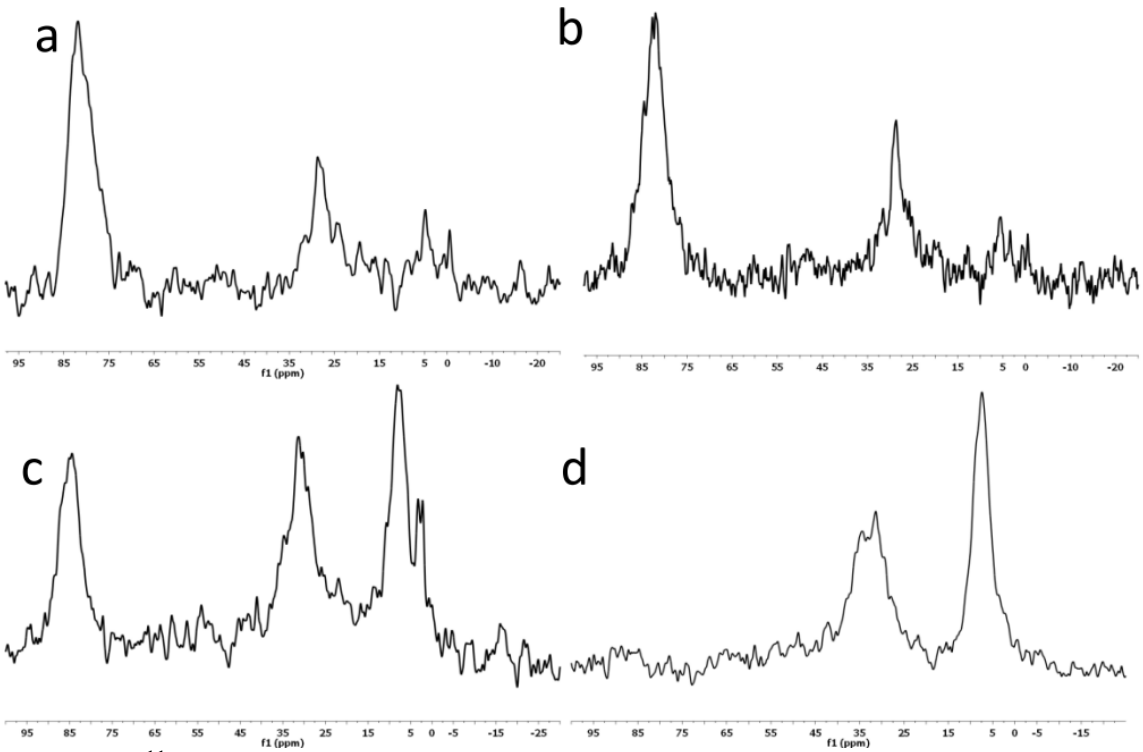

Figure 46. ^{11}B NMR spectra of **55** a) prior to addition of H_2, b) under H_2 (600 psi) at t = 0 h, c) under H_2 (600 psi) at t = 21 h, and d) after depressurization.

3. Computations

3.1. Material Properties

The gas-phase heats of formation ($\Delta H_{f,gas}$) were calculated (G3MP2) for **A–D**, **J**, and a series of their possible dehydrogenation products (Table 13). The boiling points (T_{BP}) for all these species were also calculated (COSMO-R); assuming, based on the Pictet-Trouton rule, a general entropy of vaporization (ΔS_{vap}) of 25 e.u., these boiling points were in turn used to predict each compound's heat of vaporization (ΔH_{vap}) using the equation $\Delta H_{vap} = T_{BP}\Delta S_{vap}$. Subtracting this ΔH_{vap} value from the calculated $\Delta H_{f,gas}$ value then produced an estimate of the compound's liquid phase heat of formation ($\Delta H_{f,liq}$).

Table 13. Calculated gas- and liquid-phase heats of formation (ΔH_f) and boiling points (T_{BP}) for **A–D**, **J**, and some related dehydrogenated species.

	Compound							
	 **A**							
$\Delta H_{f,gas}$ (kcal mol^{-1})	–14.0	–19.8	+3.8	+4.5	+62.2	+87.4	+82.2	+84.5
$\Delta H_{f,liq}$ (kcal mol^{-1})	–27.7	–27.6	–4.6	–3.5	+52.1	+75.1	+73.2	+77.5
T_{BP} (K)	465	311	335	485	374	358	397	403
	 **B**	 **58**						
$\Delta H_{f,gas}$ (kcal mol^{-1})	–19.7	–24.5	+0.7	–3.8	+54.0	+81.6	+73.4	+79.6
$\Delta H_{f,liq}$ (kcal mol^{-1})	–28.4	–33.1	–12.8	–8.1	+43.7	+71.0	+63.3	+69.4
T_{BP} (K)	570	345	362	351	409	405	324	413
	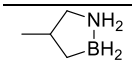 **C**	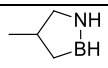	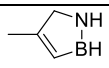	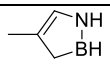	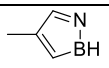	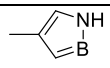	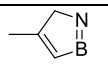	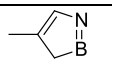
$\Delta H_{f,gas}$ (kcal mol^{-1})	–21.4	–27.0	–5.2	–3.7	+51.7	+75.6	+72.0	+79.6
$\Delta H_{f,liq}$ (kcal mol^{-1})	–30.0	–35.6	–14.0	–13.1	+40.6	+68.8	+61.9	+65.7
T_{BP} (K)	572	342	350	376	407	399	446	432

	 D							
$\Delta H_{f,gas}$ (kcal mol^{-1})	–22.7	–28.7	–5.6	–4.1	+48.5	+72.6	+73.2	+77.6
$\Delta H_{f,liq}$ (kcal mol^{-1})	–31.3	–37.2	–14.8	–13.1	+38.0	+77.5	+75.1	+73.2
T_{BP} (K)	572	345	368	357	396	392	437	422

	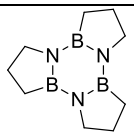	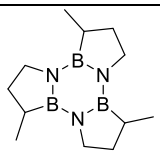 6	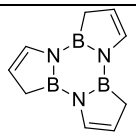	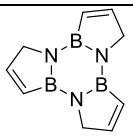
$\Delta H_{f,gas}$ (kcal mol^{-1})	–120.5	–136.1	–47.1	–48.5
$\Delta H_{f,liq}$ (kcal mol^{-1})	–137.2	–155.0	–63.6	–65.5
T_{BP} (K)	670	759	658	682

	 J	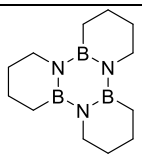 35	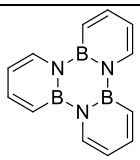
$\Delta H_{f,gas}$ (kcal mol^{-1})	–23.3	–146.1	–49.1
$\Delta H_{f,liq}$ (kcal mol^{-1})	–37.7	–165.8	–68.4
T_{BP} (K)	577	790	771

The gas-phase heats of formation ($\Delta H_{f,gas}$) were also calculated (G3MP2) for **XH_2** and the related BN and CC dehydrogenation products (Table 14).

Table 14. Calculated (G3MP2) gas-phase heats of formation for **XH_2** and related dehydrogenated species.

	Compound			
	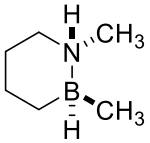 **XH_2**	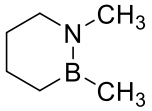 **X**	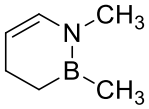	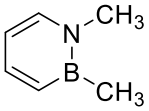 **46**
$\Delta H_{f,gas}$ (kcal mol^{-1})	–38.6	–44.0	–18.3	–10.5

The B–N bond dissociation energies (BDE) for **A–D**, **F**, **J**, and several acyclic ammonia borane derivatives were calculated using G3MP2 (Table 15). Both the gas- and solution-phase free energies (ΔG) for this bond cleavage at 298 K were also calculated; these values were in turn used to predict the equilibrium constants (K_{eq}) between the B–N associated and dissociated species. Of note, the BDE of the BN-cyclopentanes (**A–D**) are on average 5 kcal-mol^{-1} lower than those of the BN-cyclohexanes (**F** and **J**). This difference presumably arises from greater molecular strain in the five-membered ring systems. Within the BN-cyclopentane series itself, the presence of a methyl substituent on any of the ring carbons does not appear to significantly affect the BDE. In contrast, *N*-methylation in a six-membered framework results in an increase of ~4 kcal-mol^{-1} (**F** versus **J**). The gas-phase ΔG values for B–N dissociation of the acyclic compounds are generally less positive than those of the cyclic systems owing to the entropically favored formation of two separate species as a result of bond cleavage. In all cases, however, solvation, more so by THF than by Et_2O, appears to increase the ΔG value for dissociation and shift the equilibrium constants to more significantly favor the associated species.

Table 15. Calculated (G3MP2) B–N bond dissociation energies (BDE), and associated gas- and solution-phase free energies (ΔG) and equilibrium constants (K_{eq}) at 298 K.

	Compound					
	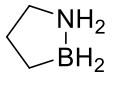	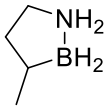	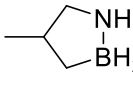	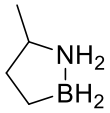	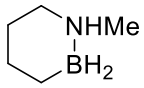	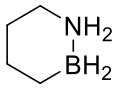
	A	**B**	**C**	**D**	**F**	**J**
BDE (kcal mol^{-1})	+25.2	+26.2	+24.4	+25.9	+32.5	+28.6
ΔG_{gas} (kcal mol^{-1})	+22.0	+23.7	+22.2	+22.6	+27.8	+24.2
ΔG_{ether} (kcal mol^{-1})	+25.6	+27.4	+26.5	+26.6	+31.1	+28.2
ΔG_{THF} (kcal mol^{-1})	+29.9	+31.7	+31.5	+31.3	+35.0	+32.8
$K_{eq,gas}$	6.67×10^{-17}	4.31×10^{-18}	4.95×10^{-17}	2.82×10^{-17}	4.19×10^{-21}	1.62×10^{-18}
$K_{eq,ether}$	1.52×10^{-19}	8.33×10^{-21}	3.59×10^{-20}	3.05×10^{-20}	1.49×10^{-23}	2.14×10^{-21}
$K_{eq,gas}$	1.14×10^{-22}	5.61×10^{-24}	7.89×10^{-24}	1.06×10^{-23}	1.98×10^{-26}	9.16×10^{-25}

	Compound			
	$H_3N{-}BH_3$	$MeH_2N{-}BH_3$	$H_3N{-}BH_2Me$ (**47**)	$MeH_2N{-}BH_2Me$ (**48**)
BDE (kcal mol^{-1})	+27.7	+33.5	+28.3	+22.5
ΔG_{gas} (kcal mol^{-1})	+17.9	+23.2	+16.1	+11.5
ΔG_{ether} (kcal mol^{-1})	+24.3	+28.9	+20.3	+16.3
ΔG_{THF} (kcal mol^{-1})	+31.7	+35.6	+25.3	+22.0
$K_{eq,gas}$	7.51×10^{-14}	1.02×10^{-17}	1.65×10^{-12}	3.92×10^{-9}
$K_{eq,ether}$	1.52×10^{-18}	6.08×10^{-22}	1.23×10^{-15}	1.08×10^{-12}
$K_{eq,gas}$	5.44×10^{-24}	7.52×10^{-27}	2.79×10^{-19}	7.86×10^{-17}

The ^{11}B NMR chemical shifts (δ) for **A**, **B**, **J**, and various related dehydrogenated species were calculated to aid in their identification in the product mixtures of H_2 release experiments (Table 16).

Table 16. Calculated ^{11}B NMR chemical shifts (δ) for **A**, **B**, **J**, and related compounds. Chemical shift values referenced against BF_3•Et_2O (δ = 0.0 ppm).

Compound	δ (ppm)	Compound	δ (ppm)	Compound	δ (ppm)
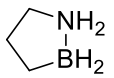 **A**	–13.3	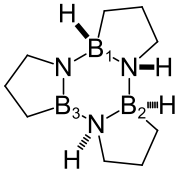	–5.3 (B_1) –8.8 (B_2) +35.5 (B_3)	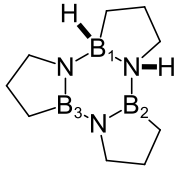	–4.5 (B_1) +41.5 (B_2) +33.2 (B_3)
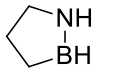	+40.9	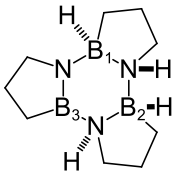	–4.8 (B_1) –5.0 (B_2) +36.8 (B_3)	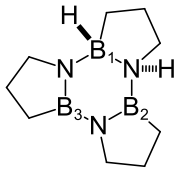	–5.4 (B_1) +43.4 (B_2) +35.3 (B_3)
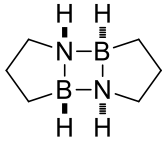	–3.0	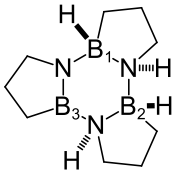	–5.6 (B_1) –7.1 (B_2) +38.0 (B_3)	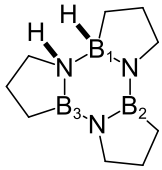	–4.7 (B_1) +31.1 (B_2) +39.5 (B_3)
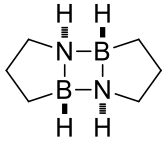	–1.7	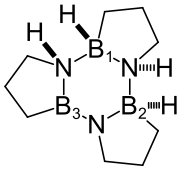	–8.6 (B_1) –6.0 (B_2) +31.3 (B_3)	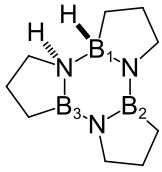	–3.8 (B_1) +32.8 (B_2) +39.8 (B_3)
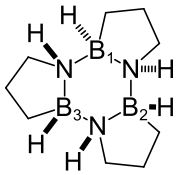	–8.8 (B_1) –8.2 (B_2) –6.2 (B_3)	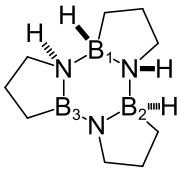	–5.3 (B_1) –4.6 (B_2) +32.0 (B_3)	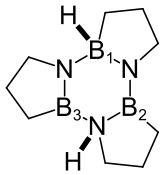	–7.2 (B_1) +30.7 (B_2) +33.6 (B_3)
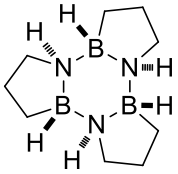	–4.3	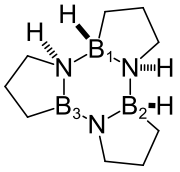	–6.1 (B_1) –4.9 (B_2) +35.1 (B_3)	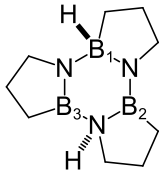	–6.8 (B_1) +28.9 (B_2) +33.2 (B_3)
				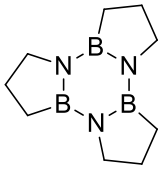	+35.6
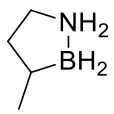 **B**	–11.4	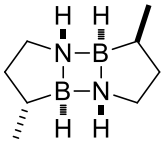	–3.0	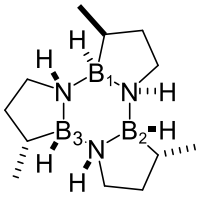 **60**	–6.1 (B_1) –5.2 (B_2) –6.4 (B_3)

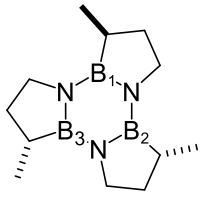

+35.5 (B_1)
+35.7 (B_2)
+34.9 (B_3)

61

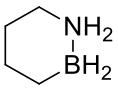

–14.3

J

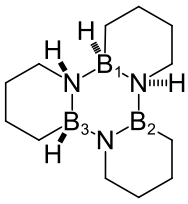

–9.5 (B_1)
+32.3 (B_2)
–7.9 (B_3)

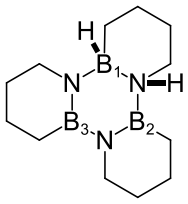

–6.1 (B_1)
+37.7 (B_2)
+29.7 (B_3)

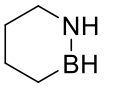

+38.4

36

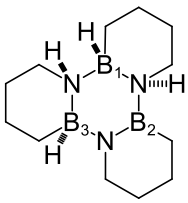

–10.7 (B_1)
+34.3 (B_2)
–9.1 (B_3)

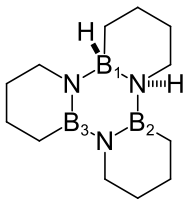

–7.8 (B_1)
+38.1 (B_2)
+31.0 (B_3)

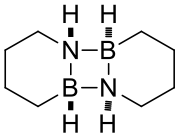

–9.3

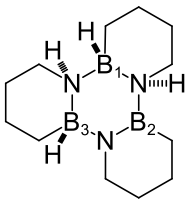

–10.0 (B_1)
+31.3 (B_2)
–8.0 (B_3)

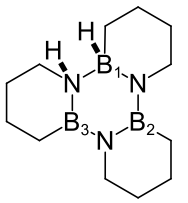

–1.4 (B_1)
+28.3 (B_2)
+38.7 (B_3)

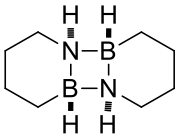

–2.2

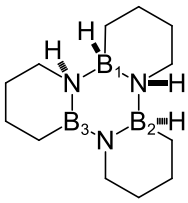

–11.3 (B_1)
–8.7 (B_2)
+32.8 (B_3)

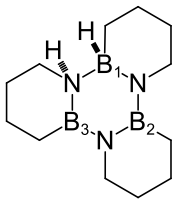

–9.7 (B_1)
+30.6 (B_2)
+37.4 (B_3)

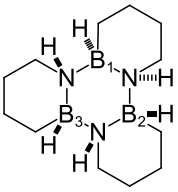

–11.0 (B_1)
–9.3 (B_2)
–5.6 (B_3)

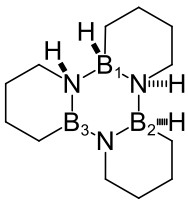

–11.3 (B_1)
–5.5 (B_2)
+30.2 (B_3)

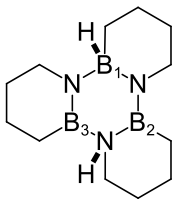

–11.6 (B_1)
+30.0 (B_2)
+31.6 (B_3)

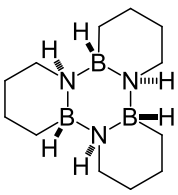

–4.3

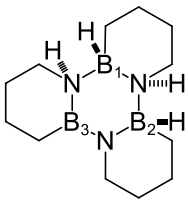

–9.6 (B_1)
–9.6 (B_2)
+30.9 (B_3)

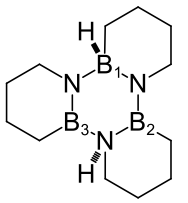

–10.4 (B_1)
+28.1 (B_2)
+28.6 (B_3)

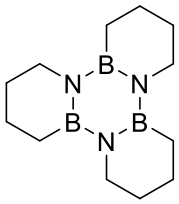

+31.9

35

The vapor pressures at 80 ºC of **B** and the products after initial loss of H_2 (**58**) and after trimerization (**6**) were calculated using COSMO-RS (Table 17). Notably, while release of the first H_2 equivalent renders **58** significantly more volatile than **B**, trimer **6** is effectively non-volatile under the same conditions. These predictions are consistent with the results of TGA-MS experiments which did not detect mass loss at 80 ºC due vaporization of **B** or **6** (see Section 2.2).

Table 17. Calculated vapor pressures of **B** and related compounds at 80 ºC.

	Compound		
	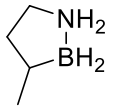 **B**	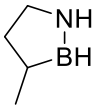 **58**	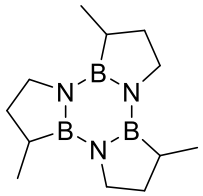 **6**
Vapor pressure (Torr)	1.5	937	0.03
T_{BP} (K)	570	345	759

3.2. Reaction Thermodynamics and Kinetics

The thermodynamics for dehydrogenation through theoretical monomeric intermediates was calculated (G3MP2) for **A–D**, **F–H**, and **J** (Table 18). A similar analysis was also performed for **A** and **J** through the intermediacy of the known trimeric products of initial BN dehydrogenation (Table 19).

Table 18. Calculated (G3MP2) thermodynamics for dehydrogenation of **A–D**, **F–H**, and **J** through monomeric species.

Reaction	ΔH_{298K} (kcal mol^{-1})	ΔG_{298K} (kcal mol^{-1})
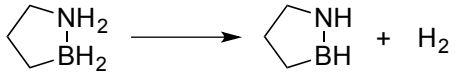 **A**	–7.0	–15.3
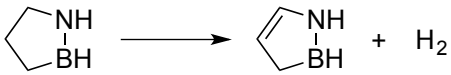	+23.1	+14.5
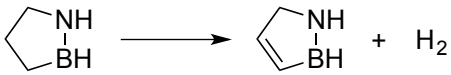	+22.5	+14.0
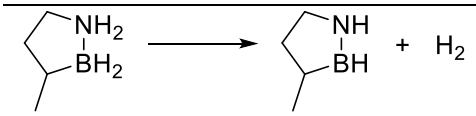 **B** **58**	–5.9	–14.3

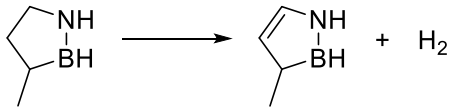

+24.0 +15.3

58

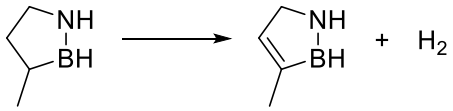

+19.6 +10.7

58

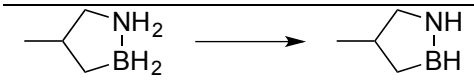

–6.7 –15.0

C

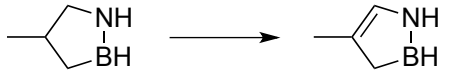

+20.6 +11.6

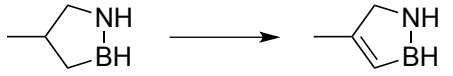

+22.2 +13.2

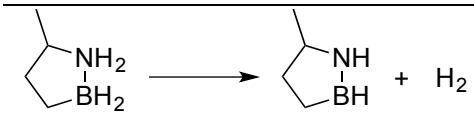

–7.1 –15.4

D

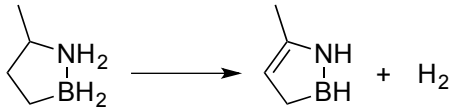

+23.4 +14.8

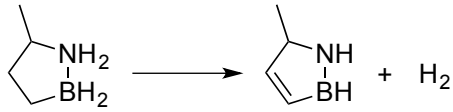

+21.9 +13.0

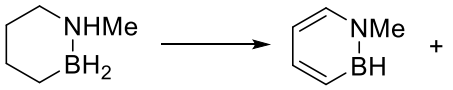

+26.0 –0.3

F

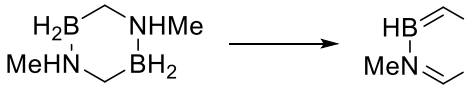

+30.9 +3.9

G

+28.4 +2.7

H

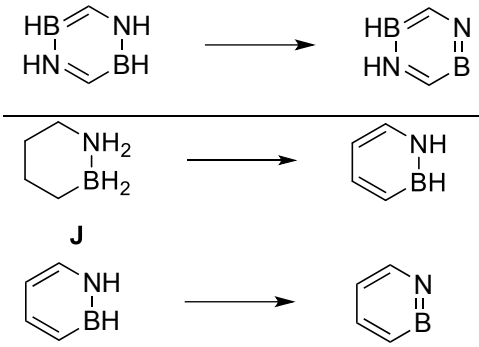

+ H_2	+50.4	+40.9
+ 3 H_2	+20.5	–5.3
+ H_2	+58.6	+49.8

J

Table 19. Calculated thermodynamics at 298 K for complete dehydrogenation of **A** and **J** through trimeric species. Values given are per unit trimer.

Reaction	ΔH_{gas} (kcal mol^{-1})	ΔH_{liq} (kcal mol^{-1})	ΔG_{gas} (kcal mol^{-1})	ΔG_{THF} (kcal mol^{-1})
3 **A** → + 6 H_2	–85.4	–61.0	–108.9	–87.6
→ + 3 H_2	+70.0	+70.3	+44.2	+46.0
→ + 3 H_2	+68.6	+68.3	+43.6	+44.8
3 **J** → **35** + 6 H_2	–83.1	–59.6	–107.3	–81.6
35 → + 6 H_2	+102.3	+102.8	+49.4	+75.0

A potential energy surface for the loss of two H_2 equivalents from a dimer of **B** (**59**) in the gas-phase was calculated using G3MP2 (Figure 47). The enthalpic component of the barrier to loss of the first equivalent was predicted to essentially consist of the endothermicity of the reaction. In contrast, the barrier to loss of the second equivalent included a sizeable endothermic component. The overall reaction is both significantly endothermic and endergonic (ΔH_{298K} = +43.9 kcal-mol^{-1}; ΔG_{298K} = +25.3 kcal-mol^{-1}).

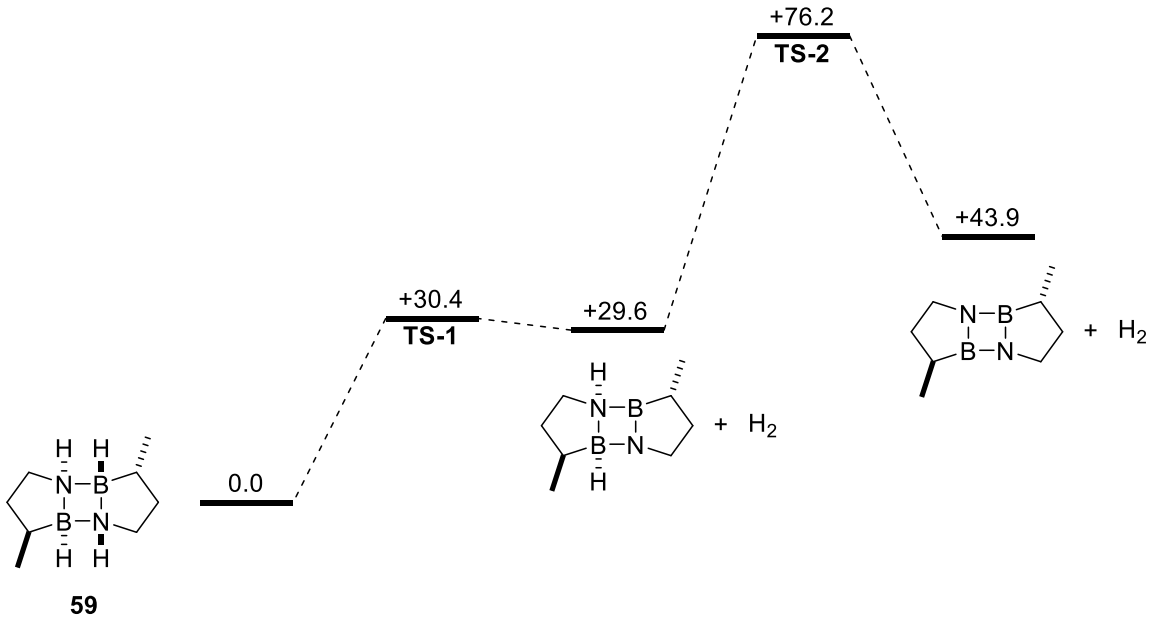

Figure 47. Potential energy surface for sequential loss of H_2 from dimer **59**. Gas-phase enthalpy values calculated using G3MP2 at 298 K.

While the alternative dissociation of **59** into two units of the monomeric species **58** was also calculated to be endothermic and endergonic (Scheme 26, top), the free energy of the reaction (ΔG_{298K} = +6.6 kcal-mol^{-1}) was considerably less than for loss of H_2 from **59**.[71] Thus, it was proposed that **58** first associates with **59** to form the saturated trimer **60**, which then decomposes to **61** with loss of three H_2 equivalents (Scheme 26, bottom). A potential energy surface for the sequential release of H_2 from **60** was calculated as before (Figure 48). The reaction enthalpies for the first two dehydrogenation steps are only very slightly endothermic; loss of the final equivalent to form the aromatic borazine core, however, renders this last step notably exothermic. The reaction overall is thus both exothermic and exergonic (ΔH_{298K} = –24.1 kcal-mol^{-1}; ΔG_{298K} = –51.6 kcal-mol^{-1}).

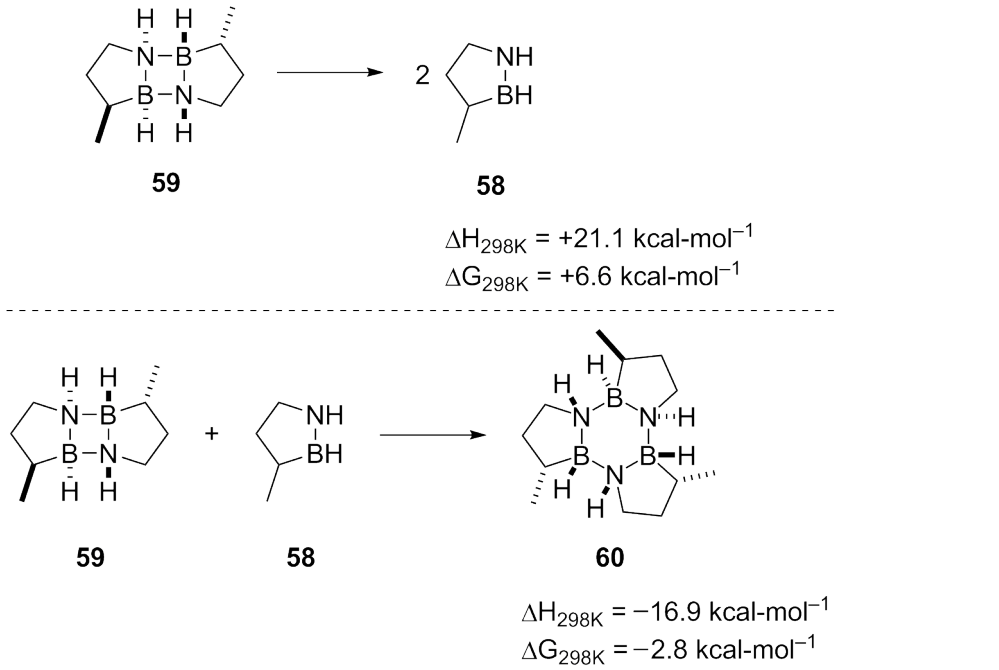

Scheme 26. Calculated (G3MP2) gas-phase thermodynamics for dissociation of dimer **59** (top), and for addition of **58** to **59** to form trimer **60**.

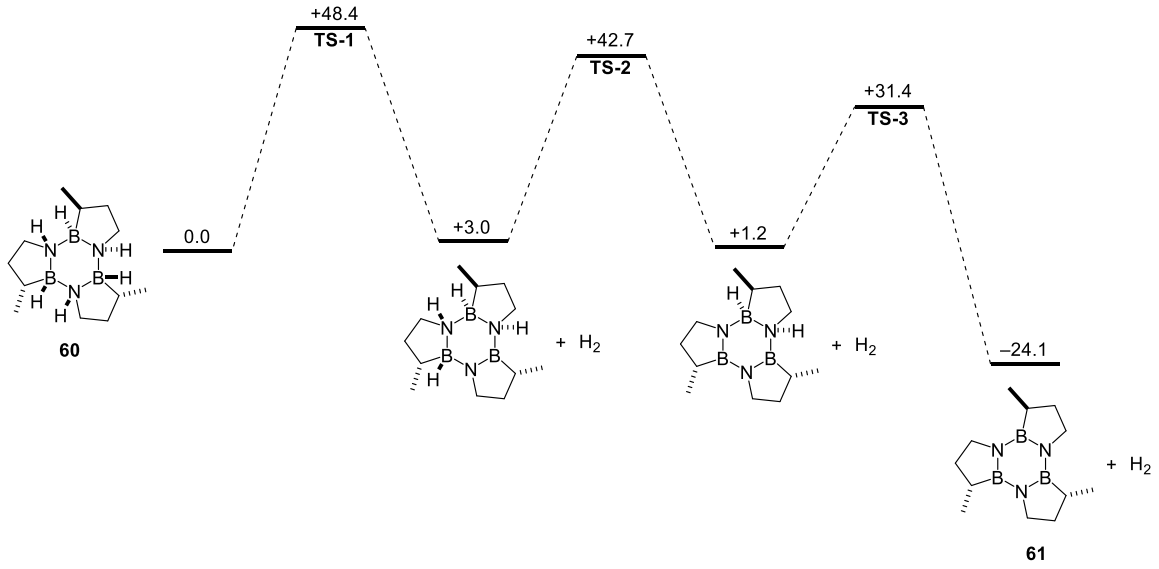

Figure 48. Potential energy surface for sequential loss of H_2 from trimer **60**. Gas-phase enthalpy values calculated using G3MP2 at 298 K.

It was hypothesized that fluorine substitution adjacent to boron in saturated five- and six-membered BN-heterocycles might favorably influence the thermodynamics of initial BN H_2 release. These effects were evaluated computationally (G3MP2) for a number of potential fluorinated materials (Table 20); boiling point predictions using COSMO-RS facilitated estimation of the liquid phase enthalpies. While neither mono- nor difluorination of **J** appeared to significantly affect the thermodynamics of the dehydrogenation reaction, more pronounced effects were indeed predicted for

mono-fluorination of **A–D**, with H_2 release becoming less exothermic and exergonic in the gas-phase and endothermic in the liquid phase.

Table 20. Calculated (G3MP2) thermodynamics of initial BN dehydrogenation of certain fluorinated materials and comparison to non-fluorinated equivalents.

Reaction	ΔH_{gas} (kcal mol^{-1})	ΔG_{gas} (kcal mol^{-1})	ΔH_{liq} (kcal mol^{-1})	T_{BP} react (K)	T_{BP} prod (K)
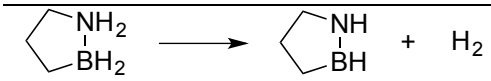 **A**	–7.0	–15.3	–0.8	465	215
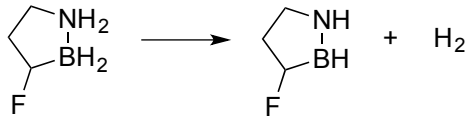	–0.7	–9.0	+5.4	591	348
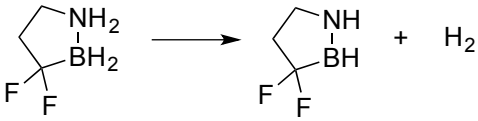	–1.6	–10.1	+4.6	680	432
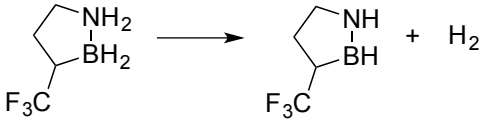	–2.7	–11.2	+1.5	548	379
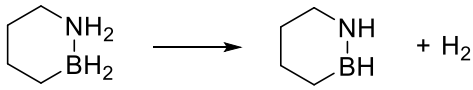 **J** **36**	–0.1	–9.0	+5.7	485	256
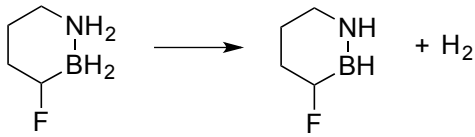	–0.4	–8.9	+4.4	529	339
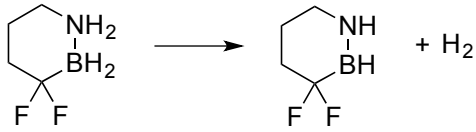	+0.5	–8.5	+6.7	635	386

For **B–D** and **J**, fluorination at the other carbon positions did not produce such pronounced effects (Table 21). Likewise, only small to moderate effects were induced by any form of dimethylation of **A** or methylation of **J** (Table 22).

Table 21. Calculated (G3MP2) thermodynamics of initial BN dehydrogenation of fluorinated derivatives of **B–D** and **J**.

Reaction	ΔH_{gas} (kcal mol^{-1})	ΔG_{gas} (kcal mol^{-1})
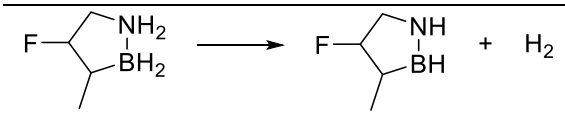	–4.7	–13.3
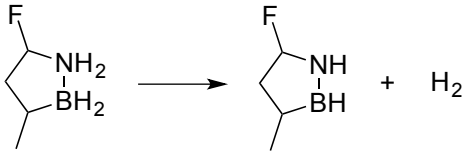	–9.9	–18.2
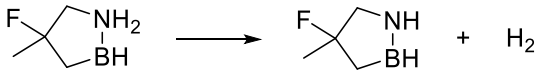	–5.1	–13.5
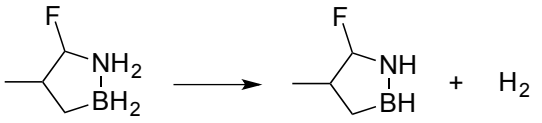	–9.8	–18.1
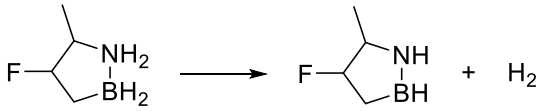	–6.6	–14.8
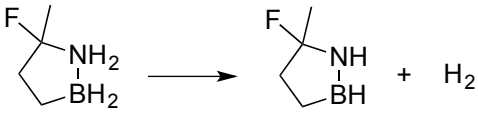	–8.3	–17.1
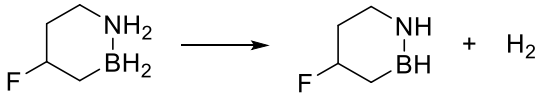	–6.0	–14.8
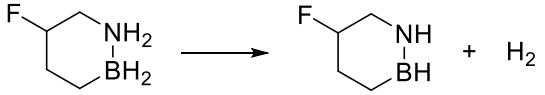	–7.7	–16.6
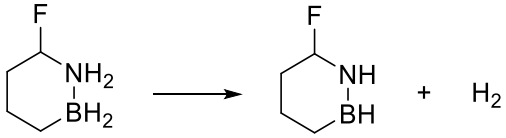	–7.6	–16.5

Table 22. Calculated (G3MP2) thermodynamics of initial BN dehydrogenation of dimethylated derivatives of **A** and mono-methylated derivatives of **J**.

Reaction	ΔH_{gas} (kcal mol^{-1})	ΔG_{gas} (kcal mol^{-1})
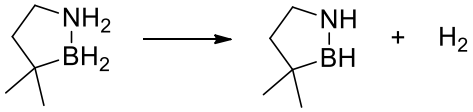	–6.1	–14.3
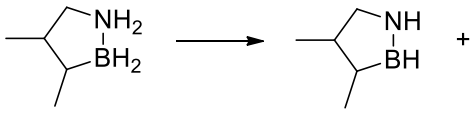	–6.2	–14.7
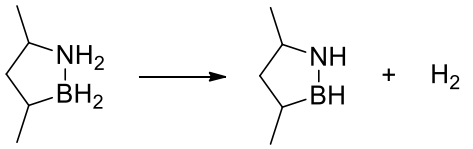	–6.2	–14.5
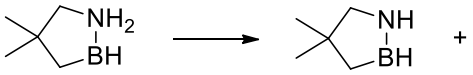	–6.6	–15.1
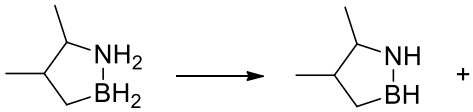	–6.9	–15.2
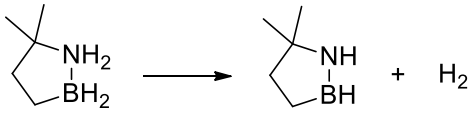	–6.9	–15.4
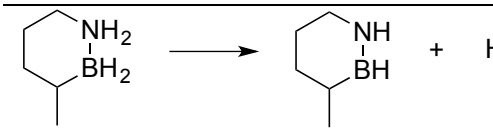	–6.3	–15.3
	–6.9	–15.7
	–7.0	–15.9
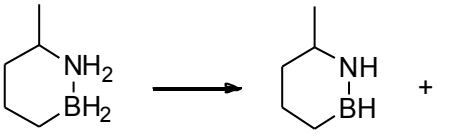	–7.0	–15.8

A spaghetti diagram for the complete dehydrogenation of $\mathbf{XH_2}$ from the di-equatorial conformer was calculated at 298 K using G3MP2 (Figure 49). Gas-phase enthalpy and

free energy values are shown for each step in Table 23.

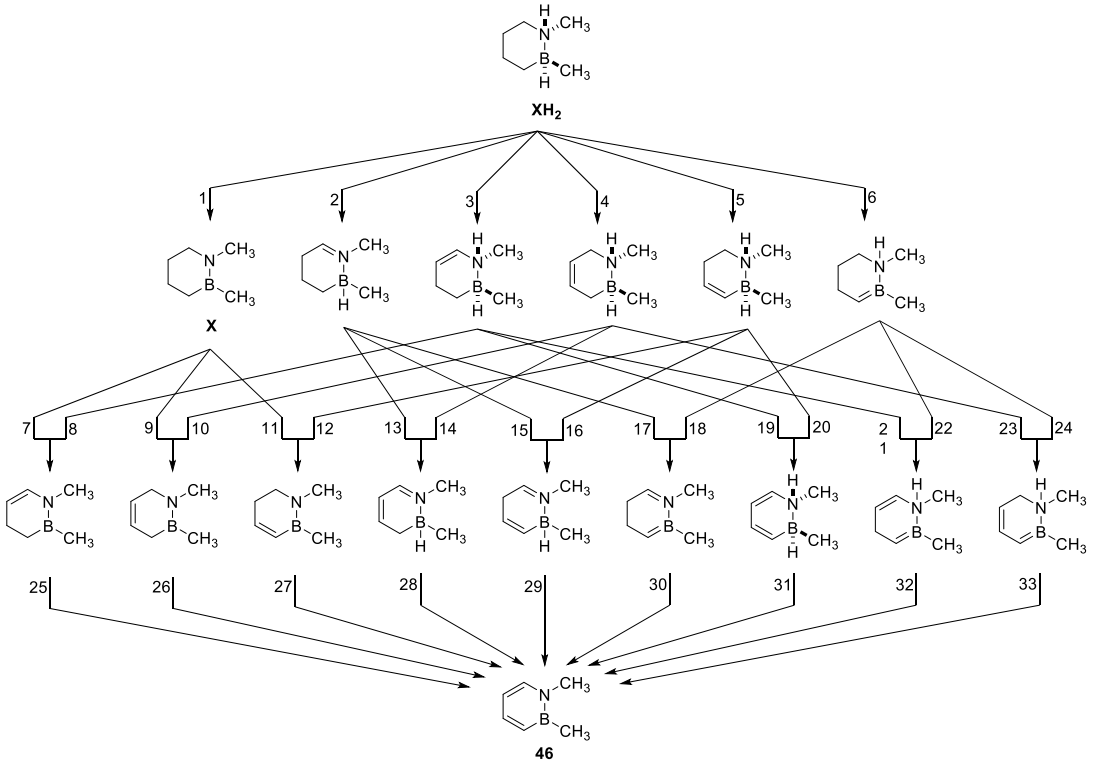

Figure 49. Spaghetti diagram for complete step-wise dehydrogenation of **XH_2**. Calculated energy values for each step are shown in Table V-K.

Table 23. Calculated (G3MP2) gas-phase enthalpy and free energy values for the complete step-wise dehydrogenation of **XH_2** shown in Figure 49.

Reaction #	ΔH_{298K} (kcal mol^{-1})	ΔG_{298K} (kcal mol^{-1})	Reaction #	ΔH_{298K} (kcal mol^{-1})	ΔG_{298K} (kcal mol^{-1})
1	–6.6	–15.9	18	+15.0	+6.0
2	+29.1	+20.0	19	+22.6	+13.7
3	+29.1	+20.0	20	+26.6	+17.5
4	+26.5	+17.6	21	+34.4	+25.5
5	+25.1	+16.2	22	+27.4	+18.2
6	+36.1	+27.4	23	+27.1	+18.6
7	+24.6	+15.4	24	+17.5	+8.8
8	–11.1	–20.6	25	+6.6	–1.7
9	+25.0	+16.1	26	+6.1	–2.4
10	–8.0	–17.4	27	+5.5	–3.1
11	+25.7	+16.8	28	–17.8	–26.8
12	–6.0	–15.3	29	–19.8	–28.4
13	+22.2	+13.4	30	–26.5	–35.7
14	+15.9	+6.9	31	–27.1	–36.0
15	+24.1	+15.0	32	–38.9	–47.8
16	+19.3	+9.9	33	–29.0	–38.4
17	+30.9	+22.3			

The thermodynamics for stepwise dehydrogenation of 3,5-dimethyl-1,4-BN-cyclohexane and proposed FLPs **52**−**54** are listed in Tables 24−27.

Table 24. Calculated (B3LYP/DZVP2) thermodynamics of stepwise dehydrogenation of 3,5-dimethyl-1,4-BN-cyclohexane.

Reaction	ΔH_{298K} (kcal mol^{-1})	ΔG_{298K} (kcal mol^{-1})
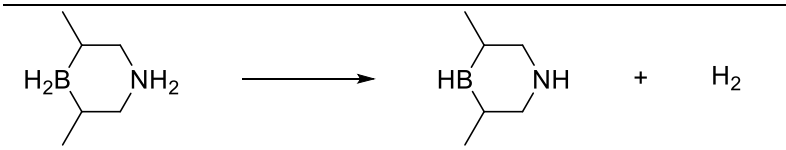	–9.3	–18.7
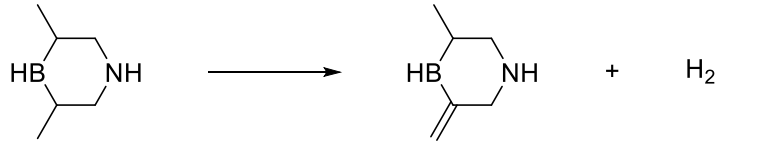	+25.8	+17.2
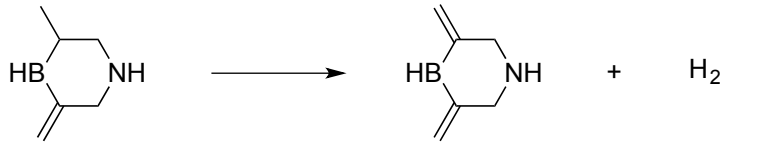	+25.6	–17.2
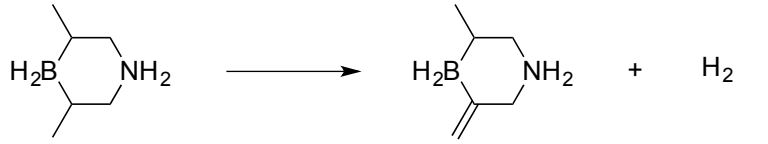	+26.6	+18.0
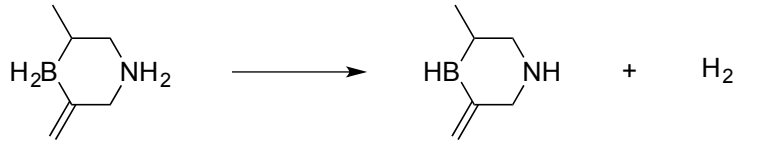	–10.4	–19.5
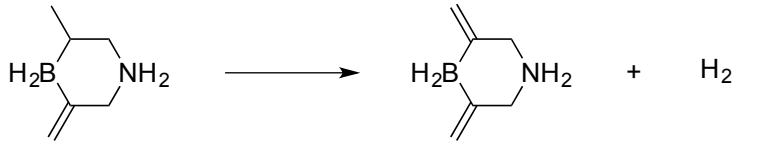	+27.0	+18.3
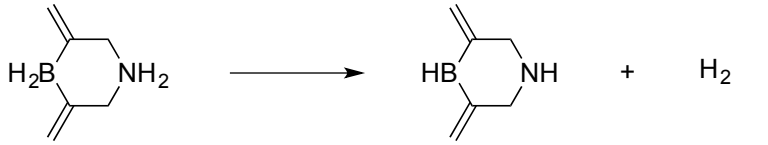	–11.5	–20.6

Table 25. Calculated (B3LYP/DZVP2) thermodynamics of stepwise dehydrogenation of **52**.

Reaction	ΔH_{298K} (kcal mol^{-1})	ΔG_{298K} (kcal mol^{-1})
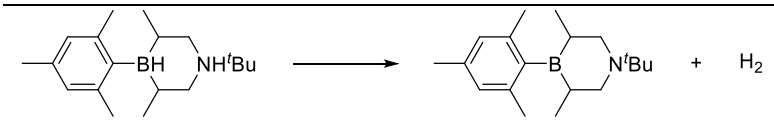 **52**	–11.0	–21.7
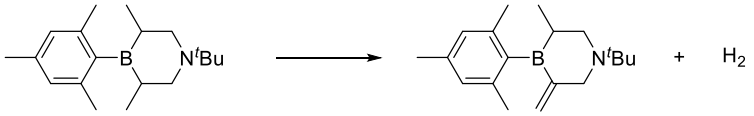	+25.1	+16.3
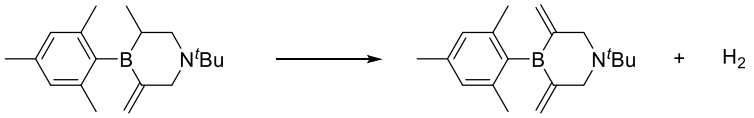	+24.8	+14.6
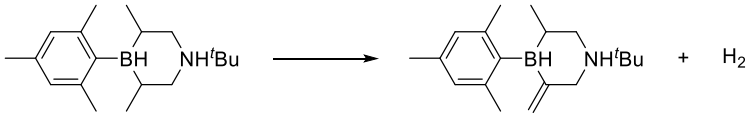 **52**	+25.1	+16.3
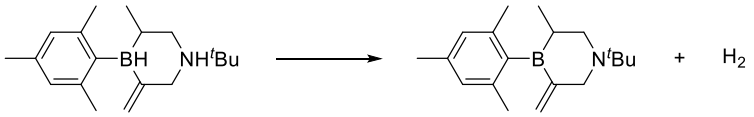	–11.0	–21.7
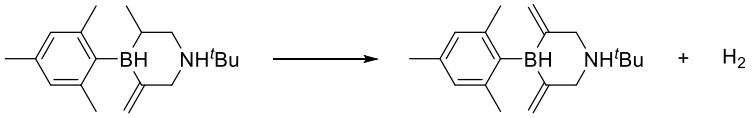	+26.0	+17.6
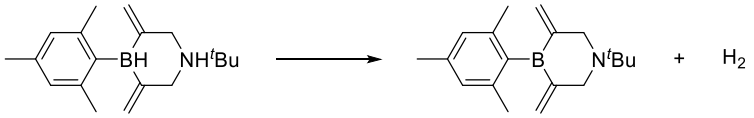	–12.2	–24.7

Table 26. Calculated (B3LYP/DZVP2) thermodynamics of stepwise dehydrogenation of **53**.

Reaction	ΔH_{298K} (kcal mol^{-1})	ΔG_{298K} (kcal mol^{-1})
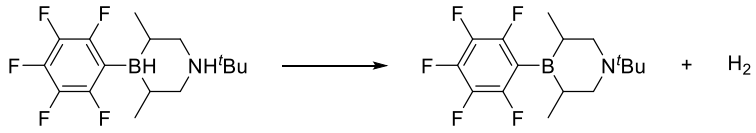 **53**	+2.9	–7.3
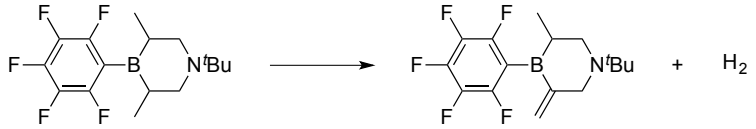	+25.9	+17.5
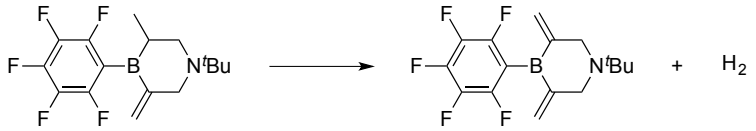	+25.9	+16.8
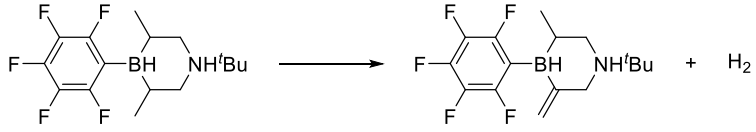 **53**	+27.2	+19.1
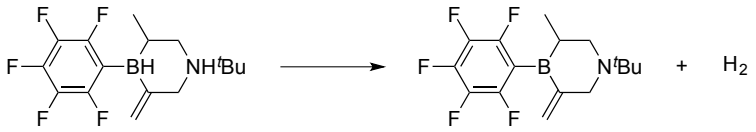	+1.6	–8.9
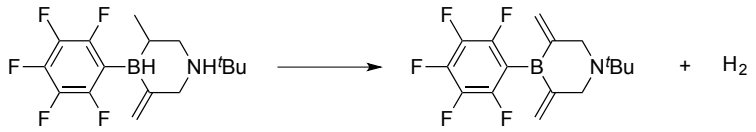	+27.6	+18.6
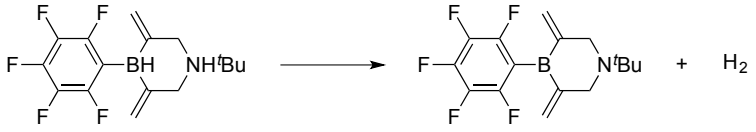	–0.1	–10.6

Table 27. Calculated (B3LYP/DZVP2) thermodynamics of stepwise dehydrogenation of **54**.

Reaction	ΔH_{298K} (kcal mol^{-1})	ΔG_{298K} (kcal mol^{-1})
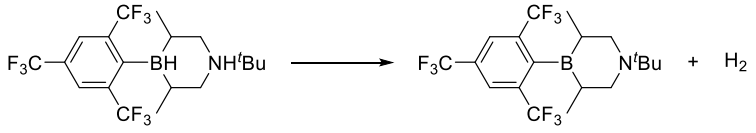 **54**	–5.4	–15.7

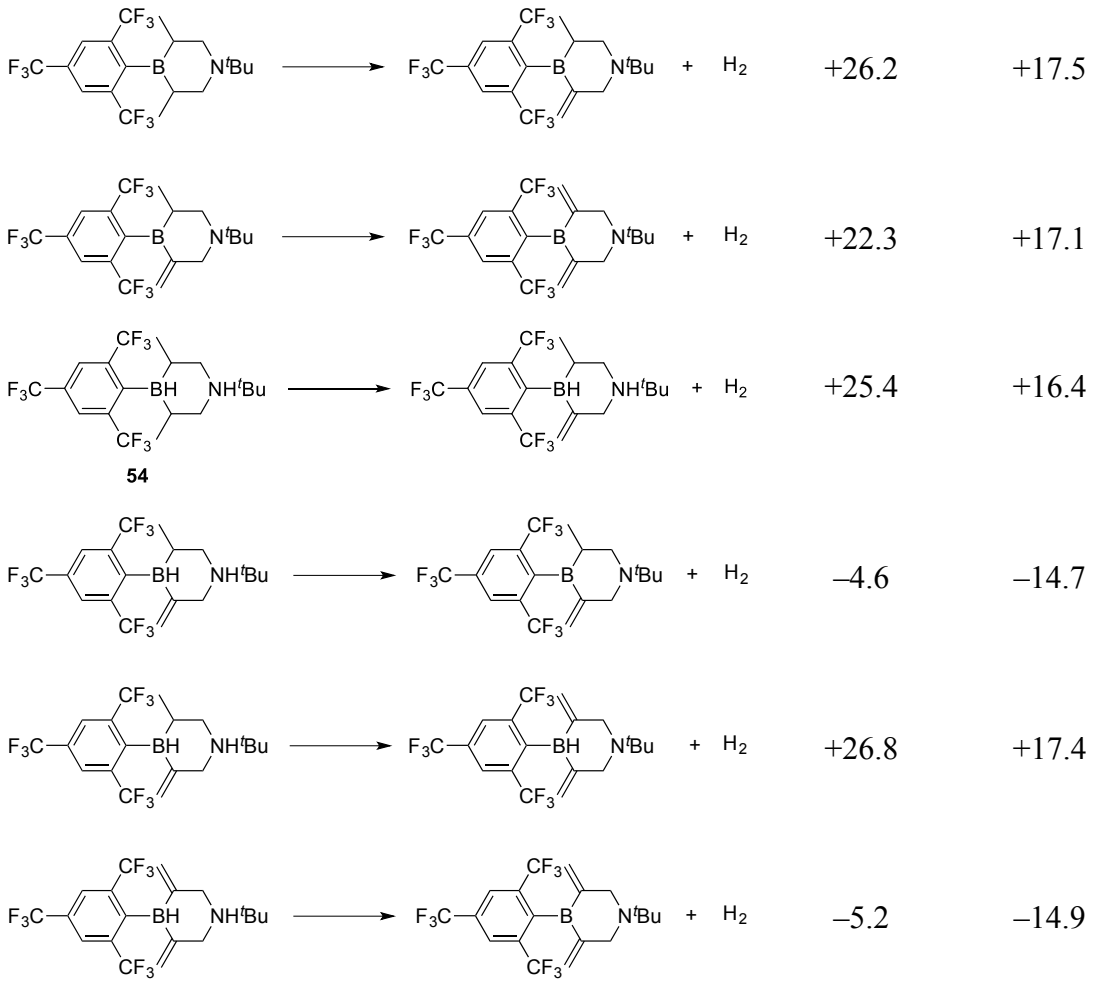

3.3. COMSOL Modeling − Exothermic-Endothermic Reaction Coupling

The presence of both -NH_2BH_2- and -CH_2CH_2- groups within the same molecule affords the opportunity to thermodynamically couple exothermic and endothermic H_2 release processes and thereby efficiently increase the effective H_2 weight capacity of the material. Successful harnessing of the heat generated from an exothermic reaction to simultaneously drive an endothermic one has been demonstrated for a number of multi-component systems.[72] Far less study, however, has been conducted for systems in which a single material undergoes both the exothermic and endothermic processes.[73]

For the purpose of our initial modeling efforts, 100% effective heat exchange and recuperation was assumed. It was also assumed that in a practical system a certain percentage of the H_2 produced could be burned to generate additional heat, and that 100% of this heat could be directed toward driving the endothermic dehydrogenation reaction. Based on these conditions, the maximum endothermicity (ΔH_{endo}) that would still allow for 90% onboard efficiency was calculated according to the following equation:

$$\Delta H_{endo} \le -\left(\frac{n_{H_2,exo}}{n_{H_2,endo}} \Delta H_{exo} + \frac{\Delta H_{comb}}{10} \left(1 + \frac{n_{H_2,exo}}{n_{H_2,endo}} \right) \right)$$

in which ΔH_{exo} is the heat of the exothermic dehydrogenation reaction, ΔH_{comb} is the heat of H_2 combustion, and n_{H_2} is the number of moles H_2 produced by either the exothermic or endothermic reaction. As shown in Figure 50 for a number of ratios of $n_{H_2,exo} : n_{H_2,endo}$, when supplemental heat is provided by partial combustion of H_2, it becomes feasible for the magnitude of ΔH_{endo} to exceed that of ΔH_{exo} and still achieve 90% onboard efficiency.

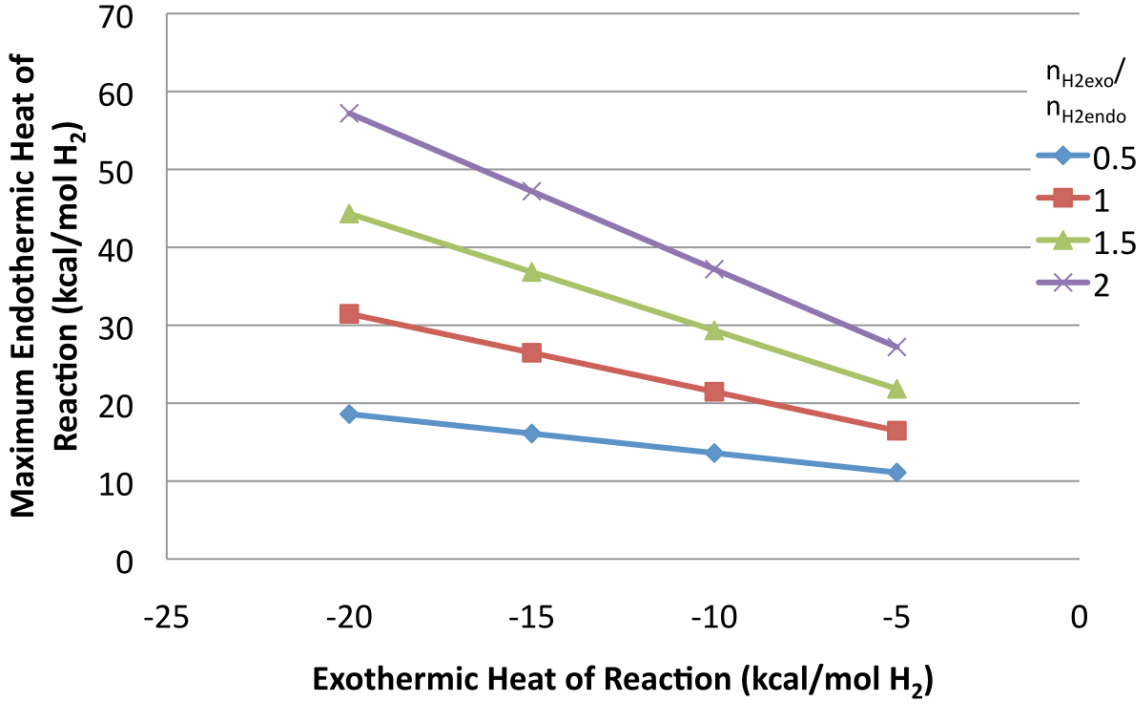

Figure 50. Maximum endothermic heat of reaction (ΔH_{endo}) to allow for 90% onboard efficiency with a given exothermic heat of reaction (ΔH_{exo}) at various molar ratios of H_2 produced from the separate dehydrogenation processes.

A one-dimensional model was developed for the sequential loss of three H_2 equivalents from **B** based on the following assumptions:

1. Tubular reactor; length = 160 cm, diameter = 40 cm
2. Substrate feed rate = 1.38 x 10^{-4} kg-s^{-1}
3. Inlet temperature = 140 ºC, pressure = 10 bar
4. 1st and 2nd H_2 equivalents from exothermic reactions with kinetic parameters from Figure 10
5. 3rd H_2 equivalent from endothermic reaction with first-order kinetics based on Pd/C-catalyzed cyclohexane dehydrogenation

Based on the concentration profiles shown in Figure 51, this model predicted a total

release of 2.6 H_2 equivalents. Additionally, the initial maximum reactor temperature (T_{max}) was predicted to be 300 ºC, but this value decreases to ~200 ºC when the endothermic reaction comes into play. Using the same systems parameters as above in COMSOL, this analysis was extended to a two-dimensional axisymmetric model; as shown in Figure 52, component velocities increase down the reactor length, rendering complete conversion difficult to attain.

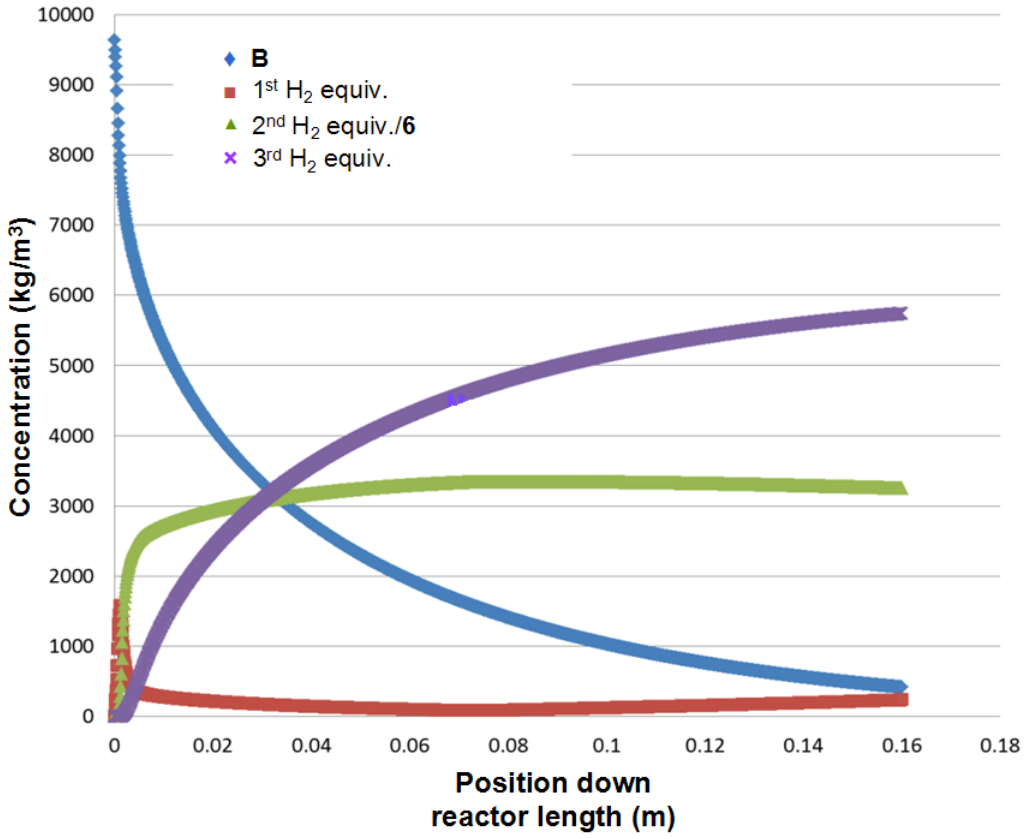

Figure 51. Predicted concentration profiles for **B**, **6**, and H_2 equivalents along a one-dimensional model flow reactor for coupled exothermic-endothermic reactions.

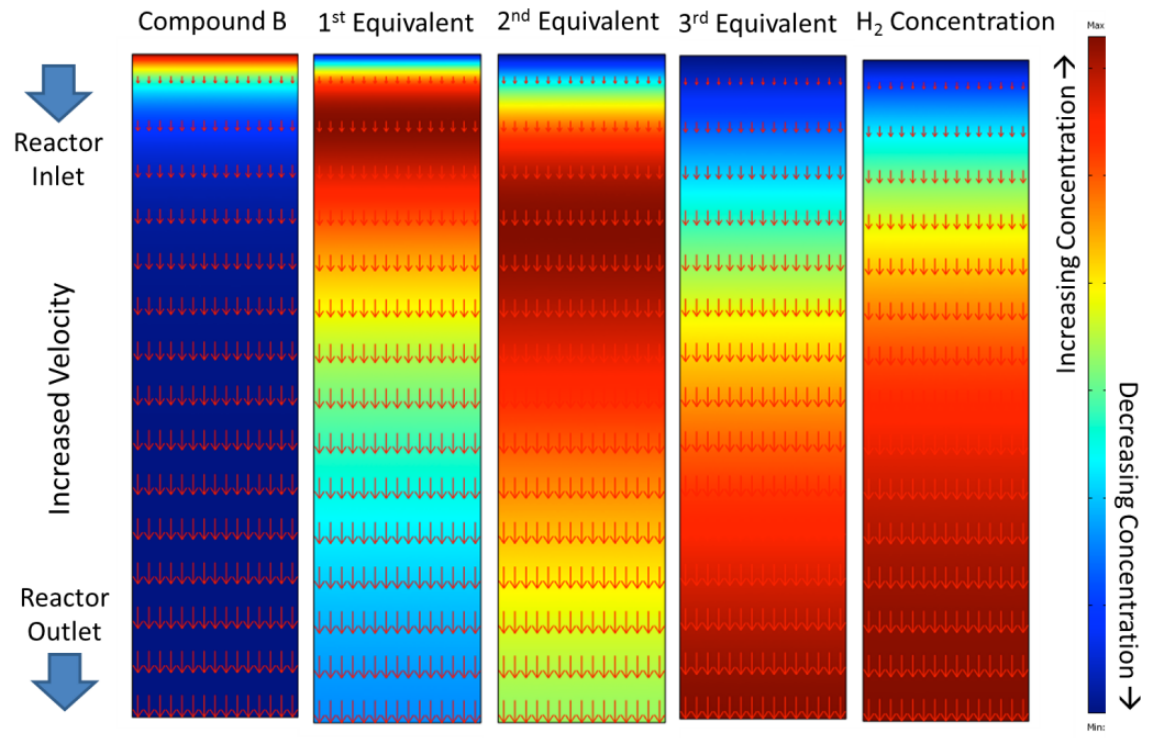

Figure 52. COMSOL-modeled concentration profiles of **B** and H_2 equivalents in a two-dimensional, axisymmetric reactor; red arrows represent component velocity vectors.

Various system parameters were adjusted to determine their influence on H_2 yield and T_{max} (Table 28). Notably, only raising the inlet temperature resulted in a higher H_2 yield *and* a lower T_{max}; all other changes that produced a higher yield also raised the T_{max}.

Table 28. Influence of system parameters on H_2 yield and maximum reactor temperature (T_{max}) for a one-dimensional model of coupled exothermic-endothermic reactions.

Adjusted parameter	Change in H_2 yield	Change in T_{max}
increased reactor length	+	+
addition of inert diluent	–	–
increased inlet temperature	+	–
increased exothermicity	+	+
increased endothermicity	–	–
increased endothermic reaction rate	no change	–
decreased endothermic E_a	+	+

A different one-dimensional model was developed to investigate the relationship between reaction temperature and conversion and different relative rates of coupled exothermic and endothermic reactions; this model assumed an adiabatic stirred batch reactor at an initial temperature of 160 ºC and a theoretical material with the properties listed in Table 29. As shown in Figure 53, if the exothermic reaction proceeds at 100x the rate of a coupled endothermic reaction, the reactor temperature will rapidly increase to 335 ºC. Under adiabatic conditions, however, the additional heat produced will drive the

endothermic reaction to 56% conversion, resulting in a gradual decrease in temperature back down to ~185 ºC. Notably, if the reactions were not coupled, the endothermic reaction would only proceed to 4% conversion, and the reactor temperature would decrease by only 4 ºC, again from a maximum of 335 ºC.

Table 29. Assumed properties of the theoretical material used to model reaction temperature and conversion as shown in Figure 53.

Parameter	Value
C	+54 cal-mol^{-1}-K^{-1}
ΔH_{exo}	–9.9 kcal-mol^{-1}
ΔH_{endo}	+17 kcal-mol^{-1}
$E_{a,exo}$	+18.6 kcal-mol^{-1}
$E_{a,exo}$	+18.6 kcal-mol^{-1}
A_{exo}	3.6 x 10^{7} s^{-1}

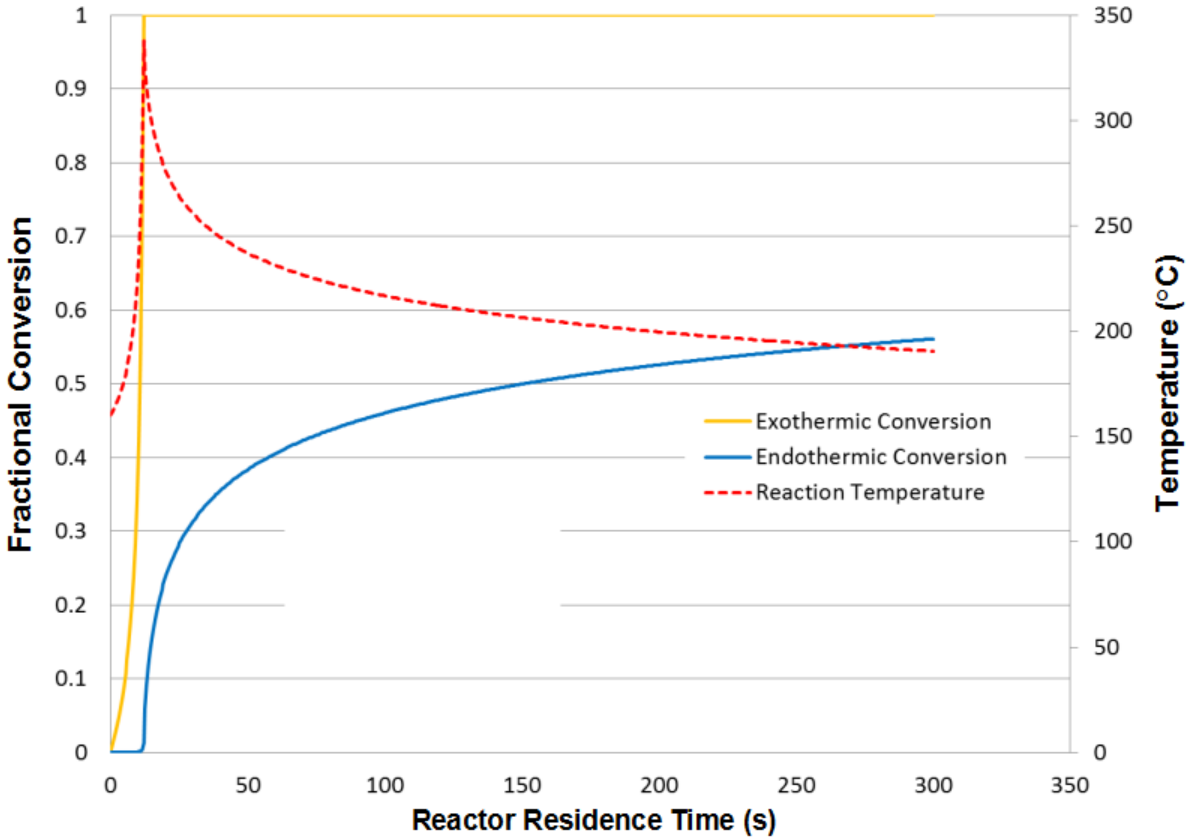

Figure 53. Predicted reaction temperature and conversion profiles for coupled exothermic-endothermic reactions with a relative rate ratio of 100:1.

If the exothermic reaction were just 10x faster than the endothermic reaction, the reactor temperature would initially increase by 133 ºC, and the endothermic reaction would proceed to 71% conversion (and 85% with 5% H_2 combustion assuming 75% combustion efficiency). Again, these gains are greatly diminished if the two reactions are not coupled: endothermic conversion drops to 13% even with H_2 combustion and the

maximum reactor temperature rises to 345 ºC.

This analysis was again extended to a two-dimensional, axisymmetric model using COMSOL. Axial and radial conduction and heat loss to the environment were also included in the model; component acceleration due to production of H_2 gas was ignored. Both reactant and product were assumed to remain in a liquid state within a plug flow reactor with an aspect ratio of 10:1 (*l*:d) and an initial temperature of 160 ºC. As before, reaction conversion and temperature were predicted for a theoretical material with properties based on those determined for various BN compounds (Figure 54). The temperature was predicted to initially increase by 67.5 ºC, and the endothermic reaction proceeded in 66% conversion.

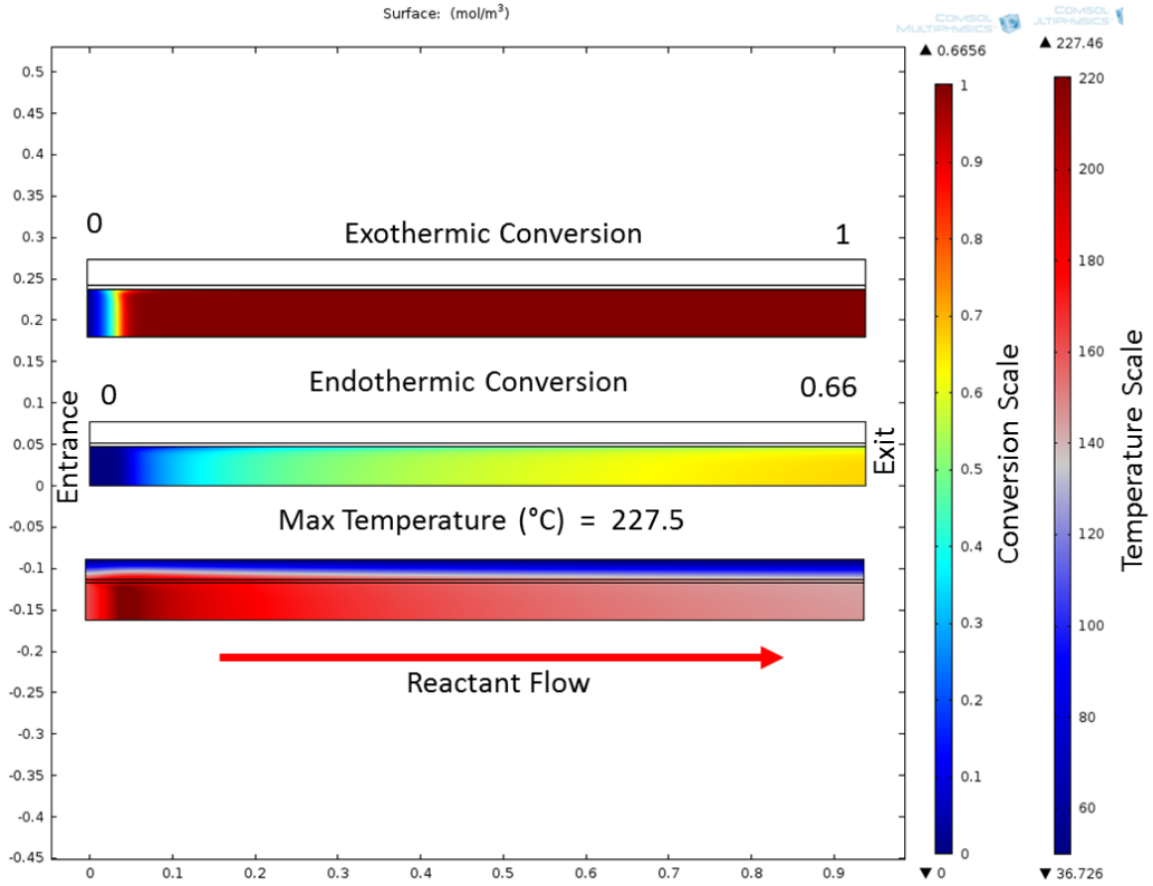

Figure 54. COMSOL-modeled reaction temperature and conversion profiles for a two-dimensional, axisymmetric reactor for a coupled exothermic-endothermic reaction system.

Various system parameters for this model were adjusted to determine their effects on endothermic reaction conversion. As shown in Figure 55, this conversion is typically maximized when the rates of exothermic and endothermic reactions of a given ΔH_{exo}:ΔH_{endo} ratio are approximately equal (r_{exo}:$r_{endo} \approx 1$). As expected, the globally highest conversion is achieved when ΔH_{exo}:ΔH_{endo} is closest to 1. When ΔH_{exo}:ΔH_{endo} is significantly <1, endothermic conversion decreases as r_{exo}:r_{endo} also becomes increasingly <1. Notably, under these conditions, the coupled exothermic reaction also fails to reach 100% conversion.

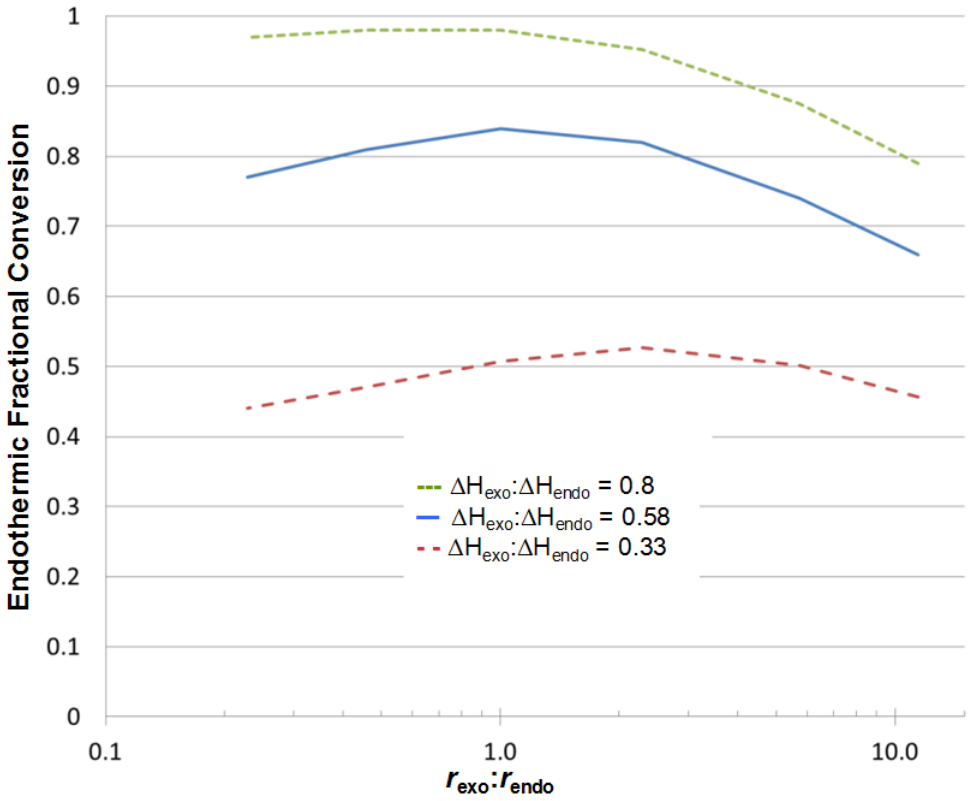

Figure 55. Predicted endothermic conversions for different ratios of rates (r) and enthalpies (ΔH) of a coupled exothermic-endothermic reaction system.

The scale of the reactor was also found to have an effect on endothermic conversion (Figure 56). Specifically, higher conversion was predicted for a larger reactor, presumably as a result of reduced heat loss to the environment. Providing additional heat through 5% H_2 combustion (70% combustion efficiency) also improved endothermic conversion to >90% even for certain cases in which ΔH_{exo}:ΔH_{endo}<1 and r_{exo}:r_{endo}>>1 (Figure 57).

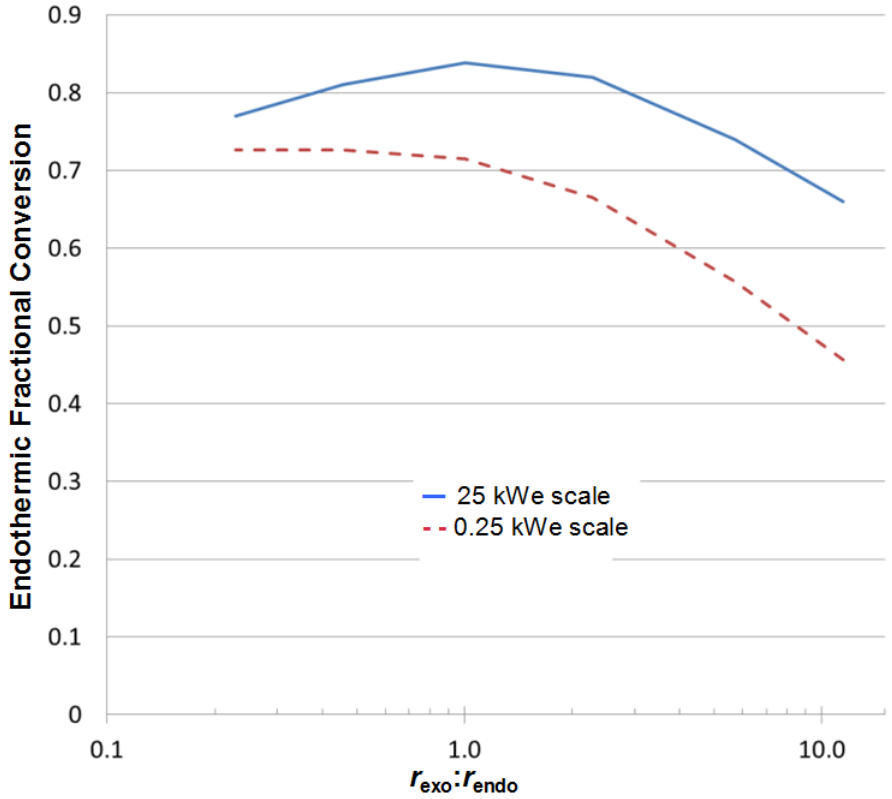

Figure 56. Predicted endothermic conversions for different ratios of rates (*r*) and of a coupled exothermic-endothermic reaction system in a reactor capable of supplying 25 kWe (blue) or 0.25 kWe (red) of power based on a hydrogen-to-electricity conversion rate of 0.02 g H_2-s^{-1}-kWe^{-1}.

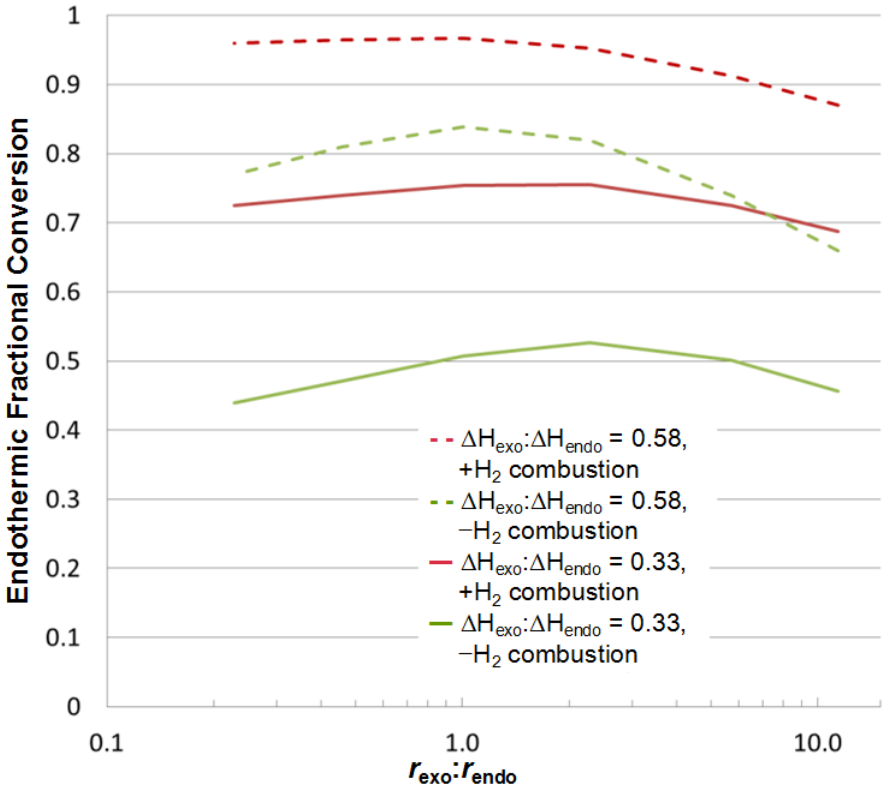

Figure 57. Predicted endothermic conversions for different ratios of rates (*r*) and enthalpies (ΔH) of a coupled exothermic-endothermic reaction system with (red) and without (green) 5% H_2 combustion (70% combustion efficiency).

In an effort to improve the accuracy of the COMSOL modeling discussed above, the kinetic parameters of the exothermic reaction were assumed to match those experimentally determined for Pd/C-catalyzed BN dehydrogenation of **J** (Figure 35); likewise, those of the endothermic reaction were assumed to be the same as determined for catalyzed CC dehydrogenation of **X** (Table 10). The reactor for this model was scaled to be capable of supplying 43 kWe. As shown in Figure 58, with an initial temperature of 160 ºC, 100% of the exothermic reaction and 39% of the endothermic reaction were predicted to occur within the first 4% of the reactor's length. With coupling between the two processes, T_{max} was predicted to reach 292 ºC (Table 30, entry 3); as expected, this value increased substantially in the case of an exothermic-only system and likewise decreased for an endothermic-only system.

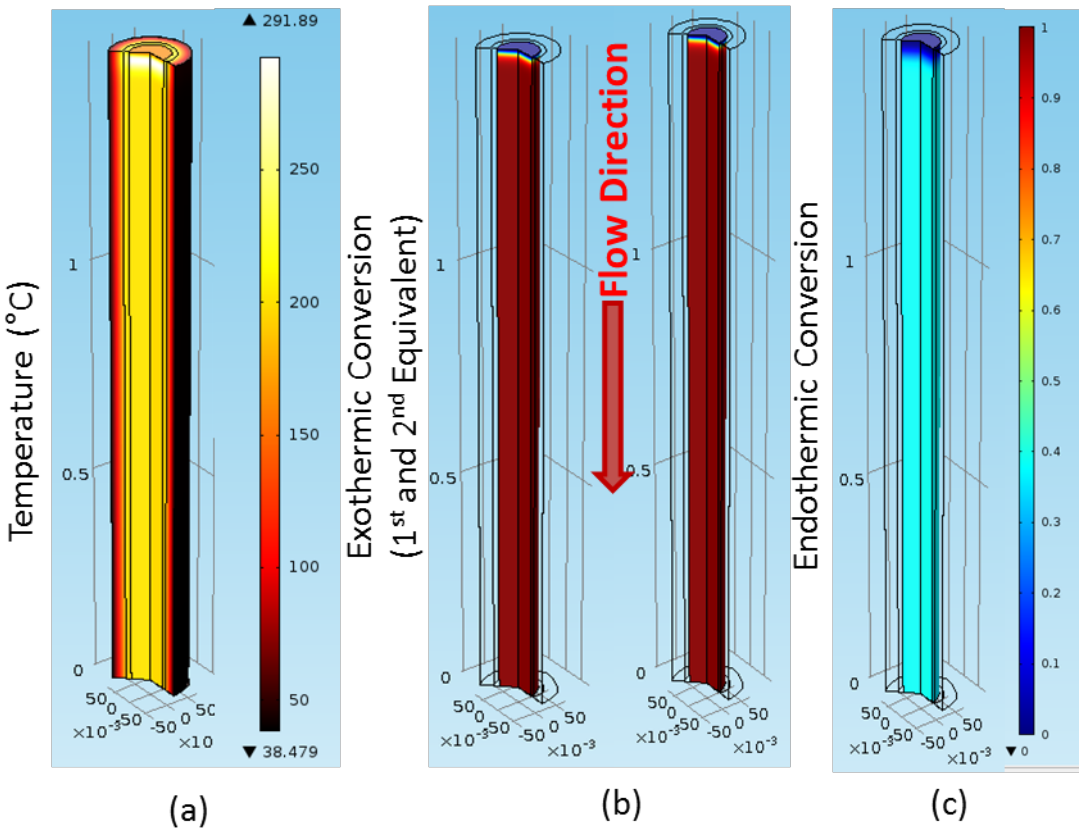

Figure 58. COMSOL-predicted reaction temperature (a), exothermic conversion (b), and endothermic conversion (c) in a two-dimensional, axisymmetric reactor for a theoretical single material featuring exothermic and endothermic Pd/C-dehydrogenation kinetics based on those experimentally determined for **J** and **X**, respectively.

Table 30. Predicted reaction conversions and maximum reactor temperature (T_{max}) for uncoupled and coupled exothermic-endothermic reaction systems with the parameters used for the model in Figure 58.

Active reaction	Exothermic Conversion	Endothermic Conversion	T_{max}
Exothermic only	100%	–	364 ºC
Endothermic only	–	5.6%	160 ºC
Exothermic+Endothermic	100%	39%	292 ºC
Exothermic+Endothermic w/o equilibrium constraints	100%	74%	292 ºC

The endothermic CC dehydrogenation process was assumed to be appreciably reversible under practical reaction conditions, with the extent of effective conversion governed by a set of equilibrium parameters. When these constraints were removed from the analysis, endothermic conversion in the coupled system nearly doubled to 74% (Table 30, entry 4).

4. Conclusions

Successful large-scale (decagram) synthesis of **B** allowed for testing of the material in powering a real PEM fuel cell stack; hydrogen produced from catalyzed decomposition of **B** proved equally effective in this regard as facility hydrogen. Additionally, a blend of compound **B** and ammonia borane afforded a hydrogen storage material that remained fluid over the entirety of its fuel cycle. The presence of **B** also appeared to reduce the formation of borazine from the decomposition of the AB component, thereby dramatically improving the purity of the blend's H_2 stream compared to that from the decomposition of AB alone.

Dehydrogenation of the carbonaceous components of a model CBN cyclohexene-type substrate was achieved in the gas phase using Pd/C as a catalyst. Generalization of this result to render it applicable to actual CBN hydrogen storage target materials, however, currently remains an unmet challenge. Using a combination of experimentally and computationally derived parameters, COMSOL modeling did indeed predict the thermodynamic coupling of exothermic BN and endothermic CC dehydrogenation could improve the overall system performance. The magnitude of these benefits, however, was revealed to be closely linked to both the relative rates of the two processes and the equilibrium constant associated with the endothermic reaction.

Compound **H** was successfully developed as a long-term storage material of exceptionally high thermal stability. Release of two H_2 equivalents per substrate was achieved using either Pd/C or homogeneous Ru catalyst. Further dehydrogenation of **H** was apparently impeded by the formation of dimeric cage-type compounds under these conditions.

The persistent formation of dimeric intermediates with *B*,*N*-substituted derivatives of **E** prevented the realization of this CBN system as a directly reversible hydrogen storage material. While several monomeric, 1,4-BN-heterocyclic compounds were successfully synthesized, none definitively demonstrated the capacity to activate H_2. The state of the art for regeneration of spent CBN fuels thus remains a two step protocol involving reduction by $LiAlH_4$ or BH_3•THF. Addressing this outstanding issue of achieving readily reversible CBN dehydrogenation should serve as a central objective of any future work conducted on these materials.

5. List of Publications that acknowledge DOE-EERE support:

1) Matus, M.; Liu, S.-Y.; Dixon, D. A. "Dehydrogenation Reactions of Cyclic $C_2B_2N_2H_{12}$ and C_4BNH_{12} Isomers" *J. Phys. Chem. A* **2010**, *114*, 2644-2654. [10.1021/jp9102838]

2) Campbell, P. G.; Zakharov, L. N.; Grant, D.; Dixon, D. A.; Liu, S.-Y. "Hydrogen Storage by Boron-Nitrogen Heterocycles: A Simple Route for Spent Fuel Regeneration" *J. Am. Chem. Soc.* **2010**, *132*, 3289-3291. [10.1021/ja9106622]

3) Daly, A. M.; Tanjaroon, C.; Marwitz, A. J. V.; Liu, S.-Y.; Kukolich S. G. "Microwave Spectrum, Structural Parameters, and Quadrupole Coupling for 1,2-Dihydro-1,2-azaborine" *J. Am. Chem. Soc.* **2010**, *132*, 5501-5506. [10.1021/ja1005338]

4) Campbell, P. G.; Abbey, E. R.; Neiner, D.; Grant, D. J.; Dixon, D. A.; Liu, S.-Y. "Resonance Stabilization Energy of 1,2-Azaborines: A Quantitative Experimental Study by Reaction Calorimetry" *J. Am. Chem. Soc.* **2010**, *132*, 18048-18050. [10.1021/ja109596m]

5) Luo, W.; Zakharov, L. N.; Liu, S.-Y. "1,2-BN Cyclohexane: Synthesis, Structure, Dynamics, and Reactivity" *J. Am. Chem. Soc.* **2011**, *133*, 13006-13009. [10.1021/ja206497x]

6) Marwitz, A. J. V.; Lamm, A. N.; Zakharov, L. N.; Vasiliu, M.; Dixon, D. A.; Liu, S.-Y. "BN-substituted diphenylacetylene: a basic model for conjugated pi-systems containing the BN bond pair" *Chem. Sci.* **2012**, *3*, 825-829. [10.1039/C1SC00500F]

7) Luo, W.; Campbell, P. G.; Zakharov, L. N.; Liu, S.-Y. "A Single-Component Liquid-Phase Hydrogen Storage Material" *J. Am. Chem. Soc.* **2011**, *133*, 19326-19329. [10.1021/ja208834v].

* Highlighted in:
Chemical & Engineering News (C&EN) (2011, November 28, page 35)
Nature Chemistry **2012**, *4*, 5 -
Nature Climate Change **2012**, *2*, 23

8) Campbell, P. G.; Marwitz, A. J. V.; Liu, S.-Y. "Recent Advances in Azaborine Chemistry" *Angew. Chem. Int. Ed.* **2012**, *51*, 6074-6092. [10.1002/anie.201200063]

9) Luo, W.; Neiner, D.; Karkamkar, A.; Parab, K.; Garner, E. B.; Dixon, D. A.; Matson, D.; Autrey, T.; Liu, S.-Y. "3-Methyl-1,2-BN-cyclopentane: a promising H_2 storage material?" *Dalton Trans.* **2013**, *42*, 611-614. [10.1039/C2DT31617J]

10) Campbell, P. G.; Ishibashi, J. S. A.; Zakharov, L. N.; Liu, S.-Y. "B-Methyl Amine Borane Derivatives: Synthesis, Characterization and Hydrogen Release" *Aust. J. Chem.* **2014**, *67*, 521-524. [10.1071/CH13198]

11) Chen, G.; Zakharov, L. N.; Bowden, M. E.; Karkamkar, A. J.; Whittemore, S. E.; Garner, E. B, III.; Mikulas, T. C.; Dixon, D. A.; Autrey, T.; Liu, S.-Y. "Bis-BN Cyclohexane: A Remarkably Kinetically Stable Chemical Hydrogen Storage Material" *J. Am. Chem. Soc.* **2015**, *137*, 134-137. [10.1021/ja511766p]

* Highlighted in:
C&EN online - [link]
JACS Spotlights (*J. Am. Chem. Soc.* **2015**, *137*, 551-552.) - [link]

12) Kukolich, S. G.; Sun, M.; Daly, A. M.; Luo, W.; Zakharov, L. N.; Liu, S.-Y. "Identification and Characterization of 1,2-BN Cyclohexene Using Microwave Spectroscopy" *Chem. Phys. Lett.* **2015**, *639*, 88-92. [10.1016/j.cplett.2015.09.009]

13) Kumar, A.; Ishibashi, J. S. A.; Hooper, T. N.; Mikulas, T. C.; Dixon, D. A.; Liu, S.-Y.; Weller, A. S. "The Synthesis, Characterization and Dehydrogenation of Sigma-Complexes of BN-Cyclohexanes" *Chem. Eur. J.* **2016**, *22*, 310-322. [10.1002/chem.201502986]

14) Giustra, Z. X.; Ishibashi, J. S. A.; Liu, S.-Y. "Homogeneous Metal Catalysis for Conversion Between Aromatic and Saturated Compounds" *Coord. Chem. Rev.* **2016**, *314*, 134-181. [10.1016/j.ccr.2015.11.006]

15) Whittemore, S. M.; Bowden, M.; Karkamkar, A.; Parab K.; Neiner, D.; Autrey T.; Ishibashi, J. S. A.; Chen, G.; Liu, S.-Y.; Dixon, D. A. "Blending Materials Composed of Boron, Nitrogen and Carbon to Transform Approaches to Liquid Hydrogen Stores" *Dalton Trans.* **2016**, *45*, 6196-6203. [10.1039/c5dt04276c]

16) Brooks, K. P.; Bowden, M. E.; Karkamkar, A. J.; Houghton, A. Y.; Autrey, S. T., Coupling of exothermic and endothermic hydrogen storage materials. *J. Power Sources* **2016,** *324*, 170-178.

17) Giustra, Z. X.; Chou, L.-Y.; Tsung, C.-K.; Liu, S.-Y. "Kinetics of $-CH_2CH_2-$ Hydrogen Release from a BN-cyclohexene Derivative" *Organometallics* **2016**, *35*, ASAP. [10.1021/acs.organomet.6b00412]

6. References and Notes

(1) a) Veziroğlu, T. N.; Şahin, S. *Energy Convers. Manag.* **2008,** *49,* 1820–1831. b) Pudukudy, M.; Yaakob, Z.; Mohammad, M.; Narayanan, B.; Sopian, K. *Renewable Sustainable Energy Rev.* **2014,** *30,* 743–757. c) International Energy Agency. Technology Roadmap: Hydrogen and Fuel Cells, 2015. http://www.iea.org/publications/freepublications/publication/TechnologyRoadmapHydrogenandFuelCells.pdf (accessed October 6, 2015). d) Elmer, T.; Worall, M.; Wu, S.; Riffat, S. B. *Renewable Sustainable Energy Rev.* **2015,** *42,* 913–931. e) Ellamla, H. R.; Staffell, I.; Bujlo, P.; Pollet, B. G.; Pasupathi, S. *J. Power Sources* **2015,** *293,* 312–328. f) Sharma, S.; Ghoshal, S. K. *Renewable Sustainable Energy Rev.* **2015,** *43,* 1151–1158. g) Singh, S.; Jain, S.; Venkateswaran, P. S.; Tiwari, A. K.; Nouni, M. R.; Pandey, J. K.; Goel, S. *Renewable Sustainable Energy Rev.* **2015,** *51,* 623–633.

(2) a) HyWays. The European Hydrogen Roadmap, 2008. http://www.hyways.de/docs/Brochures_and_Flyers/HyWays_Roadmap_FINAL_22FEB2008.pdf (accessed October 6, 2015). b) Fuel Cells and Hydrogen Joint Undertaking. A portfolio of power-trains for Europe: a fact-based analysis, 2010. http://www.fch.europa.eu/sites/default/files/documents/Power_trains_for_Europe.pdf. (accessed October 6, 2015). c) National Petroleum Council. Advancing technology for American's transportation future, Chapter 15: Hydrogen, 2012. http://www.npc.org/reports/FTF-report-080112/Chapter_15-Hydrogen.pdf. (accessed October 6, 2015).

(3) a) Hua, T.; Ahluwalia, R.; Eudy, L.; Singer, G.; Jermer, B.; Asselin-Miller, N.; Wessel, S.; Patterson, T.; Marcinkoski, J. *J. Power Sources* **2014,** *269,* 975–993. b) Ball, M.; Weeda, M. *Int. J. Hydrogen Energy* **2015,** *40,* 7903–7919.

(4) For a comprehensive review of PEM and other fuel cell types, see Sharaf, O. Z.; Orhan, M. F. *Renewable Sustainable Energy Rev.* **2014,** ***32,*** 810–853.

(5) a) Jorgensen, S. W. *Curr. Opin. Solid State Mater. Sci.* **2011,** ***15,*** 39–43. b) Durbin, D. J.; Malardier-Jugroot, C. *Int. J. Hydrogen Storage* **2013,** *38,* 14595–14617.

(6) For the most up-to-date target values, see: US Drive. Target Explanation Document: Onboard Hydrogen Storage for Light-Duty Fuel Cell Vehicles. US Department of Energy, 2015. http://energy.gov/sites/prod/files/2015/05/f22/fcto_targets_onboard_hydro_storage_explanation.pdf (accessed October 6, 2015).

(7) Hua, T. Q.; Ahluwalia, R. K.; Peng, J. K.; Kromer, M.; Lasher, S.; McKenney, K.; Law, K.; Sinha, J. *Int. J. Hydrogen Energy* **2011,** *36,* 3037–3049.

(8) Sotoodeh, F.; Smith, K. J.; *Can. J. Chem. Eng.* **2013,** *91,* 1477–1490.

(9) Dalebrook, A. F.; Gan, W.; Grasemann, M.; Moret, S.; Laurenczy, G. *Chem. Commun.* **2013,** *49,* 8735–8751.

(10) Niaz, S.; Manzoor, T.; Pandith, A. H. *Renewable Sustainable Energy Rev.* **2015,** *50,* 457–469.

(11) For select reviews, see: a) Staubitz, A.; Robertson, A. P. M.; Manners, I. *Chem. Rev.* **2010,** *110,* 4079–4124. b) Bowden, M.; Autrey, T. *Curr. Opin. Solid State Mater. Sci.* **2011,** *15,* 73–79. c) Huang, Z.; Autrey, T. *Energy Environ. Sci.* **2012,** *5,* 9257–9268. d) Johnson, H. C.; Hooper, T. N.; Weller, A. S. The Catalytic

Dehydrocoupling of Amine–Boranes and Phosphine–Boranes. In *Synthesis and Application of Organoboron Compounds*; Topics in Organoometallic Chemistry, Vol. 49; Springer International Publishing: 2015; pp 153–220.
(12) Hamilton, C. W.; Baker, R. T.; Staubitz, A.; Manners, I. *Chem. Soc. Rev.* **2009,** *38,* 279–293.
(13) Yu, X.; Tan, Y. *RSC Adv.* **2013,** *3,* 23879–23894 and references cited therein.
(14) Defined as a liquid with a viscosity <500 cP. (ANSI/HI 9.6.7, 2004.)
(15) For example, the United States has over 240,000 km of pipeline dedicated to distribution of liquid petroleum products. (CIA World Factbook. https://www.cia.gov/library/publications/the-world-factbook/geos/us.html (accessed May 21, 2016).)
(16) For examples of feasibility studies, see: a) Pradhan, A. U.; Shukla, A.; Pande, J. V.; Karmarkar, S.; Biniwale, R. B. *Int. J. Hydrogen Energy* **2011,** *36,* 680–688. b) Teichmann, D.; Arlt, W.; Wassercheid, P. *Int. J. Hydrogen Energy* **2012,** *37,* 18118–18132.
(17) To give a sense of scale for such a task, there were just 224 FCEV refueling stations operational worldwide in 2013, with the majority clustered in areas of the United States, Germany, and Japan. (Alazemi, J.; Andrews, J. *Renew. Sustain. Energy Rev.* **2015,** *48,* 483–499.) By comparison, over 114,000 commercial gas stations were operational in 2012 in the United States alone. (US Census Bureau, http://factfinder.census.gov/faces/tableservices/jsf/pages/productview.xhtml?src=bkmk (accessed May 21, 2016).)
(18) Biniwale, R. B.; Rayalu, S.; Devotta, S.; Ichikawa, M. *Int. J. Hydrogen Energy* **2008,** *33,* 360–365.
(19) For a review, see: Alhumaidan, F.; Cresswell, D.; Garforth, A. *Energy Fuels* **2011,** *25,* 4217–4234.
(20) For select examples of heterogeneous dehydrogenation systems, see: a) Ferreira-Aparicio, F.; Rodríguez-Ramos, I.; Guerrero-Ruiz, A. *Chem. Commun.* **2002,** 2082–2083. b) Yamamoto, S.; Hanaoka, T.; Hamakawa, S.; Sato, K.; Mizukami, F. *Catal. Today* **2006,** *118,* 2–6. c) Biniwale, R. B.; Ichikawa, M. *Chem. Eng. Sci.* **2007,** *62,* 7370–7377. d) Wang, B.; Froment, G. F.; Goodman, D. W. *J. Catal.* **2008,** *253,* 239–243. e) Yolcular, S.; Olgun, O. *Catal. Today* **2008,** *138,* 198–202. f) Lázaro, M. P.; García-Bordejé, E.; Sebastiàn, D.; Lázaro, M. J.; Moliner, R. *Catal. Today* **2008,** *138,* 203–209. g) Shukla, A. A.; Gosavi, P. V.; Pande, J. V.; Kumar, V. P.; Chary, K. V. R.; Biniwale, R. B. *Int. J. Hydrogen Energy* **2010,** *35,* 4020–4026. h) Antony, P. S.; Sohony, R. A.; Biniwale, R. B. *Int. J. Hydrogen Energy* **2014,** *39,* 6944–6952. i) Al-ShaikhAli, A. H.; Jedidi, A.; Cavallo, L.; Takanabe, K. *Chem. Commun.* **2015,** *51,* 12931–12934. For select examples of arene hydrogenation, see: a) Nowicki, A.; Le Boulaire, V.; Roucoux, A. *Adv. Synth. Catal.* **2007,** *349,* 2326–2330. b) Zahmakiran, M.; Tonbul, Y.; Özkar, S. *Chem. Commun.* **2010,** *46,* 4788–4790. c) Dehm, N. A.; Zhang, X.; Buriak, J. M. *Inorg. Chem.* **2010,** *49,* 2706–2714. d) Hubert, C.; Denicourt-Nowicki, A.; Beaunier, P.; Roucoux, A. *Green Chem.* **2010,** *12,* 1167–1170. e) Fang, M.; Machalaba, N.; Sánchez-Delgado, R. A. *Dalton Trans.* **2011,** *40,* 10621–10632.
(21) $\Delta H_{rxn} \approx +16$ kcal-(mol H_2)$^{-1}$ for a number of common cycloalkanes (Ref. 18).
(22) Moores, A.; Poyatos, M.; Luo, Y.; Crabtree, R. H. *New J. Chem.* **2006,** *30,* 1675–

1678.
(23) a) Clot, E.; Eisenstein, O.; Crabtree, R. H. *Chem. Commun.* **2007,** 2231–2233. b) Cui, Y.; Kwok, S.; Bucholtz, A.; Davis, B.; Whitney, R. A.; Jessop, P. G. *New J. Chem*. **2008,** *32,* 1027–1037. c) Lu, R.-F.; Boëthius, G.; Wen, S.-H.; Su, Y.; Deng, W.-Q. *Chem. Commun*. **2009,** 1751–1753. d) Dean, D.; Davis, B.; Jessop, P. G. *New J. Chem.* **2011,** *35,* 417–422. e) Mikami, Y.; Ebata, K.; Mitsudome, T.; Mizugaki, T.; Jitsukawa, K.; Kaneda, K. *Heterocycles* **2011,** *82,* 1371–1377. f) Wu, J.; Talwar, D.; Johnston, S.; Yan, M.; Xiao, J. *Angew. Chem. Int. Ed.* **2013,** *52,* 6983–6987. g) Luca, R. O.; Huang, D. L.; Takase, M. K.; Crabtree, R. H. *New J. Chem.* **2013,** *37,* 3402–3405. h) Fujita, K.; Tanaka, Y.; Kobayashi, M.; Yamaguchi, R. *J. Am. Chem. Soc.* **2014,** *136,* 4829–4832. i) Chakraborty, S.; Brennessel, W. W.; Jones, W. D. *J. Am. Chem. Soc.* **2014,** *136,* 8564–8567. j) Shen, Y.; Maamor, A.; Abu-Darieh, J.; Thompson, J. M.; Kalirai, B.; Stitt, E. H.; Rooney, D. W. *Org. Proc. Res. Dev.* **2014,** *18,* 392–401.
(24) For a summary of the extensive work conducted in this field by Air Products and Chemicals Inc., see the final report for DOE project DE-FC36-04GO14006, "Design and Development of New Carbon-based Sorbent Systems for an Effective Containment of Hydrogen" (available online at: http://www.osti.gov/scitech/servlets/purl/1039432 (accessed May 21, 2016).).
(25) Verevkin, S. P.; Emel'yanenko, V. N.; Heintz, A.; Stark, K.; Arlt, W. *Ind. Eng. Chem. Res.* **2012,** *51,* 12150–12153.
(26) Pez, G. P.; Scott, A. R.; Cooper, A. C.; Cheng, H.; Wilhelm, F. C.; Abdourazak, A. H. U.S. Patent 7,351,395 April 1, 2008.
(27) a) Sotoodeh, F.; Smith, K. J. *J. Catal.* **2011,** *279,* 36–47. b) Sotoodeh, F.; Huber, B. J. M.; Smith, K. J. *Int. J. Hydrogen Energy* **2012,** *37,* 2715–2722. c) Yang, M.; Han, C.; Ni, G.; Wu, J.; Cheng, H. *Int. J. Hydrogen Energy* **2012,** *37,* 12839–12845. d) Yang, M.; Dong, Y.; Fei, S.; Ke, H.; Cheng, H. *Int. J. Hydrogen Energy* **2014,** *39,* 18976–18983. e) Amende, M.; Gleichweit, C.; Werner, K.; Schernich, S.; Zhao, W.; Lorenz, M. P. A.; Höfert, O.; Papp, C.; Koch, M.; Wasserceid, P.; Laurin, M.; Steinrück, H.-P.; Libuda, J. *ACS Catal.* **2014,** *4,* 657–665.
(28) Eblagon, K. M.; Rentsch, D.; Friedrichs, O.; Remhof, A.; Zuettel, A.; Ramirez-Cuesta, A. J.; Tsang, S. C. *Int. J. Hydrogen Energy* **2010,** *35,* 11609–11621.
(29) Campbell, P. G.; Zakharov, L. N.; Grant, D. J.; Dixon, D. A.; Liu, S.-Y. *J. Am. Chem. Soc.* **2010,** *132,* 3289–3291.
(30) The final summary report for this preceding project (DE-FG3608GO18143, "Hydrogen Storage by Novel CBN Heterocycle Materials") is available online at www.osti.gov/servlets/purl/1221989/ (accessed April 10, 2016).
(31) Shaw, W. J.; Bowden, M.; Karkamkar, A.; Howard, C. J.; Heldebrant, D. J.; Hess, N. J.; Linehan, J. C.; Autrey, T. *Energy Environ. Sci.* **2010,** *3,* 796−804.
(32) McWhorter, S.; Read, C.; Ordaz, G.; Stetson, N. *Curr. Opin. Solid State Mater. Sci.* **2011,** *15,* 29–38.
(33) Vakaraki, E.; Lymberopoulos, N.; Zachariou, A. *J. Power Sources* **2003,** *118,* 14–22.
(34) a) Santarelli, M.; Calì, M.; Macagno, S. *Int. J. Hydrogen Energy* **2004,** *29,* 1571–1586. b) Contreras, A.; Posso, F.; Guervos, E. *Appl. Energy* **2010,** *87,* 1376–1385.

(35) a) Elgowainy, A.; Gaines, L.; Wang, M. *Int. J. Hydrogen Energy* **2009,** *34,* 3557–3570. b) Renquist, R. V.; Dickman, B.; Bradley, T. H. *Int. J. Hydrogen Energy* **2012,** *37,* 12054–12059.
(36) Whittemore, S. M.; Bowden, M.; Karkamkar, A.; Parab, K.; Neiner, D.; Autrey, T.; Ishibashi, J. S. A.; Chen, G.; Liu, S.-Y.; Dixon, D. A. *Dalton Trans.* **2016,** *45,* 6196–6203.
(37) Luo, W.; Campbell, P. G.; Zakharov, L. V.; Liu, S.-Y. *J. Am. Chem. Soc.* **2011,** *133,* 19326–19329.
(38) Luo, W.; Neiner, D.; Karkamkar, A.; Parab, K.; Garner, E. B., III; Dixon, D. A.; Matson, D.; Autrey, T.; Liu, S.-Y. *Dalton Trans.* **2013,** *43,* 611–614.
(39) *CRC Handbook of Chemistry and Physics*, 96th ed., 2015–2016, http://www.hbcpnetbase.com (accessed April 7, 2016).
(40) Effects of Liquid Viscosity on Rotodynamic (Centrifugal and Vertical) Pump Performance (ANSI/HI 9.6.7, 2004).
(41) $E_T(30) = \frac{28591}{\lambda_{max}^{abs}}$, where λ_{max} is the wavelength at the absorption maximum of the longest-wavelength intramolecular charge-transfer π–π * band of Reichardt's dye.
(42) Luo, W.; Campbell, P. G.; Zakharov, L. V.; Liu, S.-Y. *J. Am. Chem. Soc.* **2013,** *135,* 8760.
(43) Nguyen, M. T.; Nguyen,V. S.; Matus, M. H.; Gopakumar, G.; Dixon, D. A. *J. Phys. Chem. A* **2007,** *111,* 679–690.
(44) Neiner, D.; Karkamkar, A.; Bowden, M.; Choi, Y. J.; Luedtke, A.; Holladay, J.; Fisher, A.; Szymczak, N.; Autrey, T. *Energy Environ. Sci.* **2011,** *4,* 4187–4193.
(45) Liu, S.-Y.; Parab, K.; Luo, W.; Campbell, P. (University of Oregon). Boron-Nitrogen Heterocycles. WO 2012/103251 A1, August, 2, 2012.
(46) Roberts, J. D.; Mazur, R. H. *J. Am. Chem. Soc.* **1951,** *73,* 2509–2520.
(47) Chrostowska, A.; Xu, S.; Lamm, A. N.; Mazière, A.; Weber, C. D.; Dargelos, A.; Baylère, P.; Graciaa, A.; Liu, S.-Y. *J. Am. Chem. Soc.* **2012,** *134,* 10279–10285.
(48) Xu, S.; Mikulas, T. C.; Zakharov, L. N.; Dixon, D. A.; Liu, S.-Y. *Angew. Chem. Int. Ed.* **2013,** *52,* 7527–7531.
(49) An alternative synthetic route to **F** starting from *N*-methylallylamine has also been reported (Ref. 61).
(50) Chen, G.; Zakharov, L. N.; Bowden, M. E.; Karkamkar, A. J.; Whittemore, S. M.; Garner, E. B., III; Mikulas, T. C.; Dixon, D. A.; Autrey, T.; Liu, S.-Y. *J. Am. Chem. Soc.* **2015,** *137,* 134–137.
(51) Sadhu, K. M.; Matteson, D. S. *Organometallics* **1985,** *4,* 1687–1689.
(52) Martichonok, V.; Jones, J. B. *Bioorg. Med. Chem.* **1997,** *5,* 679–684.
(53) Blaquiere, N.; Diallo-Garcia, S.; Gorelsky, S. I.; Black, D. A.; Fagnou, K. *J. Am. Chem. Soc.* **2008,** *130,* 14034–14035.
(54) Park, K. S.; Ni, Z.; Côté, A. P.; Choi, J. Y.; Huang, R.; Uribe-Romo, F. J.; Chae, H. K.; O'Keefe, M.; Yaghi, O. M. *Proc. Nat. Acad. Sci.* **2006,** *103,* 10186–10191.
(55) Kandiah, M.; Nilsen, M. H.; Usseglio, S.; Jakobsen, S.; Olsbye, U.; Tilset, M.; Larabi, C.; Quadrelli, E. A.; Bonino, F.; Lillerud, K. P. *Chem. Mater.* **2010,** *22,* 6632–6640.
(56) Characterization of the properties and reactivity of **J** and its derivatives has been summarized already in part in the final report for the earlier DOE project

DE-FG3608GO18143 (Ref. 30). The section included herein details primarily the findings pertaining to **J** made in the course of the current project only.
(57) Morimoto, T.; Takahashi, T.; Sekiya, M. *J. Chem. Soc., Chem. Commun.* **1984,** 794–795.
(58) Luo, W.; Zakharov, L. N.; Liu, S.-Y. *J. Am. Chem. Soc.* **2011,** *133,* 13006–13009.
(59) Kukolich, S. G.; Sun, M.; Daly, A. M.; Luo, W.; Zakharov, L. N.; Liu, S.-Y. *Chem. Phys. Lett.* **2015,** *639,* 88–92.
(60) Daly, A. M.; Tanjaroon, C.; Marwitz, A. J. V.; Liu, S.-Y.; Kukolich, S. G. *J. Am. Chem. Soc.* **2010,** *132,* 5501−5506.
(61) Kumar, A.; Ishibashi, J. S. A.; Hooper, T. N.; Mikulas, T. C.; Dixon, D. A.; Liu, S.-Y.; Weller, A. S. *Chem. Eur. J.* **2016,** *22,* 310−322.
(62) Bassett, D. W.; Habgood, H. W. *J. Phys. Chem.* **1960,** *64,* 769–773. $\ln\left(\frac{1}{1-x}\right) = k_r \mathrm{RT}\left(\frac{W}{F}\right)$, wherein x is fractional conversion, k_r is the apparent rate constant, R is the gas law constant, T is the absolute temperature, W is the catalyst mass, and F is the carrier gas flow rate.
(63) Despite extensive synthetic efforts, we were unable to prepare an isomerically pure sample of 1,2-dimethylcyclohexene; our comparison is thus based on a 5:1 mixture of 1,2- and 1,6-dimethylcyclohexene.
(64) The dehydrogenation reaction of dimethylcyclohexene, and also unsubstituted cyclohexene, was necessarily studied at lower temperatures to avoid competing dehydrogenation of the cyclohexane side-product inevitably generated in the presence of the Pd/C catalyst.
(65) We were unable to compare the CC dehydrogenation kinetics of **X** directly to those of 1,2-dimethylcyclohexane itself, as both the *cis* and *trans* isomers of the latter rapidly deactivated the Pd/C catalyst under our standard reaction conditions.
(66) For some theoretical treatments, see: a) Hoffmann, R. *J. Chem. Phys.* **1964,** *40,* 2474−2480. b) Østby, K.-A.; Haaland, A.; Gundersen, G. *Organometallics* **2005,** *24,* 5318−5328. c) Grant, D. J.; Matus, M. H.; Anderson, K. D.; Camaioni, D. M.; Neufeldt, S. R.; Lane, C. F.; Dixon, D. A. *J. Phys. Chem. A* **2009,** *113,* 6121−6132. For an example of catalytic dehydrogenation, see: Kim, S.-K.; Han, W.-S.; Kim, T.-J.; Kim, T.-Y.; Nam, S. W.; Mitoraj, M.; Piekoś, Ł; Michalak, A.; Hwang, S.-J.; Kang, S. O. *J. Am. Chem. Soc.* **2010,** *132,* 9954−9955.
(67) Subsequent to our own reports on this subject, Manners has also published an extensive study of like compounds; see: Stubbs, N. E.; Schäfer, A.; Robertson, A. P. M.; Leitao, E. M.; Jurca, T.; Sparkes, H. A.; Woodall, C. H.; Haddow, M. F.; Manners, I. *Inorg. Chem.* **2015,** *54,* 10878−10889.
(68) For select examples using this process to prepare AB, see: a) Shore, S. G.; Parry, R. W. *J. Am. Chem. Soc.* **1958,** *80,* 8−12. b) Hu, M. G.; Van Paasschen, J. M.; Geanangel, R. A. *J. Inorg. Nucl. Chem.* **1977,** *39,* 2147−2150. c) Heldebrant, D. J.; Karkamkar, A.; Linehan, J. C.; Autrey, T. *Energy Environ. Sci.* **2008,** *1,* 156−160.
(69) Singaram, B. S.; Cole, T. E.; Brown, H. C. *Organometallics* **1984,** *3,* 774−777.
(70) Campbell, P. G.; Ishibashi, J. S. A.; Zakharov, L. V.; Liu, S.-Y. *Aust. J. Chem.* **2014,** *67,* 521−524.
(71) Dissociation of the analogous dimer of **J** to form two units of **36** was predicted to be essentially thermoneutral in terms of free energy (ΔG_{298K} = –0.3 kcal-mol^{-1}).

(72) Rahimpour, M. R.; Dehnavi, M. R.; Allahgholipour, F.; Iranshahi, D.; Jokar, S. M. *Appl. Energy* **2012,** *99,* 496–512 and references cited therein.
(73) Wechsler, D.; Cui, Y.; Dean, D.; Davis, B.; Jessop, P. G. *J. Am. Chem. Soc.* **2008,** *130,* 17195–17203.

Acknowledgment:

"This material is based upon work supported by the U.S. Department of Energy's Office of Energy Efficiency and Renewable Energy (EERE) under the Fuel Cell Technologies Office (FCTO) under Award Number DE- EE0005658."